12-2014

Development of RF accelerating structures in the front-end system of light ion particle accelerators

Ki Ryung Shin
University of Tennessee - Knoxville, kshin1@vols.utk.edu

To the Graduate Council:

I am submitting herewith a dissertation written by Ki Ryung Shin entitled "Development of RF accelerating structures in the front-end system of light ion particle accelerators." I have examined the final electronic copy of this dissertation for form and content and recommend that it be accepted in partial fulfillment of the requirements for the degree of Doctor of Philosophy, with a major in Electrical Engineering.

Aly E. Fathy, Major Professor

We have read this dissertation and recommend its acceptance:

Marianne Breinig, Seddik M. Djouadi, Syed K. Islam, Yoon W. Kang

Accepted for the Council:

Carolyn R. Hodges

Vice Provost and Dean of the Graduate School

(Original signatures are on file with official student records.)

Development of RF accelerating structures in the front-end system of light ion particle accelerators

A Dissertation Presented for the

Doctor of Philosophy

Degree

The University of Tennessee, Knoxville

Ki Ryung Shin

December 2014

ACKNOWLEDGEMENTS

First and foremost, I would like to express my deepest and sincere gratitude to my thesis advisor, Dr. Aly Fathy for providing me the inspiration that led to the completion of this dissertation. His extensive experience, superior knowledge, and expertise in RF and Microwave area have been extremely helpful in solving various technical problems throughout my research. Furthermore, his continued support and patience helped me complete my PhD journey.

I would like to extend my sincerest thanks to Dr. Yoon Kang for his great guidance and financial support throughout the entire course of this research. His profound understanding of high power accelerator system has been valuable for expanding my knowledge in the research area. I also gained in-depth knowledge of microwave engineering through a training session offered by the Spallation Neutron Source (SNS) at Oak Ridge National Laboratory (ORNL).

Special thanks are extended to Dr. Teja Kuruganti and Dr. Joshi Pooran for their support and career guidance throughout my Printed RF antenna research. They helped me broaden my technical expertise and knowledge.

I also wish to express my sincere thanks to my committee members, Dr. Syed Islam, Dr. Seddik Djouadi, and Dr. Marianne Breinig for their support and great suggestions.

Thanks also go to all my lab collaborators, supervisors and colleagues Robert Peglow, Sungwoo Lee, Sang-Ho Kim, and Mark Champion at SNS, Moses Chung and Mohamed Awida at Fermilab, Yazhou Wang, Song Lin, Yunseo Koo, Junkyu Lee, Reza Ghahremani, Essam Elkhouly, Ren Lingyun, Stephen Magoon and Mohamed Saleh at the University of Tennessee.

I owe my special thanks to my family for their unfailing support. I also thank God for enlightening my life with your presence. They have given me the strength to get through difficult times and they are the reason I live. I Love you forever.

ABSTRACT

The Spallation Neutron Source (SNS) at Oak Ridge National Laboratory (ORNL) is an RF linear accelerator-based neutron source which utilizes various RF cavity resonators to interact with a traveling particle beam to transfer energy to the beam. The RF cavity resonator generates a strong electromagnetic modal field specifically shaped at an operating frequency to provide good energy efficiency. Having a reliable cavity RF field is therefore, important to sustain performance and stable operation of the accelerator system. Although the SNS system is already built and in use, some parts still need to be improved to achieve better performance and higher operational reliability. Our study can provide potential improvements in existing accelerators as well as future ones. For example, the performance and reliability of the radio frequency quadrupole (RFQ) and the rebuncher cavities in the low beam energy front-end section of the SNS accelerators, have been improved by applying our newly proposed design ideas. In this dissertation, we propose four development directions for RFQ and rebuncher cavity to enhance its performance and field stabilization. These include: 1) a practical design method to determine RFQ fabrication tolerance based on extensive 3D simulations to help reduce RFQ fabrication errors. 2) alternative RFQ designs to improve RFQ mode separation with lower fabrication, tuning costs and structural reliability. 3) a multi-section RFQ with new RF coupling scheme which is validated with scaled prototyping. This design eliminates spurious electromagnetic modes and can decrease manufacturing and tuning costs of long coupled RFQs. 4) a double gap rebuncher cavity design instead of a single cavity for decreased gap voltage and peak electric field. This design modification can reduce X-ray radiation intensity which can address safety

problems in the current accelerator front-end area. A summary of our proposed solutions and contributions are presented in this dissertation paper.

TABLE OF CONTENTS

LIST OF TABLES

LIST OF FIGURES

CHAPTER I

INTRODUCTION

In this dissertation, we study the front end section of radio frequency (RF) particle accelerators in detail. A few design issues are addressed through simulation and measurements. Accurate 3D simulations using Commercial CAD tools have been extensively utilized, and some experimental prototypes have been developed to validate our results. The developments process presented in this dissertation is applicable to most front-end sections of light ion accelerators even though the work is often associated to the front-end in H- ion linear accelerator of the Spallation Neutron Source (SNS) at Oak Ridge National Laboratory (ORNL). In this chapter, we give a brief overview of the SNS, then summarize our research tasks and list our contributions.

1.1 Background

1.1.1 RF Engineering for Particle Accelerator

RF and microwave engineering is widely used for advanced scientific and engineering research activities. One important application of RF and microwave engineering includes charged particle accelerators which require RF technology for acceleration of various charged particles; for achieving their high energy states for diverse scientific, industrial, and medical uses. They are also used in fundamental particle physics with high energy particle colliders, material research through X-ray scattering with generation of synchrotron light and free-electron lasers (FEL), and through neutron scattering with neutron source, isotope production with ion accelerators, cancer treatment using electron, proton, or carbon particles, and future energy

development with nuclear waste treatment. For the above diverse applications and more to come, demand for high power accelerator facility is rapidly increasing, but there are still many challenges and research opportunities that need to be addressed by RF engineers.

Spallation Neutron Source at ORNL

The Spallation Neutron Source (SNS) located in Oak Ridge National Laboratory (ORNL) [1] is a proton accelerator-based pulsed neutron source. The SNS was built by a collaboration of six U.S. national laboratories – Lawrence Berkeley National Laboratory (LBNL), Los Alamos National Laboratory (LANL), Argon National Laboratory (ANL), Thomas Jefferson National Laboratory (JLAB), Brookhaven National Laboratory (BNL), and ORNL. The H- ions are generated by RF induced plasma ion source and accelerated (through RF field in evacuated RF cavity resonators) to hit a metallic target to generate neutrons. The surplus electron in the H- ion is removed when injected into an accumulator ring accelerator.

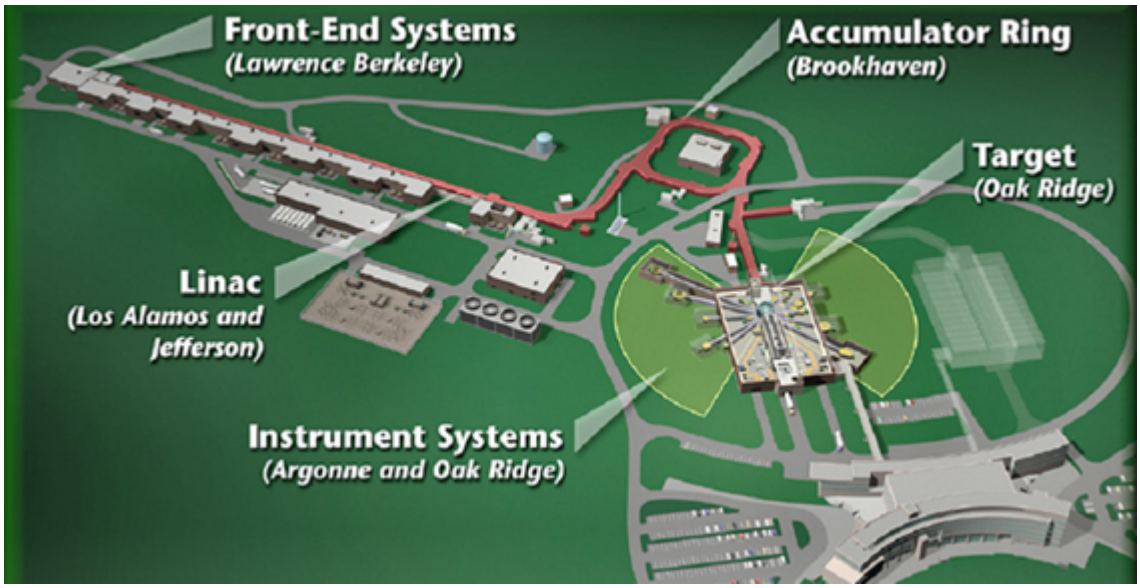

Figure 1. SNS and SNS Front End System.

RF Cavity in Particle Accelerator

The RF cavity is an effective tool to deliver RF power to increase the energy of DC particle beam as shown in Figure 2. Utilization of RF power source is preferred since it provides higher breakdown limit than DC source. An RF cavity can resonate with infinitely many electromagnetic resonant modes. Typically, one of the modes that are classified as the transverse electric (TE), transverse magnetic (TM), transverse electromagnetic (TEM), and hybrid modes is used in a resonant cavity for achieving the goal of transfer of RF energy to particles. A well-designed RF cavity has high quality factor (Q-factor) that can provide high efficiency [2] for the energy transferring task.

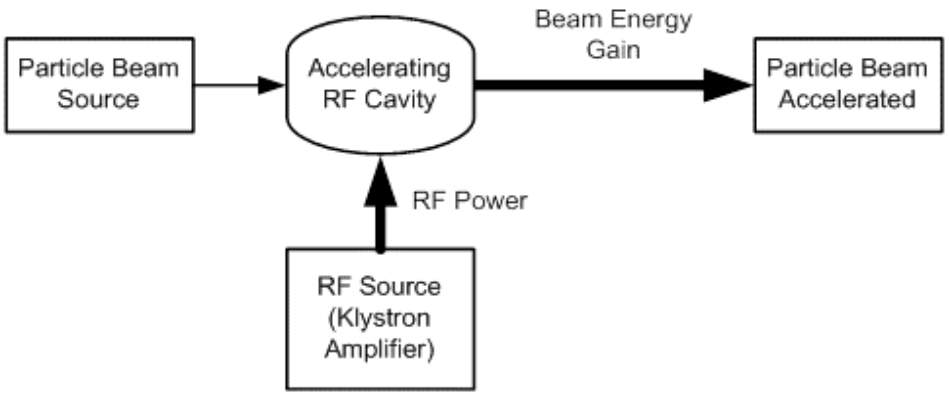

Figure 2. RF cavity to beam energy transfer process.

1.1.2 Front-end system of SNS

A) Introduction:

The work of conceptual development presented here deals with RF cavities at the lower energy section of a light ion accelerator. More specific examples and discussions are presented in this paper using the front-end (FE) section of the SNS H- ion linear accelerator shown in Figure 3 [3]. The FE contains the ion source, radio frequency quadrupole (RFQ), and medium energy beam transport (MEBT) line. The ion source generates H- ion DC beam by plasma reaction. The RFQ has two functions: First, it converts this DC beam into RF beam by adiabatic longitudinal bunching and acceleration [4]. Second, RFQ also provides a strong quadrupole focusing by electric field. The particle beam energy at SNS RFQ outlet is 2.5 MeV, with 7% speed of light [5]. The MEBT line matches the beam parameters of the RFQ output beam in order to meet the beam physics requirements of the next accelerator section. A number of focusing elements exist

in MEBT line for realizing transverse and longitudinal focusing. The longitudinal focusing is achieved by four rebuncher cavities in MEBT line [6]. Each cavity spends different power for optimized beam dynamics, and the fourth cavity is operated with the highest power as shown in Table 1.

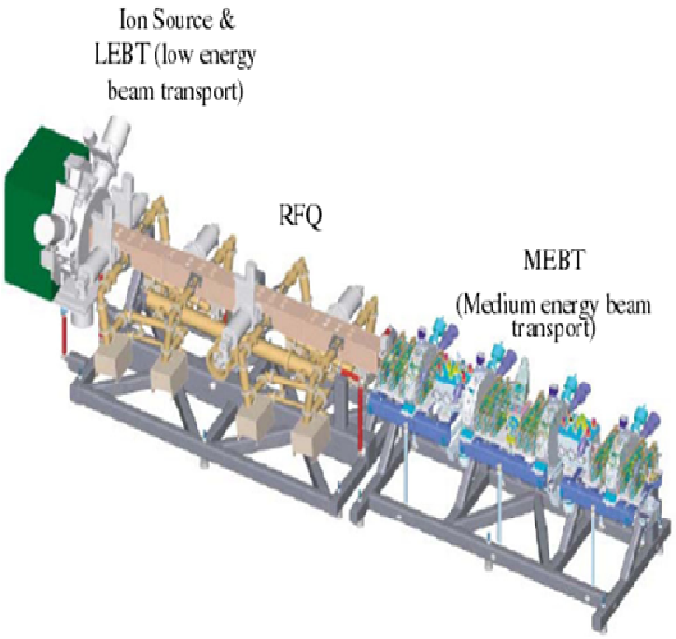

Figure 3. Overview of the SNS front-end accelerator system – After [3].

Table 1. Required gap voltage and power of MEBT cavities.

	Cavity 1	***Cavity 2***	***Cavity 3***	***Cavity 4***
Gap voltage (kV)	75	45	49.3	120
Peak power (kW)	11.0	6.8	8.1	28.2

In this dissertation we will focus on two sections: RFQ, and MEBT sections.

I. RFQ

The RFQ is evolved from the quadruple ridge waveguide, which contains four ridges in a cross section. The ridges in the waveguide are equivalent to the vanes in RFQ as it is shown in Figure 4. These four vanes are necessary to generate quadrupole mode that is known to be effective for particle focusing. The TE electromagnetic mode is used in the RFQ [4].

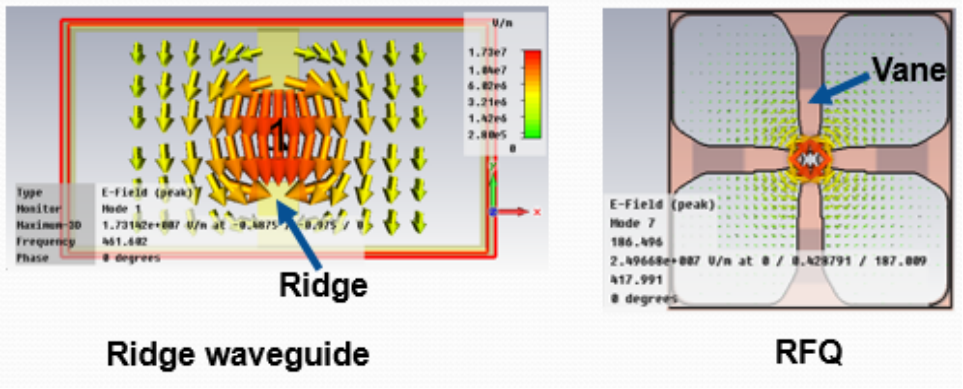

Figure 4. Ridge waveguide and RFQ

RFQ generates about 30 MV/m surface electric field between inter-vane gaps. This strong electric field generation is required to provide a good focusing gradient that is important to transport non-relativistic particle beam. As a result, very high capacitances are formed at RFQ vane gaps. Figure 5 represents how beam particle experiences RFQ focusing field in a quadrupole mode. The common notation of quadrupole mode is TE210 (or Q_0), and will be consistently used in the following discussions.

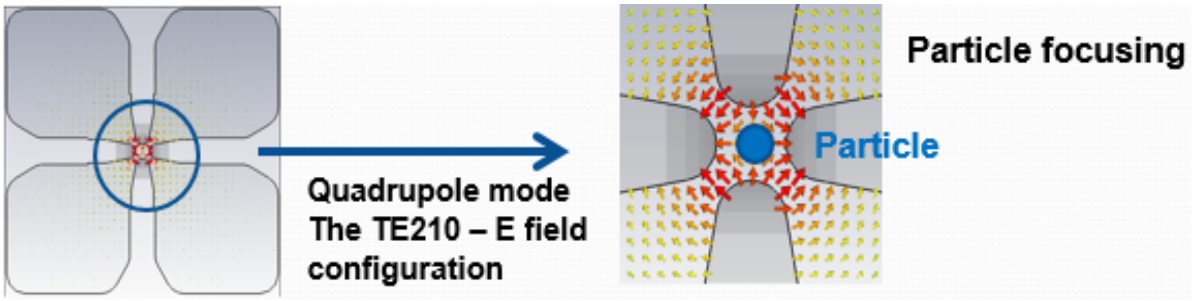

Figure 5. Quadrupole mode and particle focusing.

Inherently, the RFQ TE210 mode does not have an electric field component in the longitudinal (axial) direction where particles move along. However, some axial electric fields are generated by dimensional modifications; known as vane tip modulations [4] as shown in Figure 6. Particle bunching and acceleration are realized with this axial field synchronized to the accelerating particle velocity. As a result, the real RFQ operating mode is not a pure TE210 mode but a complex TE210-like mode through this vane tip modulation. However, this axial field strength is much smaller than the focusing field. Therefore, for modeling simplicity, a uniform transverse geometry with no vane tips modulations will be used in our electromagnetic (EM) simulation of RFQs in the following discussion.

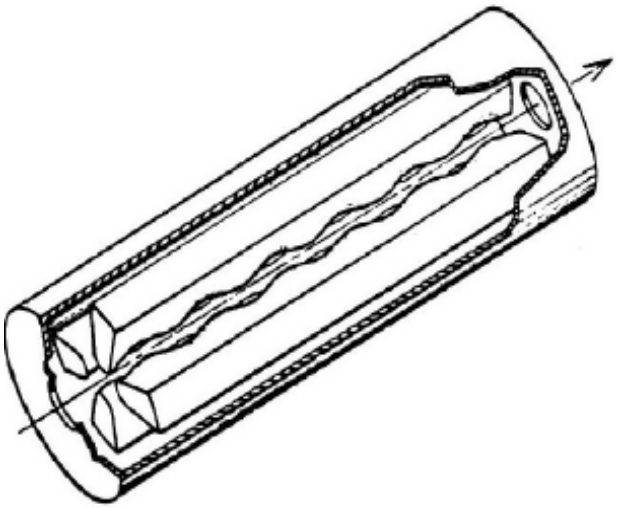

Figure 6. RFQ vane modulation for bunching and acceleration - After [7].

II. MEBT

The MEBT provides beam focusing in transverse and longitudinal directions. Installed quadrupole magnets focus a beam in the transverse plane. The longitudinal focusing is achieved with four rebuncher cavities as shown in Figure 7.

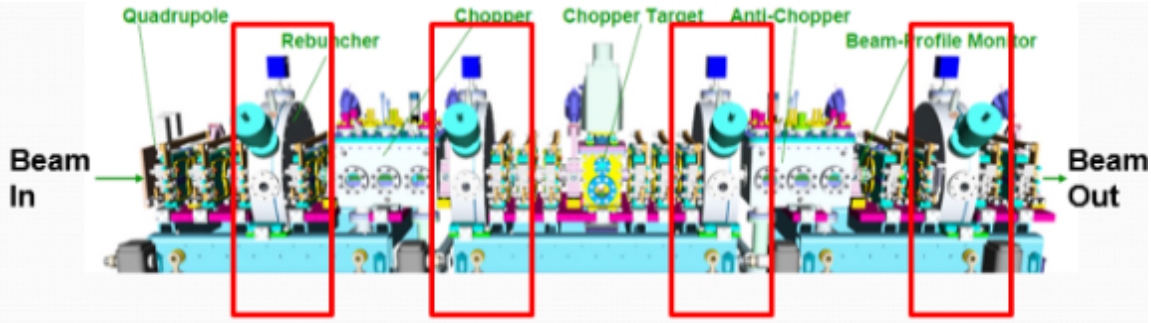

Figure 7. MEBT line and rebuncher cavities – After [8].

Rebuncher cavities in the MEBT operate with -90º RF phase from the electric field maximum to focus the ion beam on the axial direction using velocity modulation [8]. The principle of bunching by velocity modulation is described in Figure 8. The RF signal phase at the MEBT cavity gap is -90º when a reference particle has the exact designed particle speed. Electric field at this phase is zero crossing, hence the reference particle does not gain any energy. When a slow particle passes this cavity gap, however, the RF signal phase becomes positive and gains energy. As a result, the speed of slow particle increases and catches the reference particle. In the same way, a fast particle is retarded at this cavity gap because of the minus RF signal phase. Therefore, the overall longitudinal particle focusing, i.e. bunching, is realized by MEBT cavity gaps.

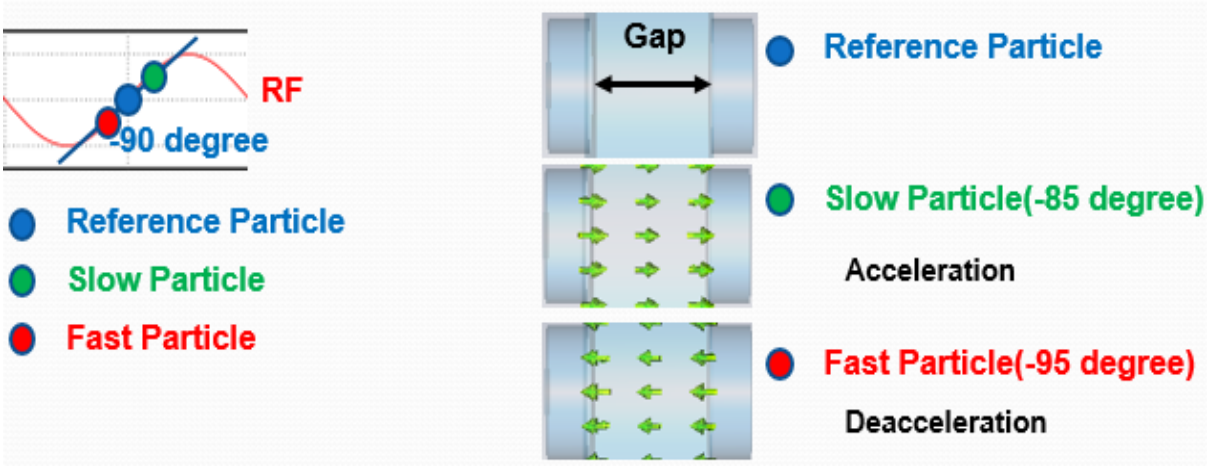

Figure 8. Bunching example.

B) Specific Objectives

In this dissertation, I am presenting the results of our investigation for more reliable and simple designs of RFQ and MEBT buncher cavities that can improve accelerator system performance, cost effectiveness, and system safety. More specifically, the objectives of our research activity include:

1) Investigate and validate full scale 3D RFQ modeling to decrease RFQ cavity design and prototyping costs
2) Develop a tolerance evaluation method with 3D perturbation study
3) Investigate and study alternative RFQ designs that increase the separation of harmful electromagnetic modes from the operating mode while decreasing the manufacturing costs
4) Develop a new multi-section coupled RFQ design that reduces design and fabrication costs of very long RFQ
5) Design validation of multi-section coupled RFQ with demonstration cavity models
6) Propose and evaluate another efficient MEBT buncher cavity design that can reduce harmful X-ray radiation
7) Perform RF and microwave measurements for model validation

C) Outline of the Dissertation

The main parts of my dissertation are Chapters 2-4. Chapter 2 and 3 address the RFQ analysis and design. Chapter 4 discusses an alternative design of MEBT buncher cavity. All chapters are aimed at improving the RF accelerator front-end section.

Chapter 2 investigates 3D modeling technology for RFQ cavity design. Conventional RFQ design was based on 2D modeling and small sized partial 3D simulation methods. The advancement in computer and simulation technology has led to large scale 3D modeling that is essential to analyze RFQ in detail. Our efforts to develop RFQ modeling, mesh setup, and accuracy verification with measurements are discussed in the first part of Chapter 2. In the latter part of the chapter, a perturbation study that is carried out with this 3D method is described. The perturbation study was determined to be an effective method to analyze the RFQ fabrication tolerance.

Chapter 3 extends the 3D modeling technology to investigate alternative RFQ designs that is more cost effective and reliable. The first part of Chapter 3 discusses designs that can address the narrow mode separation problem of the RFQ cavity. Various simulations and analytic approaches are utilized to evaluate and validate these alternative designs. The second part of Chapter 3 deals with another coupled RFQ design, which is typically used in very high energy applications. The proposed design solves the previous issues of complicated design and generation of unwanted electromagnetic mode. A demonstration model is built to ensure that the results of simulation and concepts are applicable to the real world.

Chapter 4 investigates a new MEBT rebuncher cavity design to solve the present issues of SNS MEBT line. The proposed new design generates less cavity gap voltage and X-radiation, therefore can improve safety in high power operation. A scaled microwave cavity model was built and tested to validate the results of simulation and analysis. Estimation of X-radiation and thermal property was carried out as well.

Chapter 5 summarizes this dissertation work and reviews our contributions and recommendations for future research.

D) My Contributions:

We have addressed the problems by accomplishing the following tasks:

1) Developed a full-scale 3D RFQ modeling for accurate computer simulations of various developments and validated with experimental work
2) Developed a tolerance assessment method using a perturbation method
3) Proposed a simple and cost effective RFQ design process
4) Investigated the feasibility of alternative RFQ cut-back methods
5) Proposed design guidelines of the alternative RFQ cut-back methods as function of RFQ lengths and recommended various applications
6) Developed a cost effective RFQ design and fabrication method that eliminate the usage of expensive extra circuit elements for mode separation
7) Developed a new method of RFQ coupling which is simple and cost effective
8) Proved the new concept of RFQ coupling using a demonstration model

9) Suppressed the unwanted electromagnetic mode near operating quadrupole mode by adopting the new RFQ coupling method
10) Proposed a new double gap MEBT rebuncher cavity design that decreases X-ray radiation
11) Developed a design guideline for the double gap cavity with various simulation methods
12) Validated the proposed double gap cavity design with demonstration model design, fabrication, and experimental verification
13) Estimated X-ray radiation of the double gap cavity
14) Developed thermal design of the double gap cavity

I believe my significant contributions are as follows:

1) Developed a tolerance assessment method using a perturbation method
2) Developed a cost effective RFQ design and fabrication method that eliminate the usage of expensive extra circuit elements
3) Proposed design guidelines for the alternative RFQ cut-back methods as function of RFQ lengths and recommended various applications
4) Developed a new method of coupled RFQ coupling which is simple and cost effective
5) Proposed a new double gap MEBT rebuncher cavity design that decreases X-ray radiation

CHAPTER II

RADIO FREQUENCY QUADRUPOLE (RFQ) AND 3D ELECTROMAGNETIC MODELING

2.1 RFQ Background and Operational Problems

2.1.1 RFQ Background:

Since 1970s, development and operation of RFQ have been very successful and proven to be effective. They have replaced many electrostatic accelerators that were used in the low energy sections of ion accelerators [7]. Both the compact size and efficient RF focusing features make RFQ one of the most important accelerator cavity structures in modern linear accelerator technology.

An example of real RFQ and its vane part is shown in Figure 9. They usually have four vanes that have large gap capacitance and long cavity length while operating in a standing wave. Special care should be taken when designing, fabricating, and operating RFQs for the quadrupole mode. The mode is formed near waveguide cut-off and the structure is effectively housing hundreds of small half wavelength resonant cavities realized with sinusoidal vane tip modulations.

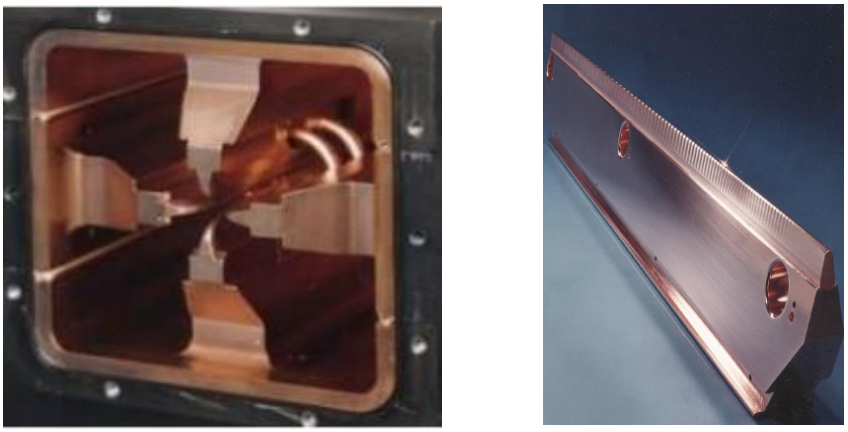

Figure 9. A real RFQ and vane part – After [9].

The RFQ as an RF circuit operates in a TE210 mode, which is a transverse electric (TE) mode with no Ez component. The modulations on the vane tip generate an Ez accelerating field component in addition to the quadrupole-like focusing fields. The modulation periods changes along the structure to match the varying speed of the accelerated charged particles. The depth of the modulations determines the strength of the longitudinal accelerating field.

The RFQ is an accelerator which is a beam transport device with acceleration added as a perturbation

As shown in Figure 10, the TE110 dipole mode is the first observable TE mode in RFQ Cavity without vanes. Here, the TE210 quadrupole mode has much higher frequency than TE110 mode. The vanes inside the RFQ cavity body concentrate the electric fields at the center. By imposing four vanes, the TE210 mode frequency becomes lower because of additional inter-vane capacitance. The TE210 quadrupole is the desirable RFQ operating mode, since it can focus any

particle that is passing through the on-axis. The TE110 dipole mode causes beam deflection, hence should be avoided by having its resonance frequency far away from the quadrupole mode.

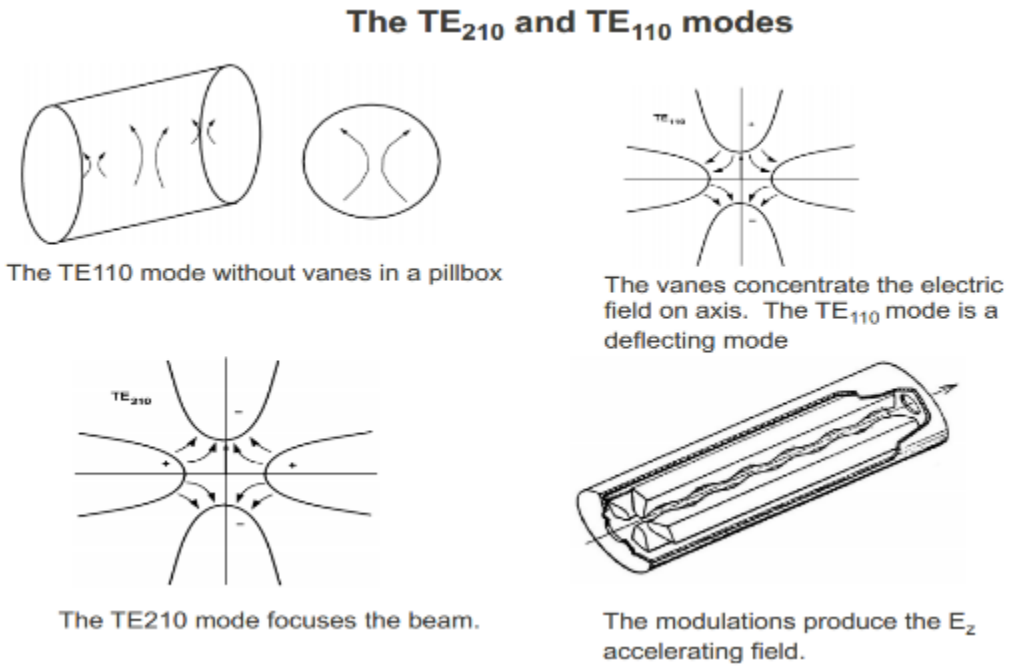

Figure 10. RFQ electromagnetic mode – After [9].

Figure 11 shows how vane modulation can generate an accelerating Ez field and a transversal focusing Eq field. The Lc in Figure 11 represents the distance that a beam particle travels in a half RF period and a period in the vane geometry. The Ez field switches from positive to negative per each half RF cycle with the vane modulation geometry. Therefore charged particles whose velocity is matched to $Lc*f_{RF}/2$ can be accelerated by the Ez field. The transversal field components Eq are all in the same direction between two neighboring vanes

(TE210 mode in figure 13) and they change their polarity every half RF cycle to result in a quadrupole like field-particle interaction for the particles moving at the right speed.

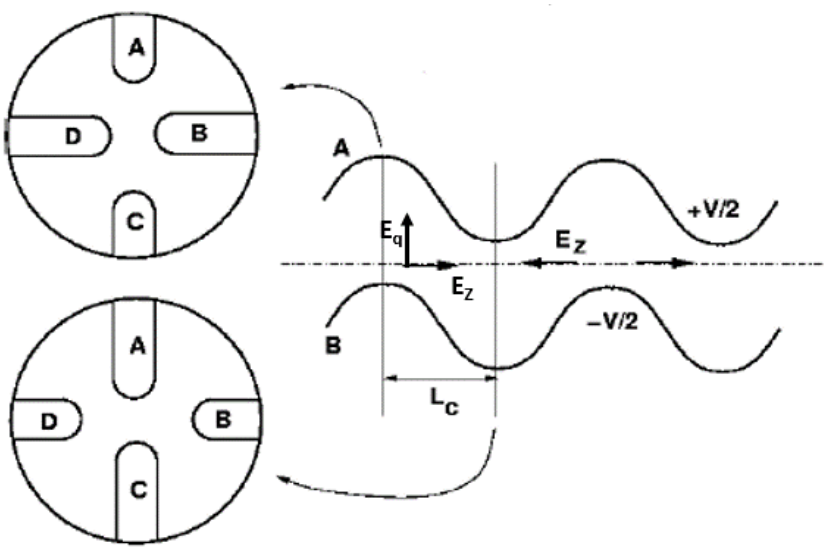

Figure 11. RFQ vane-modulation – After [9].

The RFQ tangential electric fields goes to zero due to the perfect electric (PEC) boundary condition at RFQ end walls. This condition should be avoided to maintain longitudinally uniform electric focusing field along the whole RFQ length as much as possible to prevent beam particle loss. Previous researchers solved this problem by applying cut-backs at RFQ longitudinal vane ends as shown in Figure 12. The cut-back provides open magnetic field path (i.e. no metal obstruction) while not imposing a PEC boundary condition. A cut-back capacitance is formed between vane end tip to end-wall. Figure 13 shows a comparison between the RFQ electromagnetic field with and without a cut-back design.

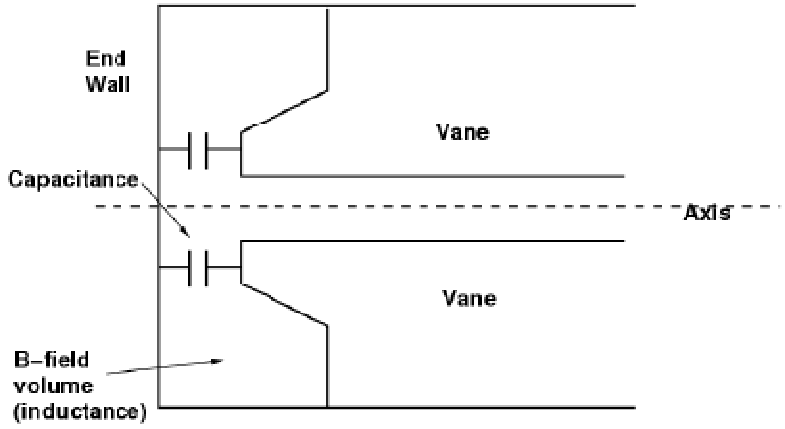

Figure 12. RFQ cut-back – After [9].

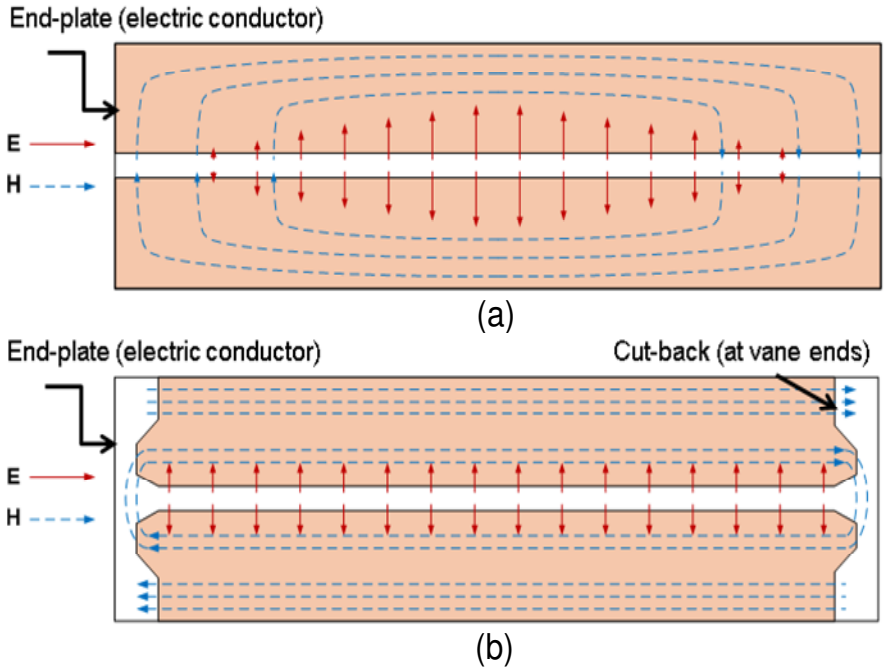

Figure 13. RFQ field by cut-back: (a) without cut-back, (b) with cut-back.

2.1.2 RFQ Operational Problems:

RFQ can experience various problems such as asymmetric axial field caused by any mechanical imperfection, narrow mode separation with adjacent unwanted modes, and high dimensional sensitivity due to very low energy flow in the structure because of their operation in a standing wave mode.

a) Mode Problem:

To be specific, RFQ cavity modes are relatively close in the frequency domain and this can cause unacceptable mode stability problems in case of any structural deformation. In particular, there are two modes: the quadrupole and dipole modes. Their frequency separation decreases as the structure length increases in a long four-vane RFQ.

b) Manufacturing errors:

RFQ provided with quadrupole can have excellent focusing if the size of the four RFQ vane gaps has good a mechanical symmetry. However in reality, achieving a perfect mechanical symmetry is difficult. For example, RFQ typically contains mechanical errors in its initial fabrication. Additional deformation could occur in RFQ operation by thermal expansion, vacuum changes, and sectional misalignment. These mechanical errors lead to RFQ field distortion, and should be tuned out before the real operation in order to have the desired field pattern.

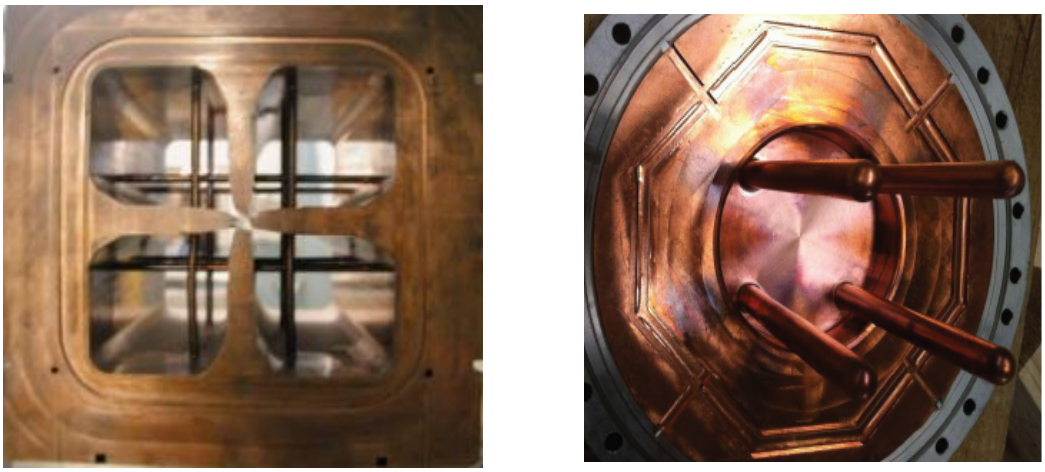

(a) (b)

Figure 14. Mode stabilization methods: (a) PISL, (b) DSR, After [9][10].

c) Stabilizer / Coupling:

This unfortunately requires extra mode stabilizer design to improve quadrupole to dipole frequency mode separation, which adds complexity to the system as shown in Figure 14. Two commonly used stabilizing methods are the Pi-mode stabilizing loop (PISL) [11] and dipole stabilizer rods (DSR) [12]. The Pi-mode stands for an azimuthal electromagnetic mode with Pi phase advance, which is the quadrupole mode. The PISL in Figure 14 (a) induces a current flow through adjacent RFQ quadrants by placing multiple stabilizing loops. The current flow increases in the dipole modes because the RF phase at each stabilizer loop ends has 180º difference compared to 0º difference in the quadrupole modes. As a result, the dipole modes experience almost short circuit and the resonant frequency of the dipole modes can be significantly higher. More than 30 MHz mode separation could be achieved in a SNS RFQ with the PISL method.

On the other hand, the DSR in Figure 14 (b) does not make current coupling between RFQ quadrants, but simply provides more perturbation on dipole fields at end-plate than on the quadrupole mode. One of the two degenerate dipole modes occupies only two opposing quadrants and has greater magnetic flux density around a rod compared to the quadrupole mode that occupies all four quadrants. Therefore, dipole mode frequencies are moved further out resulting in greater mode separation.

d) Low Energy Flow:

Additional problem is that the electromagnetic energy flow in RFQ is very small because it operates in a standing wave mode. The wave group velocity in standing wave is almost zero hence very little energy flow can occur. This makes the RFQ structure very sensitive to any perturbations. Previous researchers proposed a coupling RFQ design method to improve the wave group velocity. Researchers at Los Alamos National Laboratory (LANL) made a significant contribution by discovering a method to increase RFQ group velocity [13][14][15].

The theory of wave confluence [2] forms a basic understanding of this coupled cavity design concept with dispersion properties of periodic structures. When two cavity modes in two separate passbands - one with forward wave and the other with backward wave- have similar resonant frequencies, ω_a and ω_c as shown in Figure 15 (a), these two modes can be connected as seen in Figure 15 (b). This phenomenon is called confluence. The abscissa and ordinate of Figure 15 represent the frequency and phase advance of a cavity. The slope of Figure 15 stands for the group velocity. An interesting observation from Figure 15 is that the group velocity has non-zero

value in Figure 15 (b) after confluence occurs. Therefore, if an RFQ is designed in sections with coupling cells in between these sections, it can have a finite group velocity if operated in the standing wave mode to have both forward and backward wave modes at the same operating frequency.

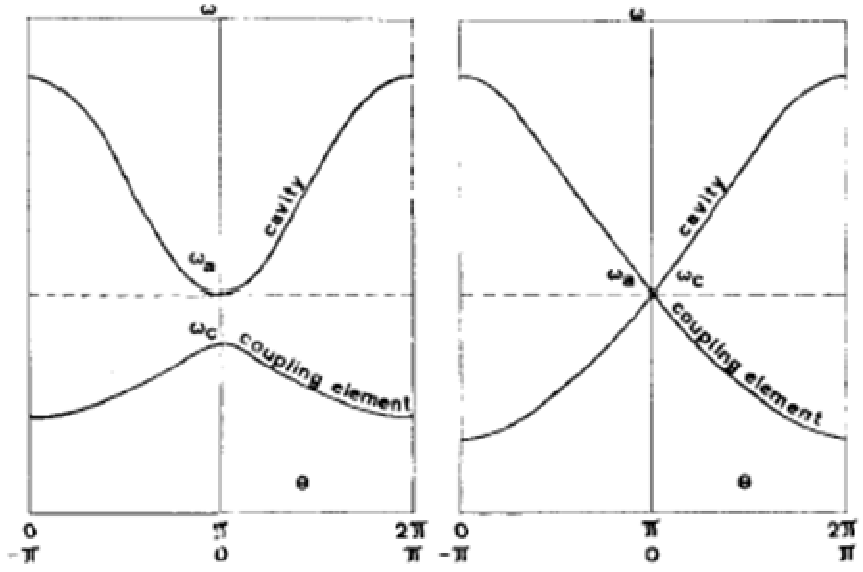

(a) (b)

Figure 15. Confluence principle: (a) before, (b) with confluence - After [2].

This confluence could be realized by using coupled RFQ design. The coupling gap created between two RFQ sections generates a TM-like forward wave mode. This gap mode couples the RFQ mode at cut-back which is a backward wave due to strong magnetic coupling. Figure 16 shows the detailed design of a RFQ coupling cell. To increase coupling strength, the coupling plate needs to be elongated to almost touch the vane overhang as shown in Figure 16 (b).

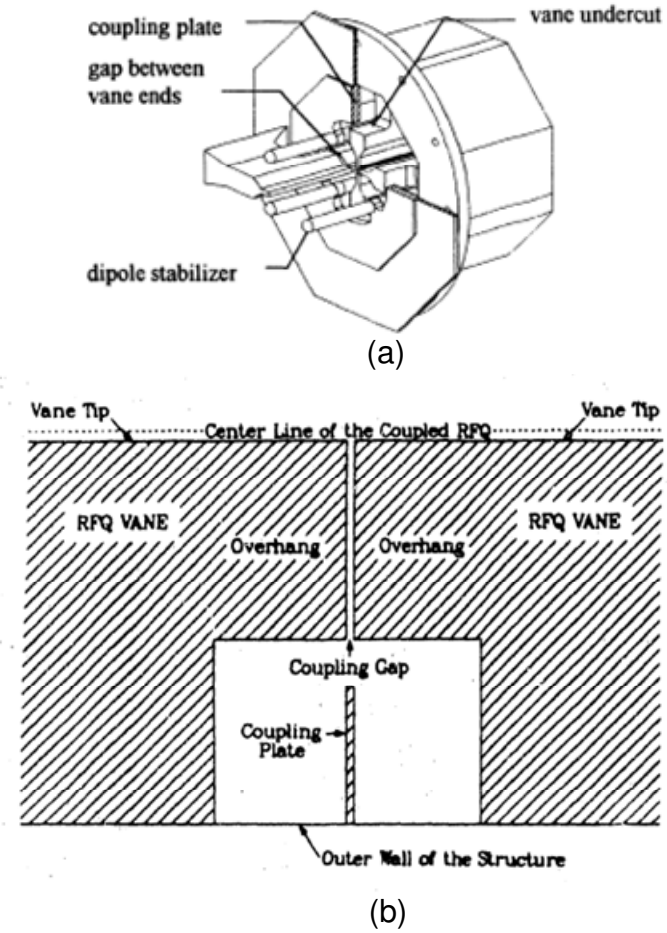

Figure 16. Coupling cell design: (a) perspective view, (b) cut-view - After [13][14].

An example of the fabricated coupled RFQ in real world is shown in Figure 17. This RFQ known as the Low Energy Demonstration Accelerator (LEDA) is an 8 meter long structure with four coupling cells. The operation of this RFQ has been successful and proved the idea of using RFQ coupling cells.

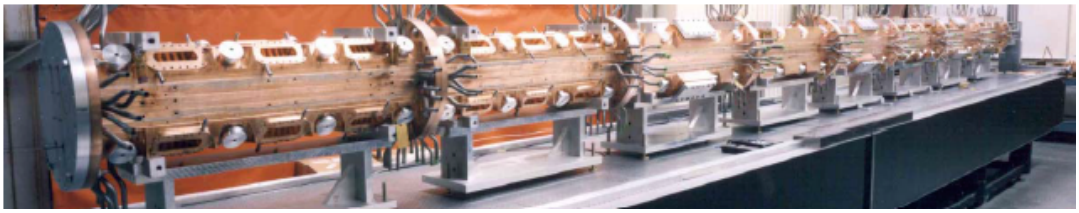

Figure 17. The LEDA coupled RFQ - After [16].

In the following sections, we utilized the 3D RFQ simulation method to solve the real RFQ design issues. We addressed the moding problem as well as, the tolerance requirement issue. Two main design issues include narrow mode separation and small group velocity and both are covered in the next chapter. In this section, we will present the alternative simulation tools required for 3D RFQ simulation, discuss its simulation and related accuracy, and use perturbation to develop a tolerance guideline for the design of these RFQs.

2.2 RFQ Modeling

2.2.1 3D simulation tools:

3D electromagnetic modeling has been the RFQ design mainstream

By the end of the 20th century, computation capacity to solve complex cavity resonators with curved boundaries was confined to mostly 2D problems due to processors and memory limitations. A well-known 2D electromagnetic (EM) simulation is Superfish [17] that utilizes the Finite Element Method (FEM). This method gives very accurate results especially for curved

geometry which is the case of accelerating RF cavities. Superfish has been utilized in many RFQ designs worldwide [9].

However, the rapid development of computer technology has led to increased use of 3D EM simulation, not only to solve a simple object but to analyze a very complex geometry like RFQ. It was a milestone work that was accomplished when researchers in Los Alamos Group [13] validated the accuracy of the 3D finite difference time-domain (FDTD) EM simulation code MAFIA [18] for various RFQ structures.

Following this achievement, another important code validation work was conducted [19] with CST Microwave Studio [20] as shown in Figure 18 – an enhanced version of MAFIA – and was compared to measurements. Although this work utilizes only one of four RFQ sections for simulations and measurements, it contains a complex PISL circuit inside the RFQ body. A prototype based on this 3D modeling provided a high level of accuracy, and motivated many researchers to utilize 3D EM simulation for future RFQ designs.

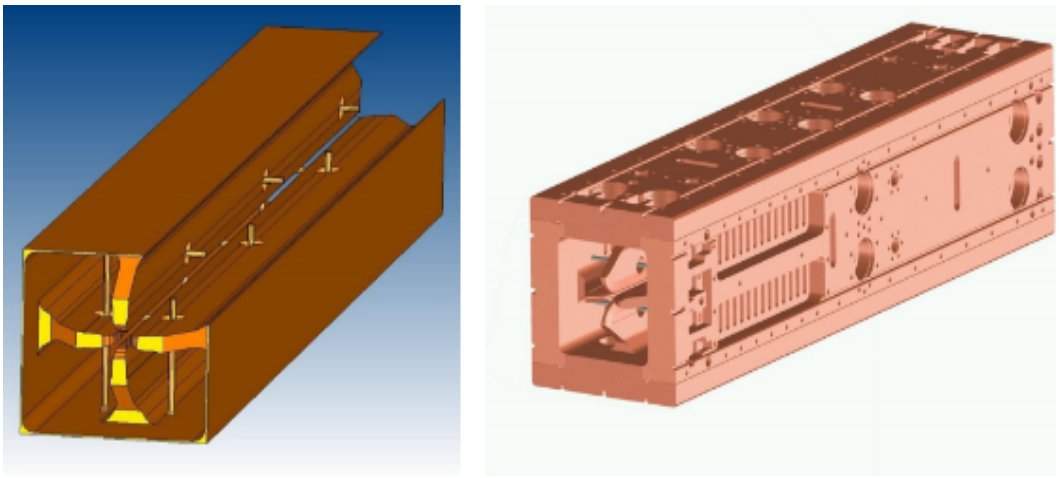

Figure 18. A CST RFQ model and prototype – After [9][19].

Other 3D EM simulation tools likewise ANSYS HFSS [21], and COMSOL Multiphysics [22] have been used to design RFQs as well as CST, and produced similar results that are in excellent agreement with the experimental data [23][24].

2.2.2 Simulation vs. Measurement:

3D RFQ modeling accuracy is validated with real RFQ measurements

The RFQ simulation is very sensitive to mesh setup because of high capacitance formed at RFQ inter-vane. Therefore, a well-defined local mesh setup is required to proceed with any RFQ simulation study with good accuracy. Here, we utilized the CST Microwave Studio [20] in all simulation work discussed in this dissertation.

Figure 19 represents the mesh setup that is utilized in this study. The automatic mesh setup has not been satisfactory for this vane perturbation analysis. Hence, a manual mesh setup with local fixpoints was used instead. 50 by 50 fixpoints were selected to divide the vane tip area with 4 μm resolution. To further improve the simulation accuracy, a manual mesh setup was also utilized at the end-region cut-back area.

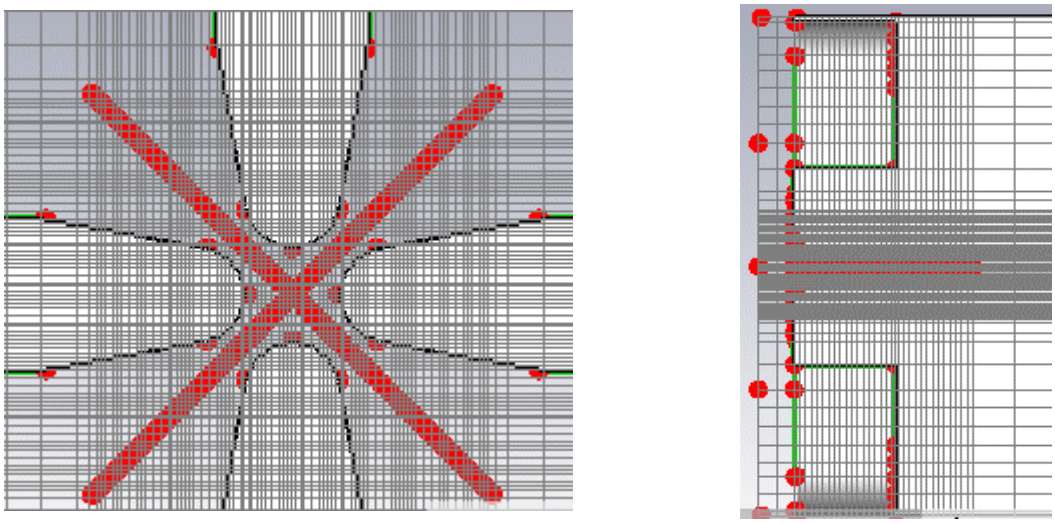

Figure 19. Mesh setup around RFQ vanes and end-region area

To validate the 3D simulated accuracy, an example simulation and measurement study of the SNS RFQ was carried out. First, a quarter section of the SNS RFQ that is 1.25 λ long was analyzed and measured. This study showed that the discrepancies between the simulated and measured frequencies were 0.20% for the fundamental quadrupole mode (Q_0), and 1.08% for the fundamental dipole mode (D_0). Our results are in very close agreement with Reference [19] as indicated in Table 2. In this example, the discrepancy in the Q_0 frequency is much less than that

of the D_0 frequency; since this SNS structure contains PISL (shown in Figure 20) that perturbs the dipole fields- and it is difficult to model it accurately.

Table 2. Simulations vs. measurement Comparison (1.25 λ, SNS RFQ).

	Measurement [19]	***Simulation PISL[19]***	***Simulation PISL [This work]***	***Simulation No PISL***
Frequency (Q_0)	402.5 MHz	403.5 MHz	403.3 MHz	413.9 MHz
Frequency (D_0)	432.9 MHz	437.6 MHz	437.6 MHz	401.6 MHz

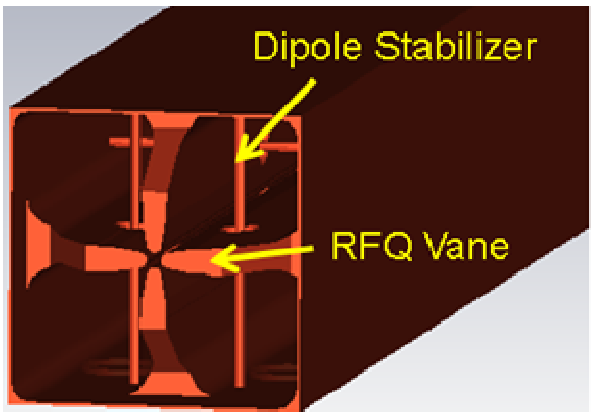

Figure 20. SNS RFQ model with PISL, shown after removing the end wall.

Second, we extended our simulation to a real size long SNS RFQ that has four sections. Figure 21 shows the measured results of this RFQ, where the Q_0 frequency is at 402.57 MHz, while the D_0 frequency is at 434.91 MHz. Our measurements were made using liquid cooling

system for stability and accuracy. A detailed comparison of the mode frequencies of our simulated (f_S) and measured (f_M) results are given in Table 3. They were all in good agreement with each other and are within 1% difference. As expected, better accuracy was noted for the Q-modes. The same mesh and simulation setup were utilized for all simulation work performed in this dissertation.

After achieving this high level of accuracy that has been validated experimentally, we gained more confidence in our simulation setup for future studies.

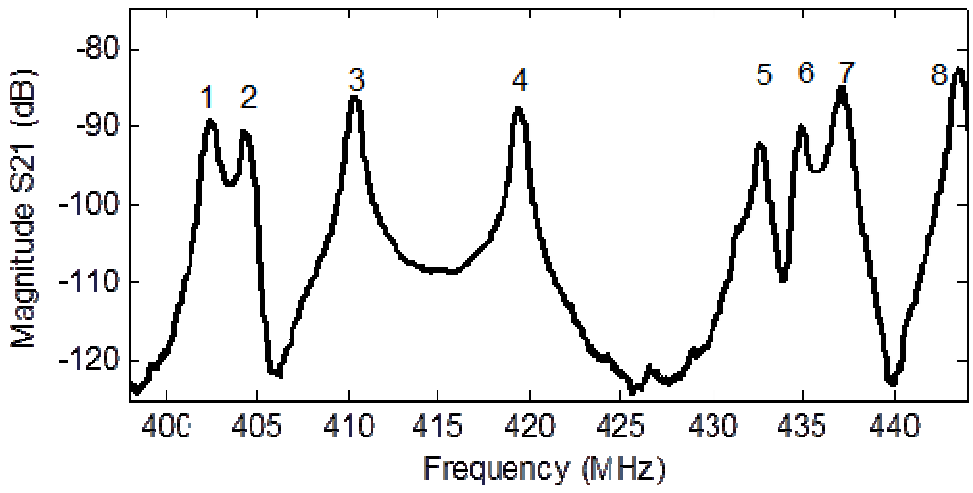

Figure 21. Measurement results of the 5.0 λ SNS RFQ.

Table 3. Simulations vs. measurement (5.0 λ, SNS RFQ model).

Mode	f_s *[MHz]*	f_M *[MHz]*	f_M *[Error %]*
1 (TE210)	401.96	402.57	0.15
2 (TE211)	403.81	404.42	0.15
3 (TE212)	409.29	410.42	0.27
4 (TE213)	418.26	419.46	0.28
5 (TE214)	430.52	432.68	0.50
6 (TE110)	437.65	434.91	-0.63
7 (TE110)	438.75	437.17	-0.36
8 (TE111)	441.00	443.61	0.59

2.3 Perturbation Study

3D simulation example – perturbation study

To address manufacturing errors, a tuning procedure is required. In this tuning process, bead-pull measurements [25][26] are usually performed at the four RFQ quadrants near vane gaps as indicated in point A in Figure 22. However, because of the narrow gap between the vanes (point B in Figure 22), it is hard to pull a bead on the beam-axis. Slug tuners are usually used to fine tune the bead-pull measured field at point A to obtain fields similar to the designed

field, and this tuned field is used as a reference field to infer the (non-measurable) on-axis field at point B. Additionally, magnetic pickup probes are used to measure the magnetic fields near the cavity wall (point C or C' of the quadrant in Figure 22). The magnetic pickup probe measurement data usually can serve as the reference field that can be maintained after complete tuning.

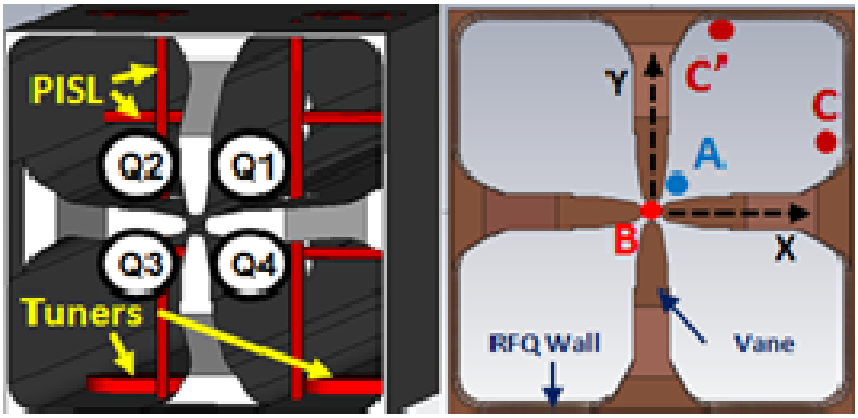

Figure 22. Slug tuners and references of RFQ field measurement.

This tuning process is effective only for RFQs which have global perturbation [27]. However, the RFQ structure could have too localized perturbation around the vane due to mechanical imperfections such as fabrication errors or structural deformations. Since the beam-axis field is predicted from the reference field measurements/estimation, it is questionable if the reference field still can represent the on-axis field when an RFQ has localized vane perturbation.

Since measuring on-axis field is very difficult, this problem can only be analyzed with simulations. A 3D simulation is desirable for applying vane perturbation on any longitudinal

location of RFQ. Figure 23 shows an example of our perturbation study that shows vane perturbation into RFQ center with 65 μm perturbation size [27] using the 3D simulation. In case 1, we assumed that the vane tip of RFQ section 3 is moved inward to the RFQ on-axis center in order to study such effect.

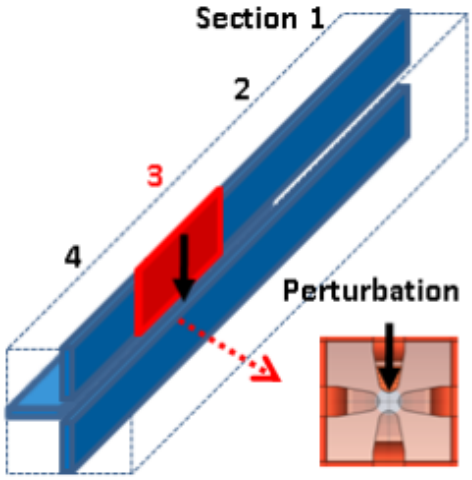

Figure 23. RFQ perturbation example - mechanical imperfection.

Electric field values at two different observation points (A and B of Figure 22) are shown in Figure 24. The top and bottom figures represent electric field intensities at vane-to-vane gap (A) and on-axis (B), respectively. The reference field before perturbation is shown as the black line. Fields are perturbed as shown by the red line, and they can be retuned as indicated by the blue line.

The on-axis field at the bottom figure represents more field distortion at the perturbation site. This extra field distortion still remains even if the RFQ field is corrected as indicated by the blue

line in Figure 24. This retuning is aimed at making the cavity wall field as flat as possible, however, the extra field distortion still can be observed on the RFQ beam axis.

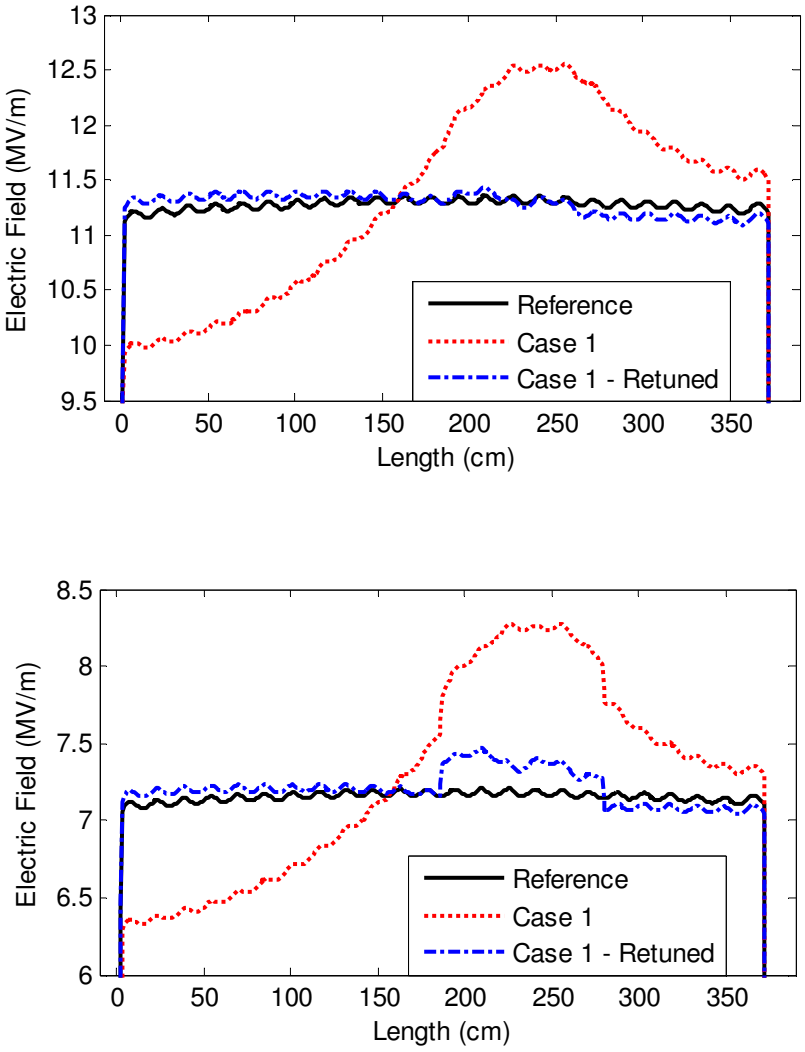

Figure 24. Disturbed and retuned RFQ field: (top) on bead-pull axis, (bottom) on beam axis.

The distorted on-axis field by perturbation can affect the RFQ beam quality and it can be shown by an analytic method. The RFQ electric field can be represented by [7]

$$
\begin{aligned}
E_X &= -\frac{XV_0}{a^2}x - \frac{kAV_0}{2} I_1(kr)\frac{x}{r}\cos(kz) \\
E_y &= \frac{XV_0}{a^2}y - \frac{kAV_0}{2} I_1(kr)\frac{y}{r}\cos(kz) \\
E_Z &= \frac{kAV_0}{2} I_0(kr)\sin(kz)
\end{aligned}
\qquad (1)
$$

where X represents the focusing efficiency, A represents the acceleration efficiency, and V_0 is the vane voltage. The second term of E_x and E_y vanishes with E_z term if vane modulation is not applied for in our simulation. This equation shows that the focusing field, which is an inverse quadratic function of the vane aperture $1/a^2$ is very sensitive to vane perturbation that changes a. The V_0/a^2 term is known as the quadrupole gradient A_0, which is a measure of its focusing strength and directly related to beam dynamics. A_0 can be calculated from the electric fields distribution in RFQ gaps such as:

$$
A_0 = -\frac{\partial E_x}{2\partial x} = \frac{\partial E_y}{2\partial y} = \frac{V_0}{2a^2} \qquad (2)
$$

If a large mechanical perturbation is present, A_0 becomes a function of the modified vane gap size as well as a vane voltage. A_0 can be calculated from the differentiation of the on-axis

field distortion. Figure 25 shows how the modified gap distorts RFQ on-axis field. In Equation (2), A_0 is calculated by differentiating this distorted field with the perturbation direction.

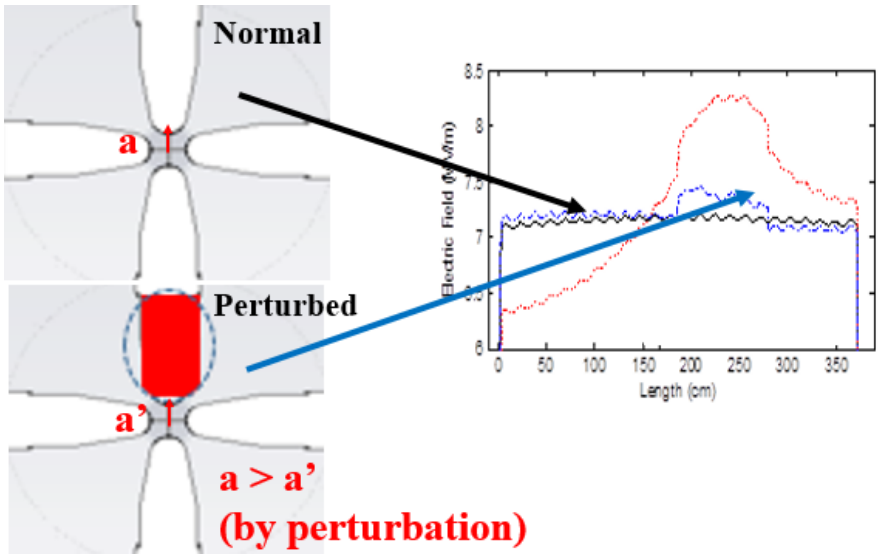

Figure 25. Vane gap variation by perturbation and distorted on-axis field.

Based on the field results of Figure 24 and Equation (2), A_0 in the transverse plane at the perturbation area is calculated in Figure 26 (a) with MATLAB [28]. Y coordinate definition follows the definition indicated in Figure 22. All A_0 values are scaled by the A_0 value of the non-perturbed reference RFQ. The retuned RFQ has slightly higher focusing gradient in the positive Y direction due to the on-axis dipolar field. However, the overall quadrupole gradient is not seriously affected by small perturbations if the RFQ is well retuned [27].

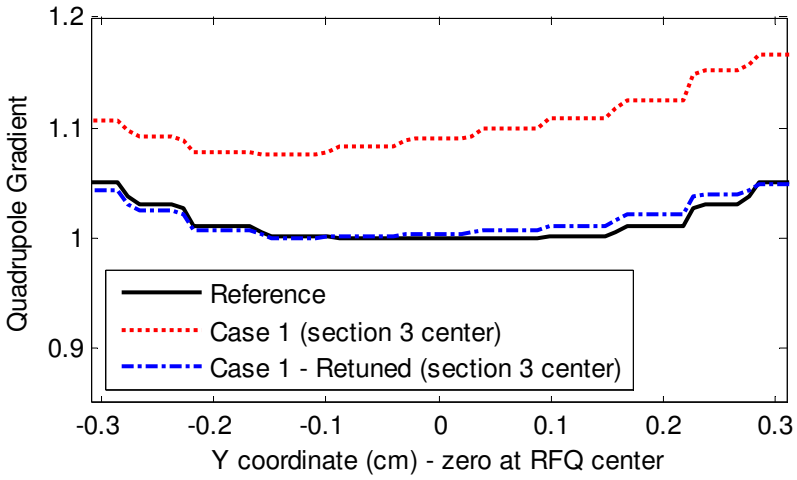

Figure 26. Quadrupole gradient with vane perturbation and retuning – scaled by reference gradient.

As perturbation size increases, A_0 mismatches after retuning increase as shown in Figure 27. If the perturbation size is over 150 μm, which is 4.2 % of a vane gap size in SNS RFQ, the gradient could reach over 5 % mismatch even if the RFQ wall field is well retuned. Hence, the desired vane tolerance should be less than 150 μm, since A_0 mismatch drastically increases with the perturbation size over 150 μm.

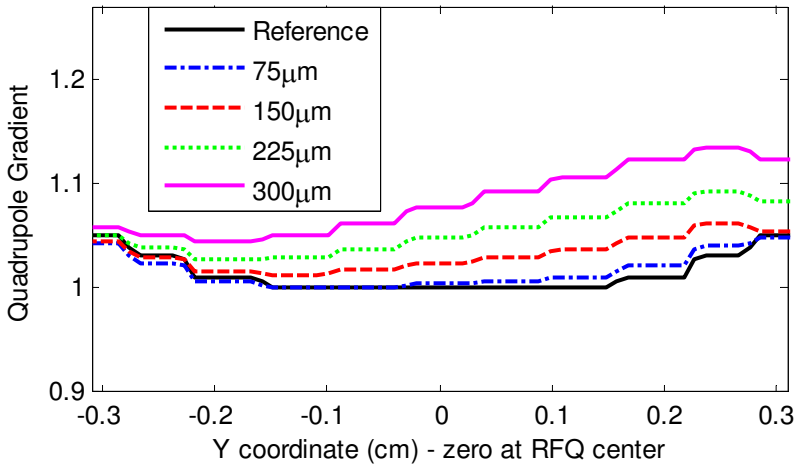

Figure 27. Quadrupole gradient by the perturbation size (Case 1, section 3).

The desired vane tolerance should be less than 150 μm in SNS RFQ

Given that the RFQ fabrication cost is very expensive and does not allow post-fabrication after the vacuum brazing process of the 4 vanes is carried out, it is important to ensure that the machining tolerance guarantees a good RFQ field distribution. Since manufacturing cost of a long RFQ is expensive (often costs more than $1M dollars), a large amount of money could be wasted if the RFQ fabrication does not achieve the desired field due to its errors. In that perspective, the perturbation study is valuable for developing RFQ fabrication with a pre-determined vane tolerance.

2.4 3D RFQ modeling for solving RFQ design issues

In the following section, we utilized the 3D RFQ simulation method to solve the real RFQ design issues. The two main design issues are the narrow mode separation and small group velocity. Although several attempts have been made by previous researchers, we suggest a more simplified engineering design that could provide a reliable and cost effective solution.

To solve the narrow mode spacing problem, we introduced an alternative RFQ cut-back design that can have potential advantages of improving the mode separation problem. The mode spectrums of these structures are thoroughly investigated as a function of the structure length, and discussed in Chapter 3.

To solve the group velocity problem, we proposed another type of coupling cell design with four cut-back resonant circuits at the coupling cell. This proposed design decreases the required coupling cell fabrication and tuning effort by half. Moreover, the new design suppresses the unwanted electromagnetic modes generated at the coupling cell which will be discussed in Chapter 3.

2.5 Conclusions

The full-scale 3D RFQ modeling and perturbation study was discussed using a SNS example. The achieved simulation accuracies are more than 99 % when compared to the measured results of a real RFQ. Investigation of a RFQ on-axis field is also possible with the 3D simulation method.

The proposed full-scale 3D RFQ modeling gives several advantages. First, the entire RFQ fabrication time and cost can be saved without building an expensive prototype model. Since our validation study proves great accuracy of long full-scale RFQ simulation, the real RFQ fabrication can directly proceed from the designer's simulation data. Second, the perturbation study can provide a design guideline by imposing a tolerance limit. Given that a malfunctioning RFQ could lead to a waste of money, the impact of this perturbation study is considered significant.

CHAPTER III

RFQ DESIGN ISSUES AND NEW DESIGN

The narrow mode separation and RF field flatness are the two main design issues that have not been addressed yet. In this chapter we will discuss the impact of designs of vane-end plates with various types of vane cut-backs in detail for widening the separation between the fundamental quadrupole and neighboring dipole modes, and maintaining RF field flatness.

3.1 Design Issue I – Narrow Mode Separation

3.1.1 Mode separation:

Problem Definition: Narrow mode separation between operating and adjacent electromagnetic modes

The TE210 quadrupole mode is the operating mode of RFQ. This quadrupole mode, however, is not the lowest order mode in RFQ, since each couple of RFQ vanes generates a dipole mode as well. The resonant frequency of dipole mode is determined by the capacitance sum of inter-vane and opposite vanes [29]. Therefore, the dipole modes are in general the lowest order mode in RFQ. Figure 28 shows the electric field plot of quadrupole and dipole modes in RFQ cross section.

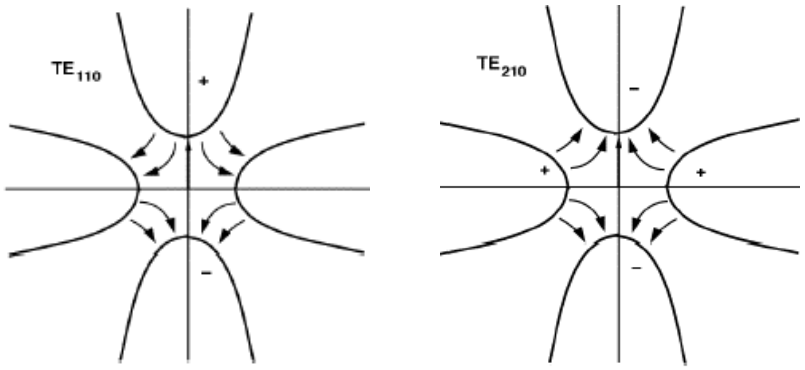

Figure 28. Electric field plot of the dipole and quadrupole modes – After [9].

Figure 29 shows an illustration of RFQ inter-vane and opposite vanes capacitance. The large inter-vane capacitance causes RFQs to have narrow frequency spacing between the quadrupole mode and the adjacent dipole modes. In other words, the opposite vanes capacitance in dipole mode becomes much smaller than the inter-vane capacitance. As a result, the quadrupole and dipole mode frequencies appear fairly close to each other.

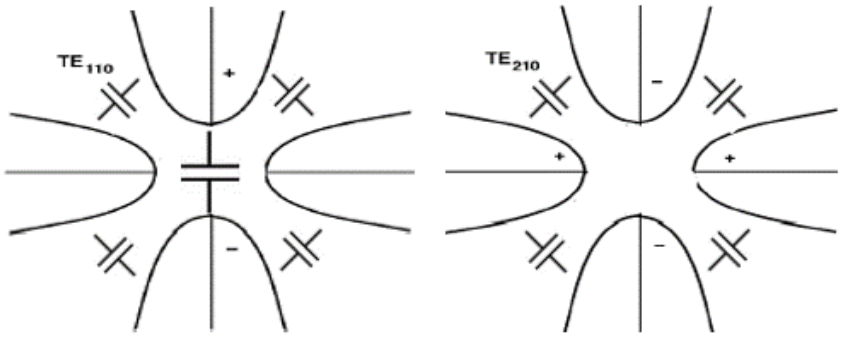

Figure 29. Vane capacitance of the dipole and quadrupole modes.

This narrow frequency spacing (separation) issue becomes more severe as RFQ length increases. The cavity higher order electromagnetic modes occur at lower frequencies upon increasing the cavity length; hence the frequency spacing between these modes is reduced. Given that the RFQ demands a much longer cavity length compared to other cavities to satisfy the requirement of very smooth change in the bunching and acceleration fields; hence this narrow spacing is a problem. For example, the SNS RFQ length is about 5 λ that is more than 10 times longer than the TM mode cavities in other acceleration sections. Hence, these modes are very dense and would create operation problems.

Figure 30 describes the associated boundary conditions used to find the *TE110*+, *TE110*-, and *TE210* modes, denoted by D_0+, D_0-*(degenerate)*, and Q_0 respectively. Precisely speaking, the fundamental quadrupole mode Q_0 is *TE210* for the circular-like geometry, and TE110 mode are the unwanted dipole mode. Therefore in this dissertation, we will follow the common RFQ mode notation of *TE110* for D_0 and *TE210* for Q_0 [7]. A realistic RFQ does not have perfect rectangular or circular cross section geometry.

The Q_0 in an RFQ (TE210) mode is utilized to provide quadrupole focusing on the beam moving along the RFQ axis. Meanwhile, both D_0*'s* generate perpendicular dipole E-fields (deflecting) that could bend straight moving particles - which should be avoided.

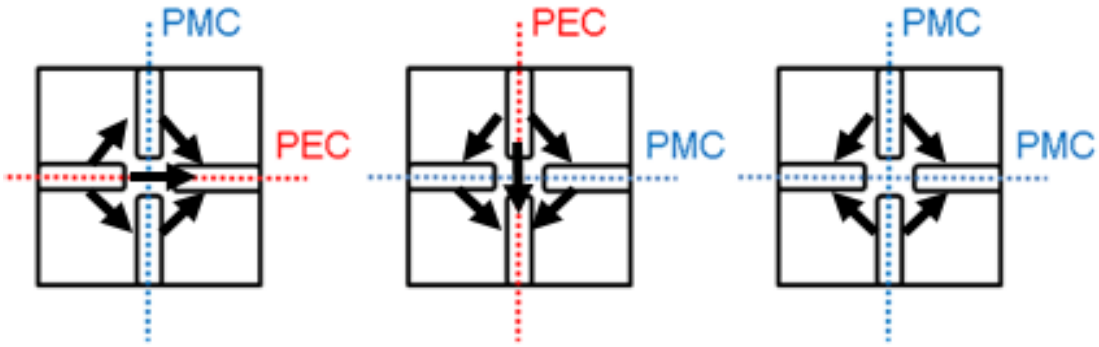

(a) (b) (c)

Figure 30. Symmetry boundary conditions of RFQ modes - (a) TE110+ (D_0+) (b) TE110- (D_0-) (c) TE210 (Q_0).

These RFQ modes have longitudinal harmonics, as well, that are denoted by: *TE11n+*, *TE11n-(degenerate),* and *TE21n* ($n \geq 0$). Mode spacing between the quadrupole mode harmonics is determined by Eq. (3) [30], after replacing the wavenumber k_n by the vane length l_v that is shown in Figure 31.

$$f_{TE_{21n}} = \frac{c}{2\pi}\sqrt{\left(\frac{2\pi}{c}\cdot f_{TE_{210}}\right)^2 + \left(\frac{n\pi}{l_v}\right)^2}, n = 0,1,2,\ldots k_n = \frac{n\pi}{l_v} \quad (3)$$

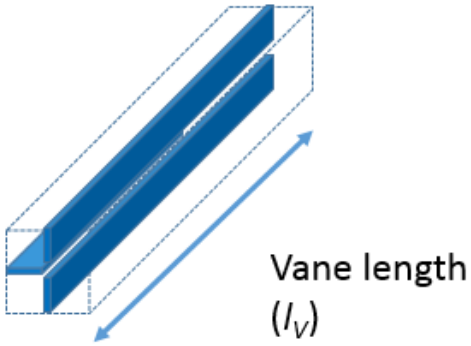

Figure 31. Definition of vane length.

where n is the harmonic mode number, f_{TE210} is the frequency of Q_0, f_{TE21n} is the frequency of Q_n. Notice here that Equation (2) suggests that the spacing between the harmonic frequencies of the quadrupole mode would be narrower for relatively long RFQs.

3.1.2 Methods to Improve Mode Separation:

As explained in the previous chapter, the most popular method to improve RFQ mode separation is to include mode stabilizer circuit such as PISL and DSR. Dipole modes are significantly affected by stabilizer circuit and can be easily shifted away from the dominant mode, hence wider mode separation can be achieved.

Another approach to increase RFQ mode separation is utilizing alternative RFQ cut-back scheme [31][32]. Conventionally, the RFQ cutback scheme is applied to all four RFQ vanes (4C) [4] to achieve both field uniformity and all quadrants symmetry. This scheme which assures the

transversal symmetry, with no doubt, has been the standard for most RFQ structures. Other possible cutback methods [31] are the double dipole (DD) and the folded dipole (FD), which have only two vane undercuts on each end. The DD RFQ employs undercuts at both ends of only two opposing vanes (Figure 32(a)) while the other two vanes are short circuited at both ends; meanwhile the FD RFQ employs an undercut on one end of each vane interleaved with the vanes with the cut-back in the other end (Figure 32(b)).

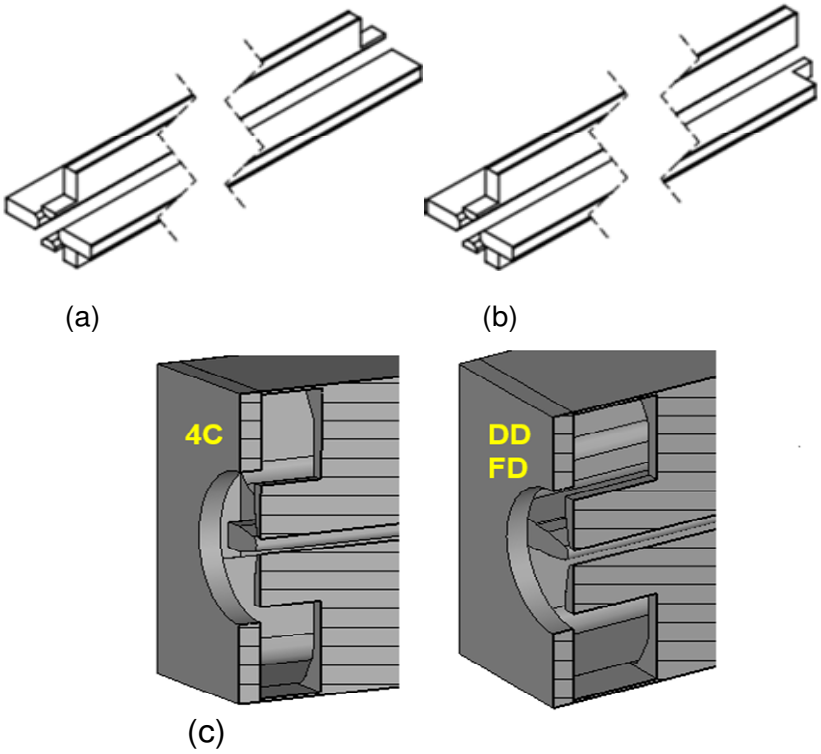

Figure 32. RFQ cut-back alternatives and end-region geometry: (a) the DD RFQ, (b) the FD RFQ, (c) end-plate design.

With DD or FD, complexity, manufacturing cost and tuning effort of these structures can be reduced since the required cut-back numbers are halved and the separation of dipole modes is readily achieved without extra effort. Although two vane-ends are short-circuited to end wall in DD and FD geometries, the transverse fields of quadrupole mode do not go to zero on vane ends because of the existence of open field path between the other two vane-ends with undercut and the end-plate. Figure 32 (c) shows end-plate design examples to realize DD and FD RFQs with minimizing the non-zero transverse E-field. The gaps between vane ends and end-plate provide open magnetic field path. The generation of an axial field at end region is a drawback of these schemes; however, Ref. [31] expected that the axial field effects could be reduced if a few input transition cells are utilized in the RFQ.

Previous Approach: Mode stabilizer designs and alternative cut-back methods have been developed and installed

3.1.3 Mode Stabilizer Limitations and Alternative Design:

The mode stabilizer circuits for mode separation improvement increases the design and fabrication costs. Although PISL method promises wide mode separation, it demands adding plenty of holes and rods. About 8% of power is dissipated in PISL rods, and it imposes a necessity of using a cooling channel design as well [5]. Moreover, the PISL rods generate parasitic capacitance near RFQ vane. Therefore, the quadrupole frequencies are also slightly shifted. The DSR decreases design and fabrication costs over PISL with drawback of reduced

mode separation. However, it still adds some design and tuning complexity beyond the baseline design.

In view of cost therefore, an alternate cut-back method could be useful for mode separation improvement. The previous work [31] is however, only done with 0.74 λ length short RFQ as shown in Figure 33. Therefore, more detailed mode separation analysis up to the common longer high power RFQ length (5 λ for SNS RFQ case) needs to be performed. Furthermore, the previous work did not give a qualitative explanation on how DD and FD RFQ dipole modes are generated and have unique mode spectrum. Understanding of these dipole properties can open new application areas of DD and FD RFQs.

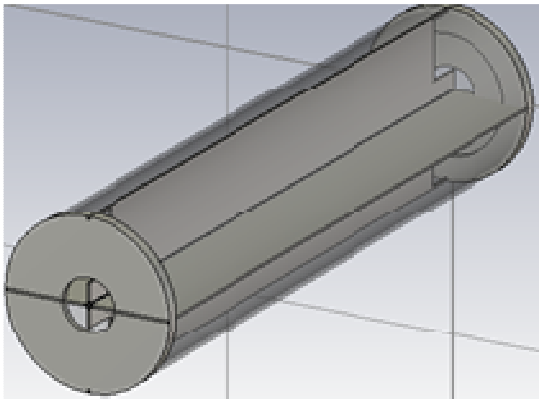

Figure 33. A short 0.74 λ length RFQ model.

Limitation of Previous Solutions: Mode stabilizer increases manufacturing and tuning costs / Alternative cut-back methods have been only demonstrated in a short length

3.1.4 Feasibility of Cut-back Methods for Long RFQs:

Here, we investigate the alternative cut-back structure up to 5 λ lengths. From this study, we will explore if these cut-back methods could even provide additional RFQ EM design options. Further discussions on dipole mode properties are also covered in this study, which are important to understand the mode spectrum that was not previously well discussed. Finally, fundamental properties of the cut-back methods are compared.

Figure 34 describes the RFQ simulation model utilized for this study. Here, we use the CST tool to calculate cavity eigen frequencies and field results. The same transverse RFQ geometry and mesh setup that was previously used for on –axis field study of SNS RFQ with good accuracy, are utilized in this study. However, in our analysis, dipole mode suppressors are not used in all the three models studied to simplify our performance prediction calculations. Based on our calculations, the SNS RFQ with a length of 5λ without a mode stabilizer has 413.9 MHz and 401.6 MHz for the Q_0 and D_0 frequencies, respectively. Several RFQ models with different longitudinal lengths have been simulated to obtain more detailed mode separation information. Figure 35 shows the details of an end-region geometry with a cut-back for this simulation.

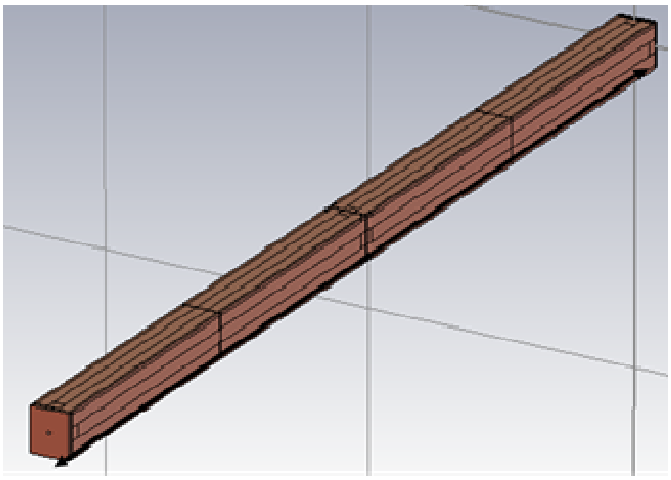

Figure 34. A 5 λ length long RFQ model.

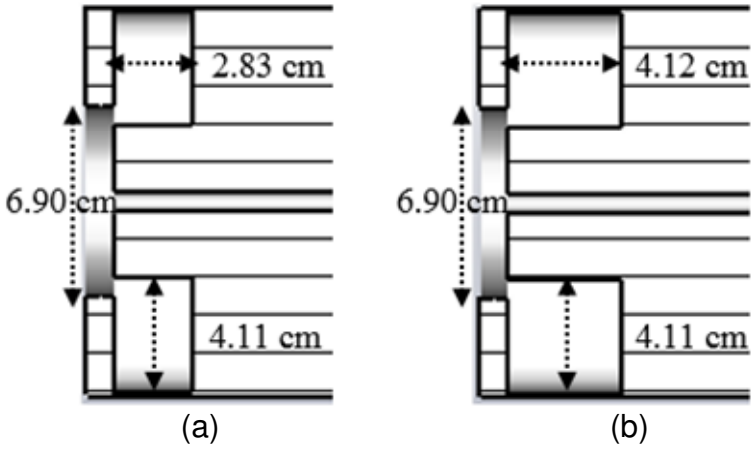

Figure 35. RFQ End-region geometry for simulation: (a) 4C, (b) DD / FD.

In the analysis, a coupling factor k_c that represents the mode separation of the RFQ structure is defined as given by [33]. k_c defines the coupling between Q_0 and D_0 modes and is given by the following expression:

$$k_c \approx \frac{f_H - f_L}{f_c} = 2\frac{f_H - f_L}{f_H + f_L} = 2\frac{f_{Q_0} - f_{D_0}}{f_{Q_0} + f_{D_0}} \quad if\ k_c << 1 \tag{3}$$

where f_H and f_L represent the highest and lowest frequency utilized for k_c definition, which are the Q_0 and D_0 mode frequencies. f_c is the center frequency of the passband. Based on the prediction of these frequencies, the coupling factor k_c is estimated to be approximately 3%.

Typically, the measured Q_0 and D_0 resonant frequencies of RFQs with similar Q_0 frequency and length are comparable whenever their mode separations are similar. This 3 % coupling factor is widely adopted in many 4-vane RFQs [29][34]. Therefore, a mode distribution (dispersion) study as a function of RFQ length can provide a useful design guideline for these alternative designs.

Detailed dispersion results of 4C, DD, and FD RFQs as function of their structure lengths are presented in Figure 36, Figure 37, and Figure 38. TE11n+ and TE11n- dipole modes have the same frequency (degenerate) for FD and 4C RFQs, but different in DD RFQ. Higher TE110+ mode frequencies can be observed in the DD RFQ compared to the 4C and FD RFQs; however in all cases, the TE110- frequency of DD RFQ is lower than the TE110+ frequency and they are not degenerate.

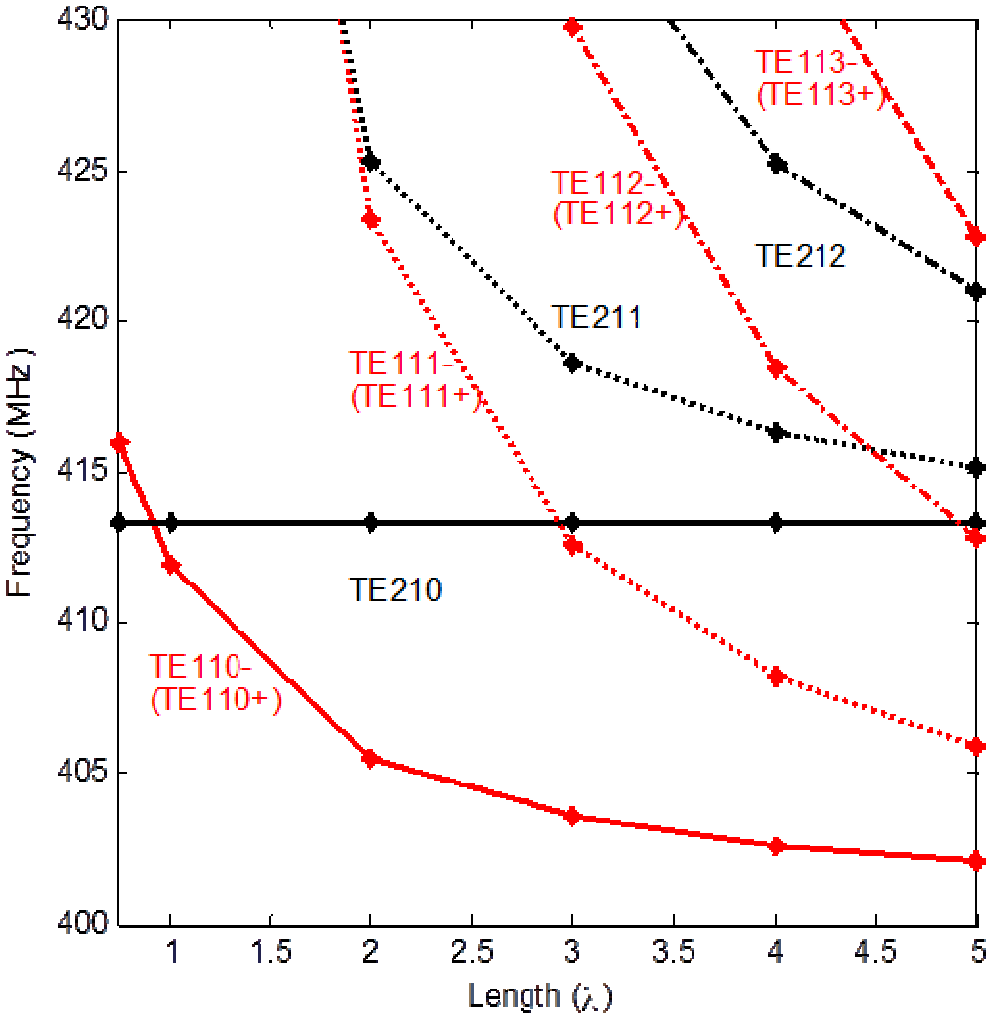

Figure 36. Resonant frequencies of the 4C RFQ modes.

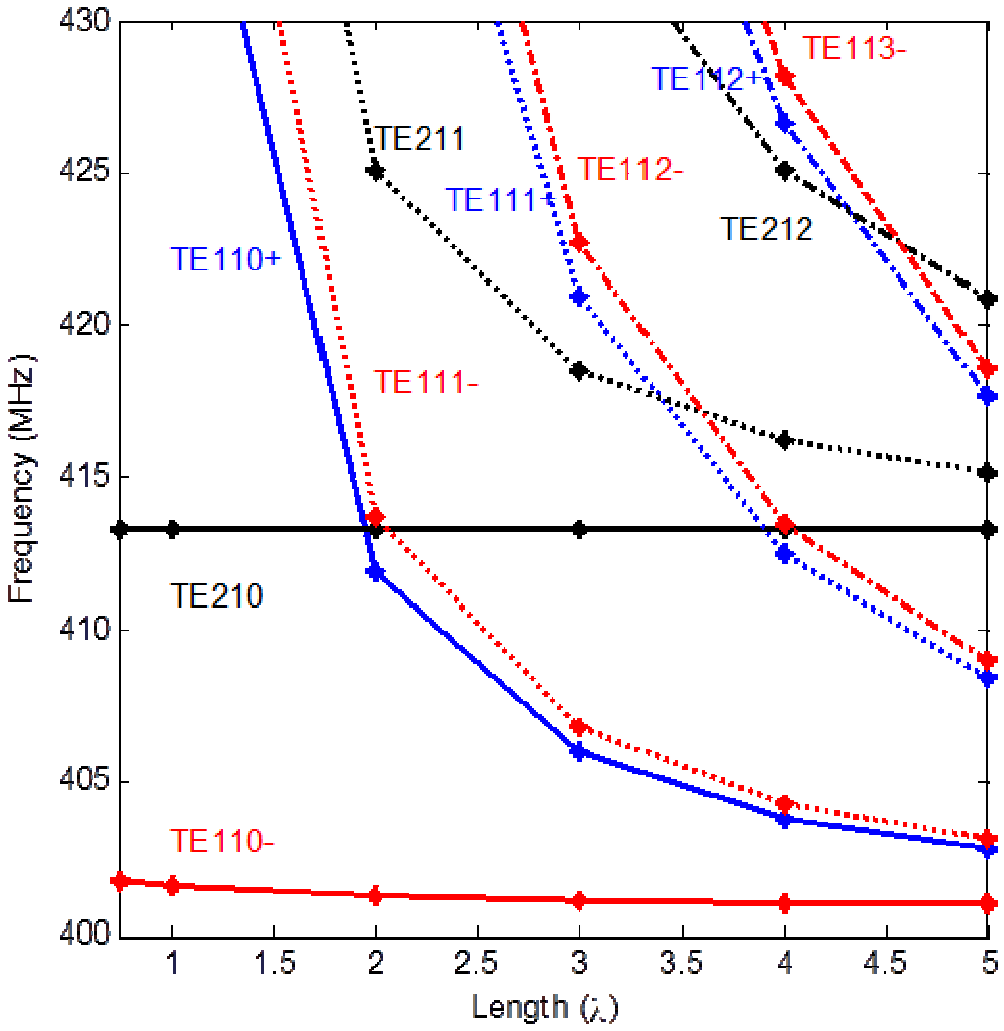

Figure 37. Resonant frequencies of the DD RFQ modes.

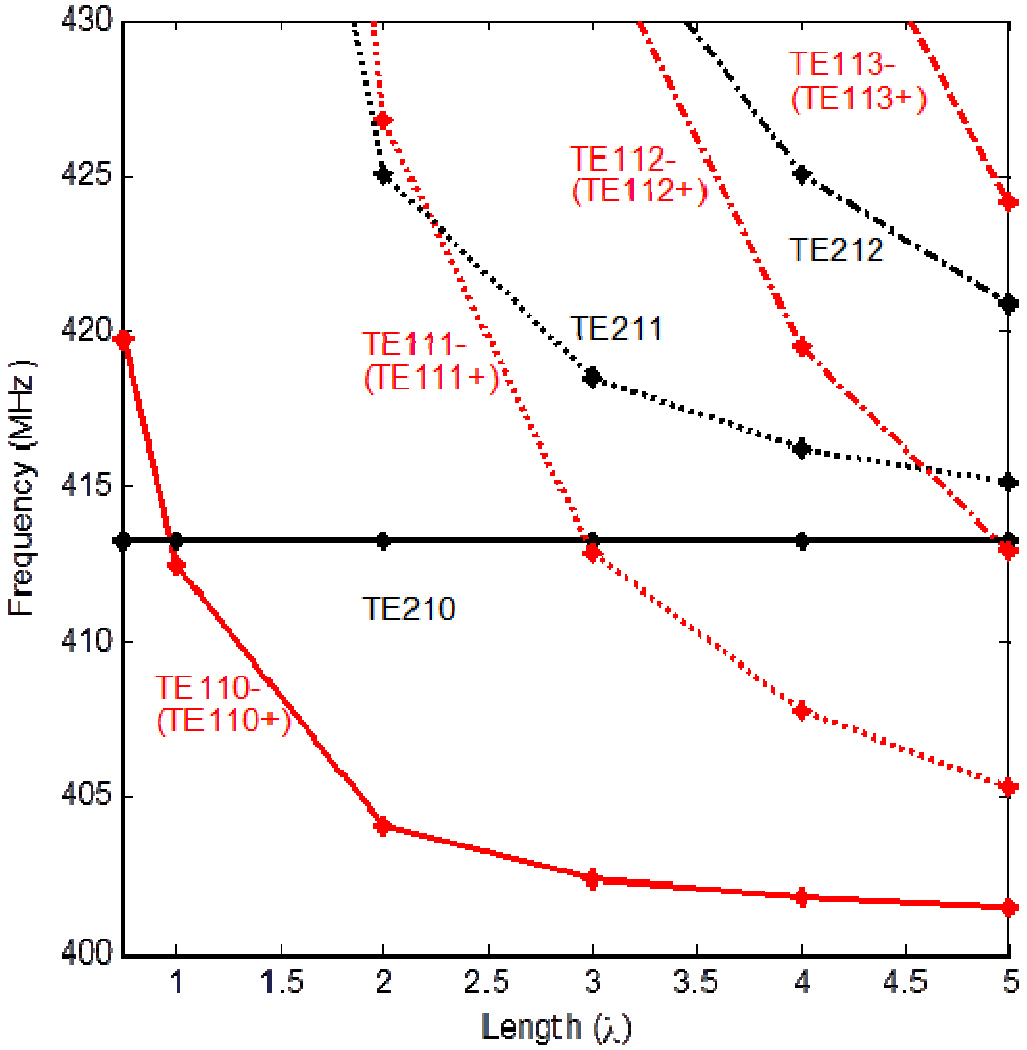

Figure 38. Resonant frequencies of the FD RFQ modes.

Wider mode spacing is always preferred since it improves field stability [2]. With a $k_c \approx 3$ %, the DD design could have wider mode spacing than the 4C RFQ with ≤1.5λ, 3λ, and 5λ structure lengths. For example, a 5λ long DD RFQ provides a 4.43MHz separation between the Q_0 adjacent to the TE112- dipole mode, which is 1.07% of the Q_0 frequency. Meanwhile, a 4C

structure gives only 0.49MHz separation which is merely 0.12% of the Q_0 frequency. Therefore, an additional dipole mode stabilizer may not be required for a 5λ long DD RFQ; thus simplifying the mechanical structure.

Applications: Some RFQs for proton accelerators are commonly built with about 5λ length, a DD RFQ design may be a good candidate for this application. For short structures $\leq 1.5\lambda$, the DD design also provides excellent mode separation. So, this short DD RFQ can also be a useful design option for a short RFQ.

Meanwhile, the FD RFQ mode spectrum does not show significant difference compared to the 4C RFQ spectrum with structure length $\geq 1.0\lambda$. Therefore, the FD design does not give obvious benefits over 4C RFQ for long structures. One possible application for the FD RFQ is for a very short RFQ of $\leq 0.5\lambda$. As it is expected from Ref. [31], the D_0 frequency is located more upward from the Q_0 frequency than that for 4C in this short FD RFQ. This short RFQ $\leq 0.5\lambda$ is usually not used for accelerators, but still suitable for other applications.

Applications: One interesting application can be an RFQ type rebuncher cavity [35]. In a very short RFQ like this RFQ rebuncher, the FD scheme may provide better mechanical strength with good mode separation.

The mode spectrum results in previous figures can be more meaningful if mode properties are understood as well. The main difference of DD and FD RFQs on dipole mode is caused by the difference in end-wall boundary conditions and the axial capacitance at end region. The short

circuit to the end-plate induces different boundary conditions to the dipole modes forming an axial capacitance; i.e. capacitive loading.

Proposed Solution and Innovation: Alternative cut-back methods in long RFQ structures

3.2 Design Issue II – Impact of Cut-backs on End Plates and DSRs on Field Distribution

3.2.1 Effect of DD and FD Scheme on Field Distribution:

The short circuit end-plate affects DD and FD RFQ dipole mode boundary conditions. Figure 39 shows end-region field plots of D_0 mode in 4C, DD, and FD RFQs. Without short circuit plate, the 4C RFQ dipole fields are formed in two diagonal RFQ quadrants as shown in Figure 39 (a). The FD RFQ dipole fields in Figure 39 (b) are similar to 4C RFQ fields, however, they are also distributed in other diagonal quadrants. Two FD RFQ end regions do not provide symmetric boundary condition to each other, hence the impedance changes like in the case of an unbalanced transmission line. This unbalanced line generates common mode currents through magnetic coupling in the cut-back region and excites fields in the other RFQ diagonal quadrants. Given that the RFQ experiences magnetic coupling in the cut-back area and electric coupling at the vane tips along the whole structure length, subsequently this magnetic coupling effect decreases as RFQ length increases. Therefore, the FD RFQ mode spectrum becomes similar to that of the 4C RFQ mode spectrum for long RFQs. From Figure 38, the FD RFQ can provide unique spectrum in $\leq 1.0\lambda$ structure length.

The DD RFQ dipoles have symmetric boundary conditions, but do not degenerate as shown in Figure 39 (c)-(d). The DD dipole modes can be understood as a combination of two dipoles with electric coupling through the RFQ vane gap. As a result, dipole fields are excited in all four RFQ quadrants with similar field intensity. The TE110- and TE210 modes in DD RFQ are equivalent to the modes oscillating with 0 and π phase advances in two electrically coupled dipole cavities, respectively.

3.2.2 Effect of DSR on Field Distribution:

End region dipole fields can be significantly affected by utilizing DSR in 4C RFQ. DSR provides an additional load in the end-cell of dipole modes, while introducing a small perturbation to quadrupole modes [12]. This additional capacitance by DSR decreases the equivalent cut-back frequency at the end region for dipole modes. Hence, dipole field distribution can be more uniform and changes dipole frequency. Figure 39 (e) describes how the dipole field profile changes by the DSR stabilization method.

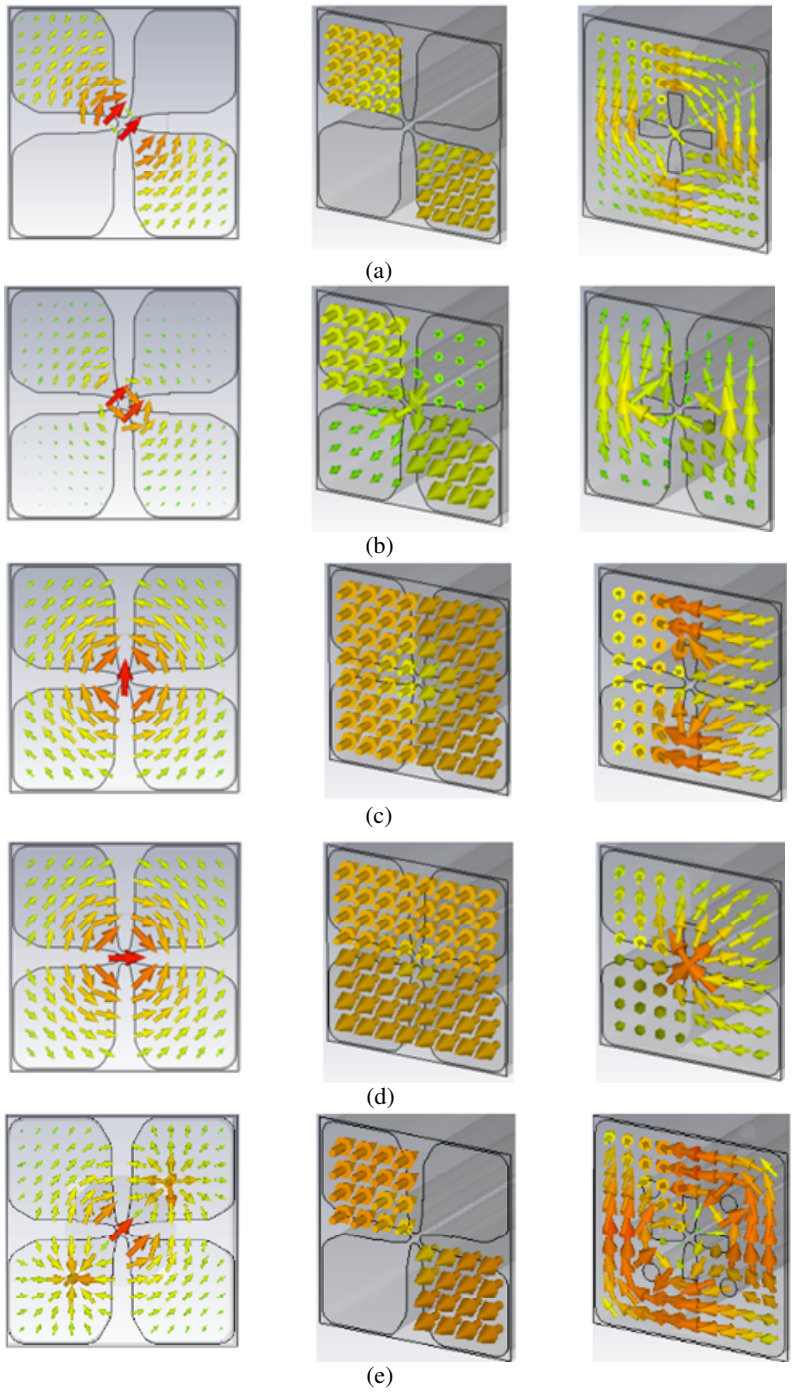

Figure 39. Fields at D0 mode- E field / H field / H field at cut-back: (a) 4C (TE110-), (b) FD (TE110-), (c) DD (TE110-), (d) DD (TE110+), (e) 4C with DSR (TE110-).

In DD RFQ, TE110- has open circuit-like condition while TE110+ experiences a short circuit-like condition at both ends. As a result, these two dipoles have different mode frequencies. One interesting observation from Figure 37 is that the mode frequency of open dipoles (TE11n-) has about a harmonic order difference from the frequency of short dipoles (TE11n+) in DD RFQs. In other words,

$$f_{TE_{11n+}} \cong f_{TE_{11(n+1)-}} \cong \frac{c}{2\pi}\sqrt{\left(\frac{2\pi}{c}\cdot f_{TE_{110-}}\right)^2 + \left(\frac{(n+1)\pi}{l_v}\right)^2}, n = 0,1,2,.. \; k_n = \frac{n\pi}{l_v} \quad (4)$$

The open circuit dipole TE110- is equivalent to the waveguide mode, while the short circuit dipole TE110+ is comparable to the cavity mode with a short end wall. Therefore, this condition of Eqn. (4) generally holds unless the TE110- field distribution is not generally uniform. Because of this relation, the mode spectrum in DD RFQ is not complex though the two dipoles are not degenerate.

A simulation is performed for shortened version of the SNS RFQ model for one λ length. The simulated result in Figure 40 verifies the mode spectrum observation. It was found that the two degenerate 4C dipoles have the same distribution pattern, while FD dipoles do not have a symmetric pattern. As expected before, DD open dipole (TE110-) shows rather flat field distribution while short dipole (TE110+) exhibits sinusoidal-like distribution. However, the 4C dipole field distribution becomes uniform with DSR utilization.

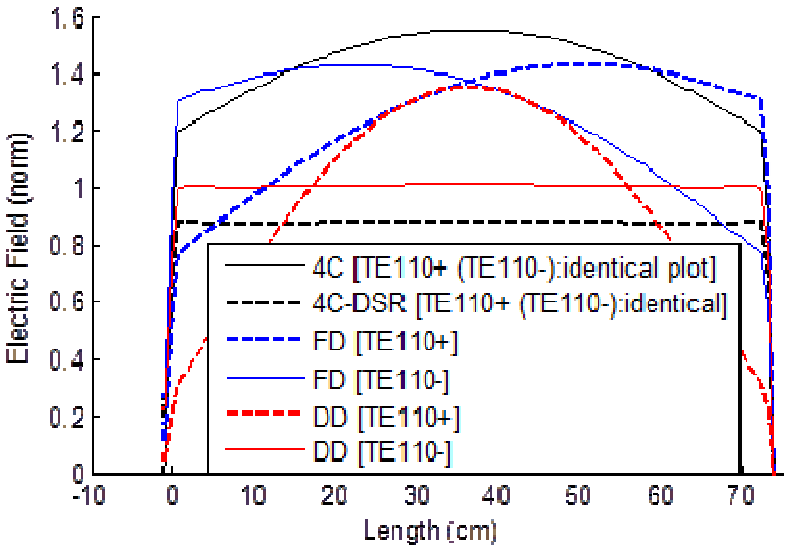

Figure 40. Dipole field distribution in 0.7 m (1 λ) RFQ length.

In a 4C RFQ, the end-plate longitudinal potential on beam axis of Q_0 is almost zero if all four vanes have perfect electrical field symmetry [26]. On the end-plate beam axis, the RF voltage induced by one vane pair is cancelled by the RF voltage produced by the other vane pair with 180º out of phase. This cancellation also occurs in D_0 that has 90º phase difference as well; hence the 4C RFQ does not have significant axial capacitance in both Q_0 and D_0.

In DD RFQ, the same RF potential cancellation appears in D_0, but not in Q_0. In Q_0, the end-plate potential becomes similar to the potential of electrically shorted vanes. As a result, the shorted vane pair cannot generate much RF capacitance and the net capacitance on beam axis has a finite value. Figure 41 shows the z-direction on-axis electric field (E_z) maps of 4C and DD RFQ end region. The red and blue color represent the E_z phase of the positive and negative

maxima. The green color represent the zero field area. As shown in the Figure 41 (b) right, the phases of vertical vanes and horizontal vanes - represented with red and light blue color, respectively - are not symmetrical in DD Q_0 mode.

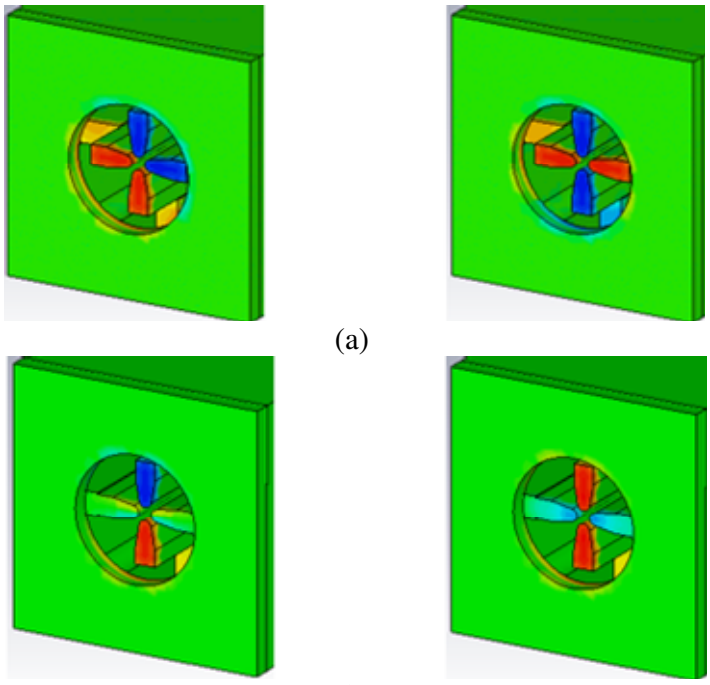

(a)

(b)

Figure 41. End-region E_z field in D_0 / Q_0 mode: (a) 4C, (b) DD. The red and blue colors represent the E_z phase of the positive and negative maxima.

3.2.3 Effect of End-Plate Cutback Axial Field Capacitance on Field Flatness:

Due to the finite axial capacitance in DD RFQ Q_0 mode, it was pointed out [31] that axial field generation is expected. Here, we will discuss this axial capacitance and how it can affect on field flatness and mode spectrum.

Figure 42 shows the equivalent circuit view of RFQ end-region with vane cut-back. The axial capacitance C_{axis} is zero in 4C RFQ Q_0, and the cut-back frequency is determined by the cut-back inductance L and the cut-back capacitance C in both Q_0 and D_0. On the other hand, C_{axis} is not zero in DD RFQ Q_0. Therefore, the cut-back capacitance in Q_0 is actually determined by subtraction of C_{axis} from C while the cut-back capacitance in D_0 (TE110- open dipole) is equivalent to C. The results are summarized in Table 4.

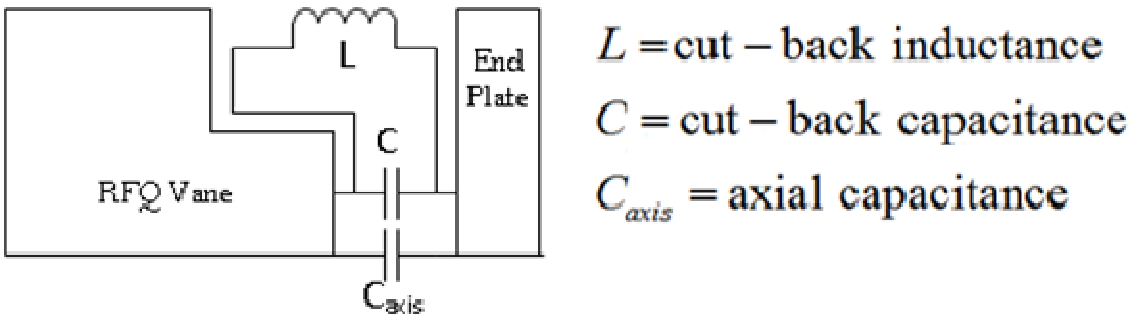

Figure 42. Cut-back equivalent circuit with axial capacitance.

Table 4. Axial capacitance and cut-back frequency.

Quadrupole (4C) – TE210	*Quadrupole (DD) – TE210*
$C_{axis} \cong 0$ $\omega_Q = (LC)^{-1/2}$	$C_{axis} \neq 0, \quad C_{eff} = C - C_{axis}$ $\omega_Q = (LC_{eff})^{-1/2}$
Dipole (4C) – TE110	***Dipole (DD) – TE110-***
$C_{axis} \cong 0$ $\omega_D \neq (LC)^{-1/2}$	$C_{axis} \cong 0$ $\omega_D \cong (LC)^{-1/2}$

In 4C RFQ, once the cut-back frequency is matched to the body Q_0 frequency ω_Q, this cut-back obviously still does not provide a uniform field profile in D_0 because of the frequency difference between the two modes.

In DD RFQ, the cut-back frequency is matched to the body Q_0 frequency ω_Q with the effective capacitance C_{eff}, but in D_0 (TE110-) the cut-back capacitance changes to C. Since $C_{eff} < C$, this cut-back frequency becomes lower in D_0 (TE110-). For most RFQs with Q_0 frequency > D_0 (TE110-) frequency, this capacitance difference can provide a flatter dipole field distribution in the DD case. Obviously, DD dipole frequencies do not have the same frequencies as the 4C dipole frequencies.

3.3 Impact of the Study

The Results of this Study can decrease RFQ design and fabrication cost

In long RFQ structures, DD can have two advantages compared to stabilizer designs. First, DD scheme is obviously simpler hence we can save design time, fabrication and tuning costs. Second, DD may enhance the mechanical reliability in the long term operation due to its simplicity. Therefore, the potential DD RFQ applications could be: 1) a low cost RFQ, 2) a continuous wave (CW) RFQ or pulsed wave RFQ with low peak electric field, 3) an RFQ that requires a long term reliability. For these purposes, DD can be utilized if DD gives superior mode separation over 4C cut-back method in a given RFQ length. Table 5 shows a comparison between the three RFQ cut-back schemes in view of mode separation and the applicable length range.

Table 5. Comparison of RFQ cut-back schemes.

	4C	***DD***	***FD***
Mode separation at $f_{Q0} \approx 413$MHz, kc ≈ 3%	Good for ≈2λ, 4λ	Good for <1λ,≈3λ, 5λ	Good for <1λ, ≈2λ, 4λ
Length Acceptable	Long	Long / Short	Short

Table 6. Comparison of DD and 4C + DSR schemes.

	DD	*4C + (DSR)*
Design complexity	Low	Moderate
Tuning effort	Low	Moderate
Power dissipation	Moderate	Moderate
On-axis field	High	Low
Peak electric field	High	Low
Rod modes	N/A	Exist (N/A if no DSR)
Applicability (By length)	Length dependent	All RFQ lengths

Table 6 shows a comparison between the DD and 4C with DSR RFQs. DD RFQ has advantages of a simple design, fabrication and tuning. Meanwhile, it also has disadvantages of increasing on-axis field and peak electric field slightly. For low cost applications, DD method can be considered with a superior mode separation above 4C RFQ.

3.4 Conclusion

The alternative cut-back design is simple and cost effective / It also mechanically more stable

The alternative cut-back structures are investigated and analyzed in detail to solve the narrow mode separation problem of long RFQs with providing simple and cost effective design

guidelines. The simulation and analysis results clearly show that extra mode stabilizer circuit is not necessary with the proposed designs at some specific lengths. Therefore, the traditional 4C and alternative FD and DD can be selectively utilized based on our proposed design guideline that clarifies the expected mode separation by RFQ length.

The proposed DD RFQ design is promising because it is able to eliminate the extra stabilizer circuit design in most applications where the 4C design is not. Moreover, DD structure is mechanically simpler and reduces the tuning and high-precision fabrication costs around the cut-back area by half. Furthermore, our analysis clearly proves that the non-degenerating dipole modes in DD RFQ are not a practical design concern at all.

The FD design is useful and interesting solution for short RFQ and RFQ buncher cavity. Our work demonstrates that this design can provide the largest mode separation in a short RFQ structure ($< 0.7\ \lambda$). Also it adds mechanical strength of short RFQ that could not be achieved by 4C method.

3.5 Design Issue II – Small Group Velocity

The RFQ is designed to operate in a standing wave with reduced group velocity. Such condition may make the design very sensitive to fabrication tolerance. In this Chapter we proposed a modified coupling scheme between the different RFQ sections to reduce such sensitivity.

3.5.1 Coupling Problem between Beam Particles and RF Field:

RFQ is by far the only accelerating cavity operating with TE mode with respect to the particle beam axis. The required TM mode for the acceleration is formed microscopically at only around the vane tip area. The TE mode operation enables the overall field uniformity without wavelength dependency and strong focusing field formation. The SW cavity design is required in RFQ system because the field uniformity cannot be obtained in a travelling wave with the TE mode operation near waveguide cutoff frequency [2][36].

However, SW resonant cavities tend to have small group velocity of electromagnetic wave that becomes almost zero in long RFQ structures. Since the group velocity is a measure of energy flow velocity, near zero group velocity means that perturbed local field is not compensated by electromagnetic energy flow quickly. As a result, SW cavities are very sensitive to local perturbations.

In SW cavity the RFQ can be considered as a quadruple ridge waveguide operating at the cutoff frequency of its TE quadrupole mode. The waveguide wavelength λ_g is given by [36]

$$\lambda_g = \frac{2\pi}{\beta_g} = \frac{2\pi}{\beta_0\sqrt{1-(f_c/f)^2}} = \frac{\lambda_0}{\sqrt{1-(f_c/f)^2}}$$

$$when \quad f = f_c \ , \qquad \lambda_g \approx \infty \ , \qquad \beta_g \approx 0 \tag{5}$$

where β_g is the operating mode propagation constant, f_c is its cutoff frequency, and when the RFQ operates at the cutoff frequency that is the case of the standing wave operation, the mode has an infinite guided wavelength λ_g.

Energy velocity is small, hence very sensitive to perturbation

In an RFQ structure, an infinitesimal β_g translates to a large phase velocity, and a very small group velocity – i.e. standing wave. The cutoff frequency depends on the transverse dimensions of the waveguide geometry, and is very sensitive to any dimensional errors. Hence, any slight perturbation in the mechanical structure could cause significant field non-uniformity along the RFQ structure thus leading to mode instability.

3.5.2 State-of-the Art Approaches and their Limitations:

An example of the very long coupled RFQ constructed previously was introduced in Chapter 2 (shown in Figure 17). This RFQ was for the Low Energy Demonstration Accelerator (LEDA) project and had 8 meter length with four coupling cells. The designers came up with the idea of each coupling cell with 8 vane cut-backs on RFQ coupling cell area. However, the coupling cell design is rather complex because the fabrication and tuning of 8 cut-backs around the coupling cell is not simple. As a result, the manufacturing and tuning costs can be expensive. Figure 43 shows the complexity of coupling cell design.

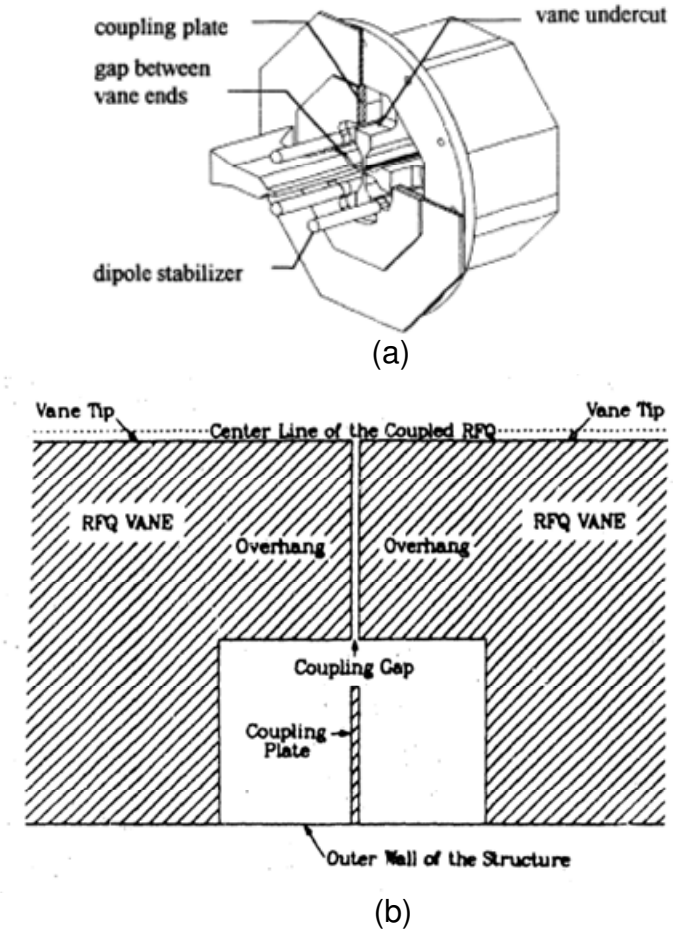

Figure 43. Coupling cell design: (a) perspective view, (b) cut-view - After [13][14].

RFQ coupling cell which requires 8 cut-backs is designed and realized. However it increases manufacturing and tuning costs. Also it generates unnecessary modes

In addition to increasing the design complexity, the coupling cell also generates an unwanted electromagnetic coupling gap mode near the operating quadrupole mode. Upon adding the coupling gap there are three TM-like modes those can be generated in the RFQ as described in

Figure 44 [26]: end mode, coupling gap mode, and coupling plate mode. The end mode in Figure 44 (a) appears at RFQ end plate. The coupling plate mode in Figure 44 (c) is the degenerate forward wave mode with the operating mode of coupled RFQ. Meanwhile, the coupling gap mode in Figure 44 (b) is an unnecessary mode that is our concern. Unfortunately, this coupling gap mode frequency can show up close to the operating quadrupole frequency. Therefore separation of this mode put another limitation on coupled RFQ design.

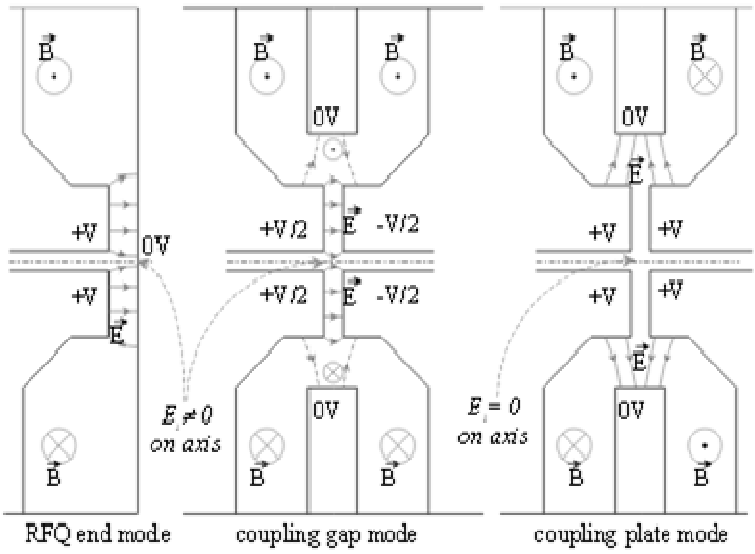

(a) (b) (c)

Figure 44. Extra RFQ modes generated at: (a) end, (b) coupling gap, (c) coupling plate [degenerate] - After [26].

3.5.3 Proposed Solution and Innovation:

The complexity of coupling cell design could be significantly reduced if the number of required cut-back decreases. Based on this, we propose another coupling cell design with DD cut-back. As shown in Figure 45, the required cut-back numbers are halved by this design. Another expected advantage from this proposed design is that this design can be mechanically more stable. Since a vane pair does not need undercut, the possibility of mechanical deformation by manufacturing could be reduced. Moreover, the unwanted coupling gap mode discussed in Figure 44 (b) can be suppressed by a DD coupling cell. Because of the short circuit condition of two vanes at the coupling plate in the middle, this coupling gap mode frequency moves to much higher frequency.

Utilize a new simple coupling cell design

One potential drawback of this design is that the coupling is realized with only two vanes at the coupling cell. Naturally, the required coupling strength becomes smaller than 4C coupling RFQ. Therefore, the coupling gap size needs to be smaller in DD coupling cell design.

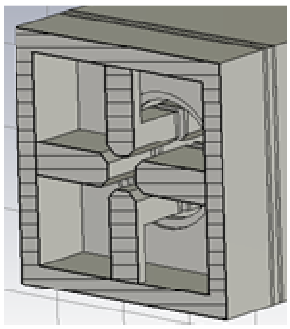

Figure 45. DD coupling cell.

3.6 Proposed Design Concept Validation:

To verify this proposed idea, a simulation of RFQ model with a compact model of 36in length is created and is shown in Figure 46. The coupling cell design in Figure 45 is located in the middle of this RFQ model. To reduce fabrication cost of this model, the vane to vane capacitance of this model is intentionally designed to have smaller value than SNS RFQ to relieve the requirement of very precise machining. Given that the tolerance requirement of real RFQs are in the μm range, this low capacitance model helps to relieve the tolerance requirement significantly. However, the expected operating quadrupole frequency is 1363 MHz that is about three times higher than SNS RFQ.

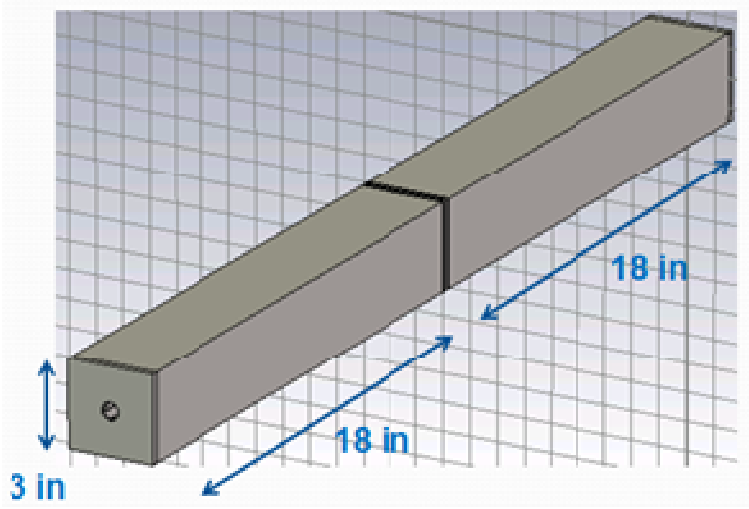

Figure 46. A conceptual model with DD coupling cell.

3.6.1 Mode Separation Advantages:

Table 7 shows mode frequencies of the 36in model without utilizing the coupling cell design that was calculated using CST tool. The dipole separation of 4C RFQ is good with this length, however, only 3 MHz separation is obtained in DD RFQ. The second harmonic of the short circuit dipole (Dipole S) is the nearest mode to the DD quadrupole mode. Open dipole modes (Dipole O) are not a concern in this case.

Table 7. Mode frequencies distribution - 4C and DD, uncoupled.

Mode number	*4C [MHz] (Quadrupole)*	*4C [MHz] (Dipole)*	*DD [MHz] (Quadrupole)*	*DD [MHz] (Dipole O)*	*DD [MHz] (Dipole S)*
0	1363	1288	1364	1285	1291
1	1374	1309	1374	1299	1320
2	1402	1344	1401	1329	1367
3	1447	1394	1445	1376	1429

The results of the coupled DD RFQ are summarized in Table 8. Similar to the 4C coupled RFQ design, DD RFQ quadrupole mode separation is improved from 11 MHz to 19 MHz with the coupling cell. Better dipole separation could be also observed from 3 MHz to 36 MHz. As expected, no coupling gap mode is observed around RFQ operating mode.

Table 8. Mode frequency distribution - DD, coupled.

Mode number (*π phase advance)*	*[MHz]* *Quadrupole*	*[MHz]* *Dipole O*	*[MHz]* *Dipole S*
-0.5	1341	1274	
0	1363	1285	1318
+0.5	1382	1314	1319
+1	1399	1327	1421
+1.5	1479	1418	1427
+2.0	1499	1433	1578

3.6.2 Electric Field Distribution:

The expected electric field distribution of the operating quadrupole mode is shown in Figure 47. This simulation assumes a perfect transverse symmetry of the RFQ quadrants, hence the real measurement may contain some errors due to vane misalignment, surface roughness, and fabrication errors. Practically, no serious discontinuities of the electric field at the coupling gap area should be observed to ensure that these two RFQ sections are actually coupled.

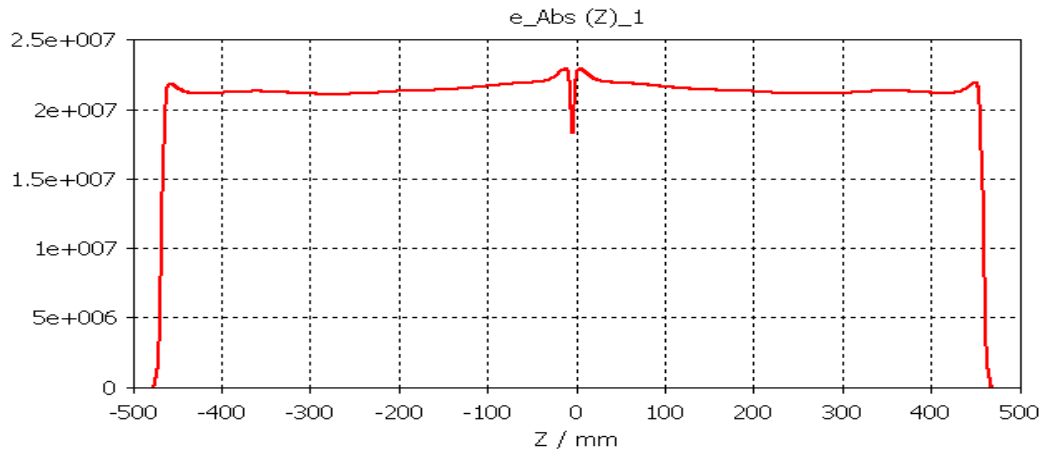

Figure 47. Simulated field profile - quadrupole mode.

3.7 Experimental Validation

A test DD coupled RFQ model is designed and built with the same internal geometry that was utilized for the calculations above. But, the finalized structure contains several holes to place slug tuners and couplers as shown in Figure 48. Because of the existence of these holes, the expected resonance frequency is decreased from 1363 MHz to 1355 MHz as they were not accounted for. Table 9 shows the shifted mode frequencies with holes. These frequencies are expected to be seen when we carry out real measurements.

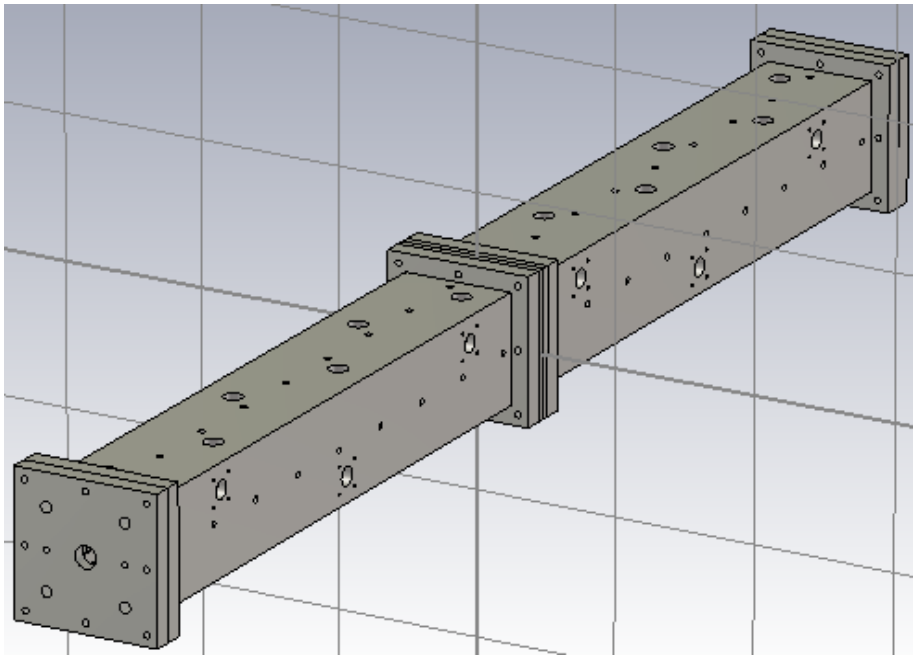

Figure 48. A Finalized model with DD coupling cell.

Table 9. Mode frequency with holes.

Mode number ***(π phase advance)***	***[MHz]*** ***Quadrupole***	***[MHz]*** ***Dipole O***	***[MHz]*** ***Dipole S***
-0.5	1329.32	1264.84	
0	1354.81	1277.54	1310.64
+0.5	1373.18	1305.14	1312.37
+1	1389.84	1318.83	1414.47

A detailed mechanical design of this RFQ is performed with the 3D mechanical CAD tool Solidworks [37]. Figure 49 describes the key parts and assembly design. As explained, extra surface holes for RF coupler and tuner ports are also created for low power RF measurement. End plate holes are utilized for bead-pull measurement.

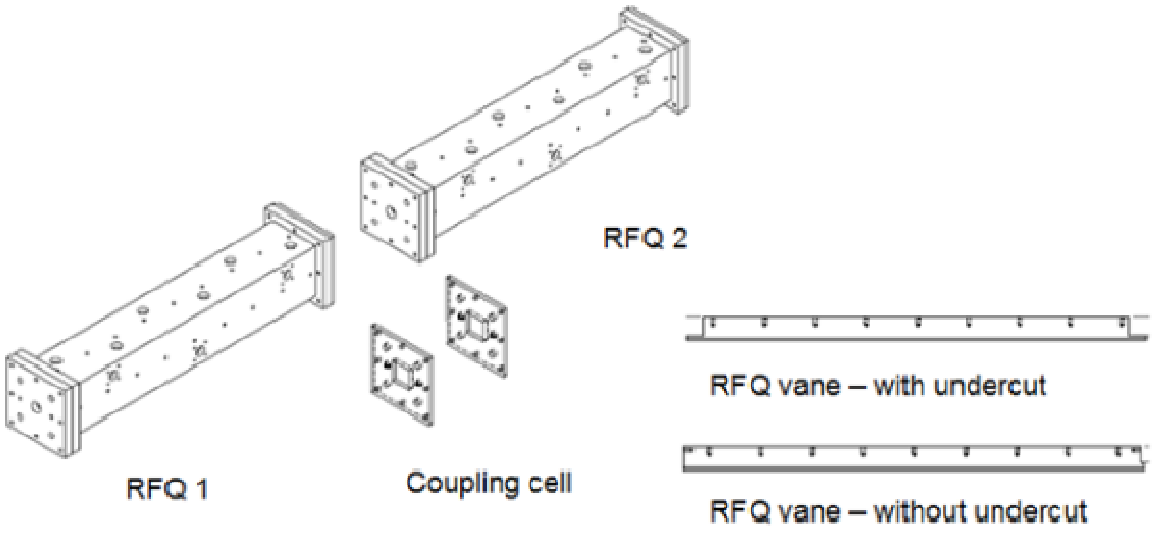

Figure 49. Detailed mechanical design of coupled DD RFQ model.

The fabricated RFQ parts are shown in Figure 50. These pieces are fabricated with Aluminum material to save fabrication costs. Two RFQ body assemblies are connected together via coupling plate.

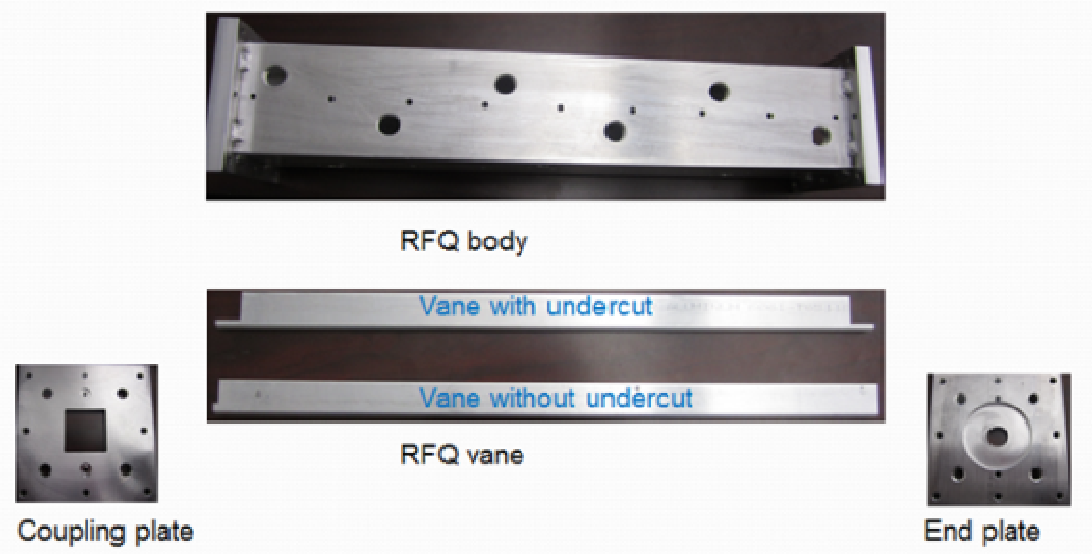

Figure 50. Fabricated coupled DD RFQ model.

The previous simulation results are validated with RF measurements. First, the frequency measurement is done to see that the designed coupled RFQ has similar resonance points to the simulated results. Second, the bead-pull measurement is performed to check if the RFQ operating mode is the real coupled quadrupole mode.

The S-parameter measurement system setup is shown in Figure 51. S21 is measured through two SMA connector ports to determine the resonant frequency. Several tuner bolts are inserted to tune non-ideal RFQ fields, which is mainly caused by vane misalignments and fabrication errors.

The measured frequency results are shown in Table 10 and Figure 52. All measured frequencies have less than 0.65% error. The first coupled quadrupole mode – Quadrupole (1) in Table 10 – gives more error than other coupled quadrupole modes such as Quadrupole (2) and

(3). Ideally, the operating mode ‘Quadrupole (2)’ should have the same mode spacing from the adjacent ‘Quadrupole (1)’ and ‘Quadrupole (3)’ modes. This is because the ‘Quadrupole (2)’ mode is the coupled mode at which two electromagnetic dispersion curve combines. ‘Quadrupole (1)’ and ‘Quadrupole (3)’ lies on the dispersion curve of coupling cell and RFQ body mode.

However, the measured mode spacing result is not very symmetric. This implies that the combined dispersion curve of RFQ body and coupling cell is not ideal due to fabrication and assembly errors. Due to the bolt and nut joint of two metal pieces that were utilized in this coupling cell demonstration model, the surface gap and RF loss between metal pieces decreased the coupling strength than ideal simulation model.

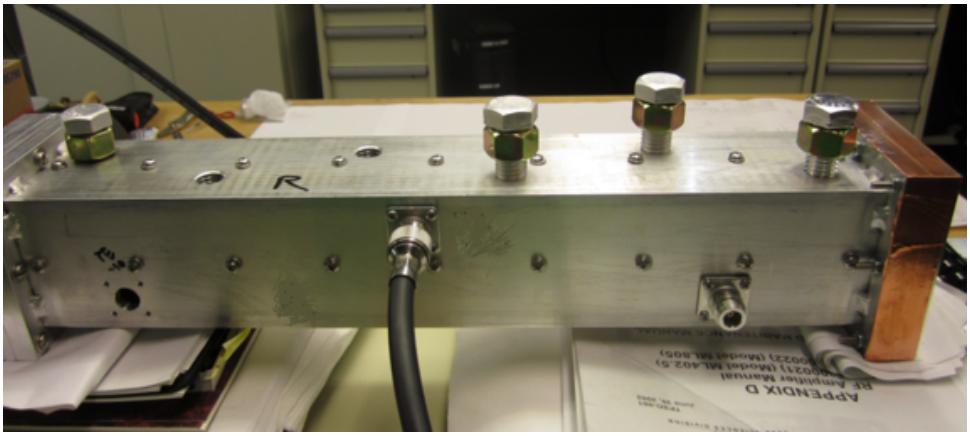

Figure 51. Measurement setup - frequency.

Table 10. Simulation vs. Measurement - coupled DD RFQ mode frequency.

Mode	*Simulation [MHz]*	*Measurement [MHz]*	*Error [%]*
Dipole O (1)	1264.84	1271.73	0.54
Dipole O (2)	1277.54	1279.84	0.18
Dipole O (3)	1305.14	1302.26	0.22
Dipole S (1)	1310.64	1304.26	0.49
Dipole S (2)	1312.37	1311.06	0.10
Dipole O (4)	1318.83	1321.47	0.20
Quadrupole (1)	1329.32	1337.88	0.64
Quadrupole (2)	1354.81	1352.29	0.18
Quadrupole (3)	1373.18	1373.50	0.02
Quadrupole (4)	1389.84	1387.51	0.17

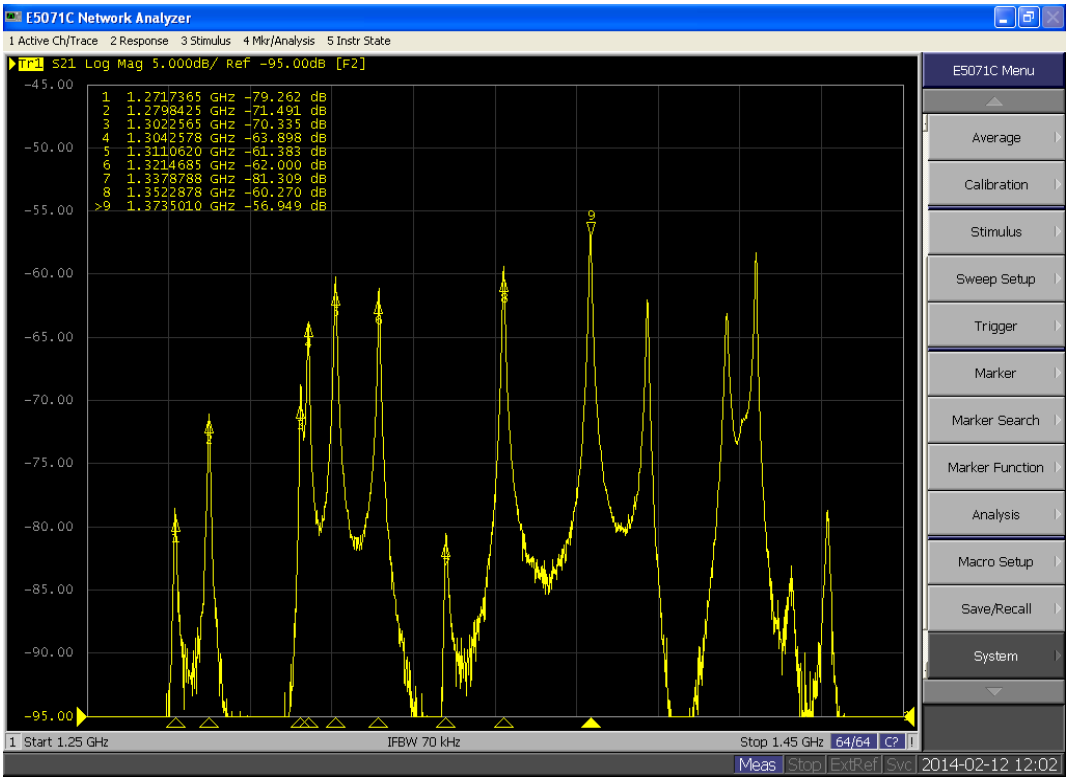

Figure 52. Measured mode frequency - coupled DD RFQ.

The bead-pull measurement is also performed to make sure that the 'Quadrupole (2)' mode is the real operating mode. The system setup is shown in Figure 53 and Figure 54. A metallic bead on the fishing line is pulled off from the RFQ upstream to downstream. The bead movement is realized by a step motor, which is controlled by LabView [38] program. A metal bead perturbation changes electric stored energy in RFQ [39], and it results in the frequency and phase changes. Here, phase changes are measured and they are utilized to calculate the electric stored energy and field in RFQ. More details of bead-pull measurement can be found in APPENDIX A.

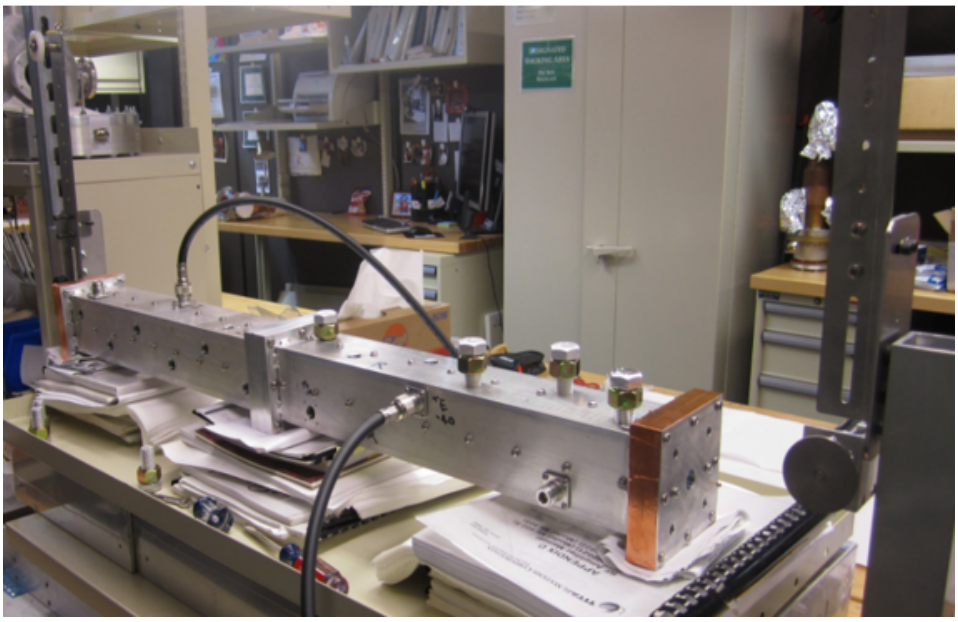

Figure 53. Measurement setup - bead-pull.

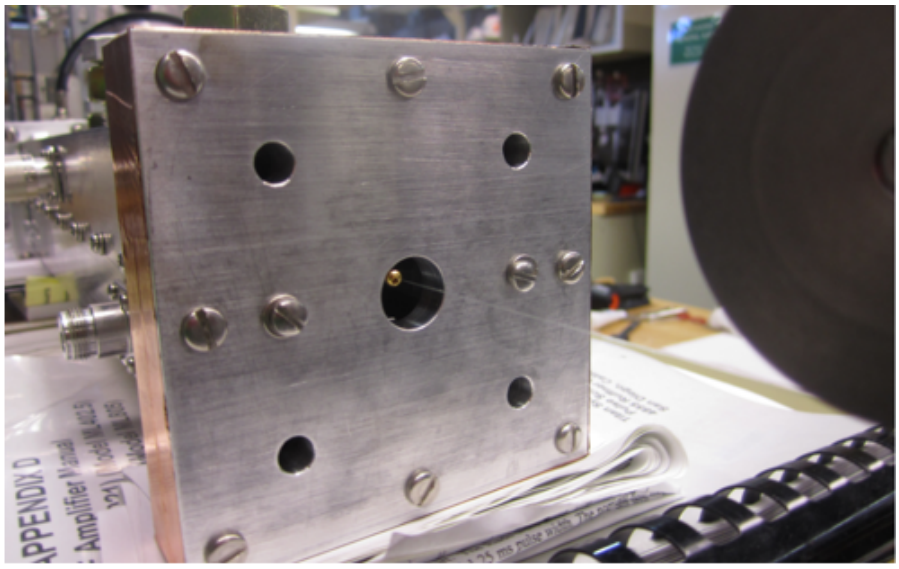

Figure 54. Bead perturbation.

The measured electric field profile at the operating quadrupole mode is shown in Figure 55. The profile is normalized by the reference field of uniform distribution. The field profile is not very uniform due to fabrication and assembly errors. It is clearly seen, however, the electric field does not have a discontinuity at the coupling cell area. In other words, this RFQ mode is obviously the coupled quadrupole mode. Because of unideal coupling gap, the field notch at the coupling cell is larger than the ideal simulation result in Figure 47.

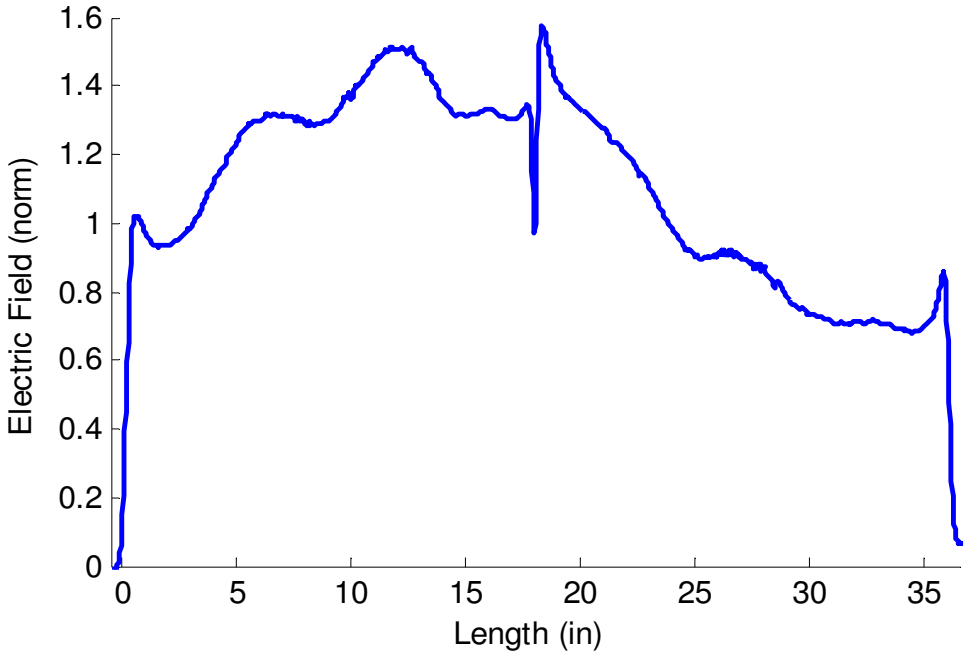

Figure 55. Measured field profile - quadrupole mode.

3.8 Conclusion

The new coupling cell design is simple and cost effective / It also separates unwanted modes

The coupled RFQ design study with an example model verifies that this type of RFQ design can be used in future coupling RFQ design. The measurement results are in good agreement with simulations. Therefore, this coupling RFQ design with two vane cut-back can be considered as a potential high energy RFQ structure.

The proposed coupled RFQ design could be promising because it decreases the required cut-back and tuning efforts in half. Moreover, it suppresses the unwanted coupling gap mode far away from the operating quadrupole mode.

CHAPTER IV

MEDIUM ENERGY BEAM TRANSPORT "MEBT" SECTION

Currently the rebuncher cavity utilized at 400 MHz with 2.5MeV energy- which is located at the front end section of the 1 GeV energy H- ion accelerator- suffers from relatively high gap voltage and peak electric field which may create X-ray radiation. A double gap microwave rebuncher cavity is proposed here to eliminate the possibility of any X-ray radiation.

A detailed electromagnetic model of the proposed double-gap microwave rebuncher cavity is presented here and validated by extensive simulations. This design is intended to decrease both the gap voltage and peak electric field. For model validation, a low cost 1/2 scaled aluminum cavity double gap model was built and tested. Mode frequencies and quality factors of the model were also measured and compared to our simulation. Additionally, bead perturbation method was used to measure the para-axial electric field. Simulation of the single and double gap cavities were compared to measurements and were in good agreement. Subsequently, guidelines have been developed to design the double gap rebuncher and optimize its gap size for lower electric field and subsequently reduced X-ray radiation.

4.1 MEBT Background

Some MEBT cavities emit X-radiation under poor vacuum because of high gap voltage and field.

In SNS accelerator, the front-end section which is comprised of ion source, LEBT, RFQ, and MEBT systems is not shielded and placed outside the concrete tunnel for easy access. Although initial system design assessed the area and concluded that it was safe with negligible radiation, some unsafe radiation was detected randomly. As a result, the area was designated as a radiation area with controlled access and the radiation was routinely surveyed according to the accelerator operating protocols since the section was directly exposed in the building. X-ray radiation with non-negligible level could occur if cavities are not under good vacuum conditions [40] likewise in post-maintenance period, or due to RF breakdown that appears in the cavities while in operation.

The MEBT RF system is comprised of four rebuncher cavities and four RF amplifiers driving the cavities individually. The X-ray radiation may occur in the fourth rebuncher cavity in the SNS MEBT that typically operates with the highest gap voltage and field [41][42]. The gap voltage V_o is an important parameter that determines the bunching efficiency of the velocity modulation device. To increase V_o for a given power, this cavity requires a reentrant geometry [43] which can reduce the particle transit time [44] along the cavity gap. The reentrant geometry, however, increases the peak electric field and may cause field emission with electron discharge. The narrow gap increases power efficiency, but raises peak electric field as well. This can lead

to a field breakdown and X-ray radiation unless the cavity maintains high vacuum with, minimized gas desorption from wall, and gas flow from the ion source.

Typically, however, in MEBT line design, a tight longitudinal size limitation is required which is 13 cm [6] for the SNS MEBT as shown in Figure 56. This constraint comes from the fact that the beam optics design recommends to keep this cavity length as short as possible to minimize beam size growth. At the same time, the cavity design should be kept simple with good power efficiency. Therefore, a more conservative cavity design is sought for minimizing X-ray radiation.

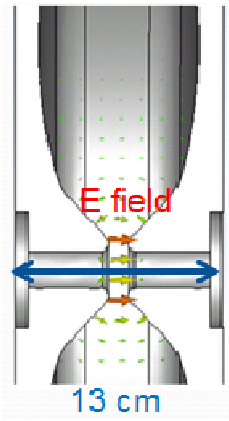

Figure 56. Cavity length limitation in MEBT line (13 cm).

4.2 MEBT Reference Design (Single Gap)

The requirements of a simple design with high power efficiency led to a single gap TM mode cavity design shown in Figure 57. For the SNS MEBT RF frequency of 402.5 MHz, the usual

TM mode cavity design gives good power efficiency and reasonable cavity size. The designed cavity length is 11.5 cm, which is within the 13 cm length constraints [6].

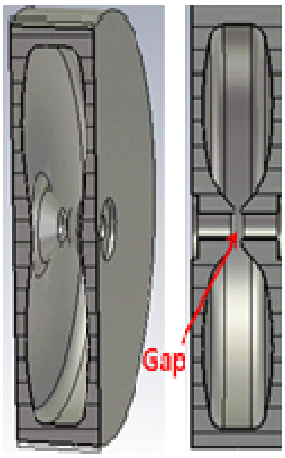

Figure 57. Single gap MEBT rebuncher design.

However, slight X-ray radiation was detected and it was measured as shown in Figure 58. Which is a problem that need to be addressed and finding a solution to it, that can be useful for future accelerator designs.

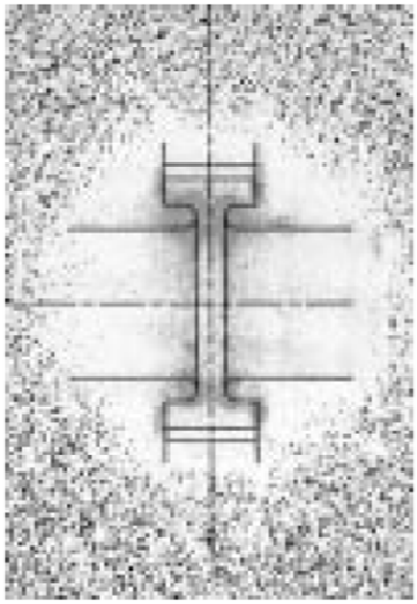

Figure 58. Radiation measurement of a single gap Klystron cavity - After [45].

Maintaining high RF efficiency with no degradation of beam performance while reducing the X-radiation is important

For the current SNS MEBT section, beam energy at a single gap elliptical buncher is 2.5 MeV with H- light ion. The maximum cavity length L and bore radius a are determined to be 13.00 cm and 1.5 cm respectively by beam line requirement and beam simulation [8] in cavity 1 and 4. Meanwhile, for cavity 2 and 3, a = 1.8 cm is used.

Within the constraints of L and a, the gap length g is selected to optimize particle transit efficiency. The transit time factor T represents the RF efficiency [7]. The designed T value in

SNS elliptical cavity is 0.445 for a =3.0 cm cavity with g = 1.23 cm [8]. Typically, peak electric field can be reduced by increasing g, however, T and RF efficiency will be reduced as well.

Subsequently, to realize a new MEBT section design beyond the level of the state of the art, the new design should provide similar T and RF efficiency while decreasing its peak electric field.

Other cavity parameters need to be evaluated as well and used for efficiency prediction, first the cavity shunt impedance R_s is calculated from the gap voltage V_0, which can be obtained from the integration of longitudinal on- axis gap field E(z). For convenience, the average integration value of $E(z)$ is expressed as E_0 as (3) [7]:

$$R_s = \frac{(V_0 \cdot T)^2}{P} = \frac{\left|\left(\int_0^L E(z) \cdot dz\right) \cdot (T)\right|^2}{P} = \frac{(E_0 \cdot T \cdot L)^2}{P} \qquad (3)$$

where P is the dissipated power on cavity wall.

The second parameter is R/Q [7] defined using Equation (4) below from the measurements of R/Q - Meanwhile, Measurement of Q as well can be used to calculate R_s as indicated by

$$\frac{R}{Q} = \frac{R_s}{Q} = \frac{(V_0 \cdot T)^2}{\omega U} = \frac{\left|\left(\int_0^L E(z) \cdot dz\right) \cdot (T)\right|^2}{\omega U} = \frac{(E_0 \cdot T \cdot L)^2}{\omega U} \qquad (4)$$

where U is the cavity stored energy, and ω is the angular RF frequency.

4.3 Complexity of X-Ray Radiation Issue

Field emission mechanism can facilitate X-radiation mechanism

The X-ray radiation mechanism is rather complex as indicated by [46-47]. A general radiation intensity J_X dependence on the gap RF voltage $V(t)$, and the discharge current $i(t)$ is given by:

$$J_X = K \cdot i(t) \cdot V^n(t) \qquad (1)$$

where K is a constant and can be determined experimentally. The constant n commonly has a value in the range of 1.8~3.0 [46-47]. Lowering $V(t)$ can directly decrease J_X with a quadratic to cubic dependence; which is significant.

The generation of $i(t)$ follows the field emission (FE) [17] mechanism because of the presence of high RF fields in the cavities. Assuming $i(t)$ generation due to FE mechanism, the

emission current can be determined by the cavity RF electric field likewise using Fowler-Nordheim formula [48] :

$$i(t) \cong A E^{2.5}(t) e^{-\frac{B}{E(t)}} \qquad (2)$$

where A and B are constants, and E is the applied RF electric field. Therefore, to decrease X-ray radiation, both $i(t)$ and the electric field E should be reduced. Accurate results can be obtained using (2).

However, in a real system, the field emission mechanism usually starts even faster because of the existence of surface micropoints. These micropoints may lead to X–ray radiation multiplication, i.e. enhancement. The enhancement of the field emission due to the micro-emitters (micropoints) on the material surface is more specifically from various surface imperfections such as tiny spikes, impurities, austerities, scratches etc. The field on these emitters can be higher by 40-100 times than the average field on the surface. However, this enhancement (beyond what is predicted by formula (2)) is always unknown, that is why this Fowler-Nordheim FE formula is so hard for use in practice. Nevertheless, the surface roughness should be controlled and minimized as much as possible to minimize this field enhancement mechanism, i.e. a very smooth surface will reduce the effects of micropoints. Figure 59 shows the field direction of single gap cavity and FE micropoints concept.

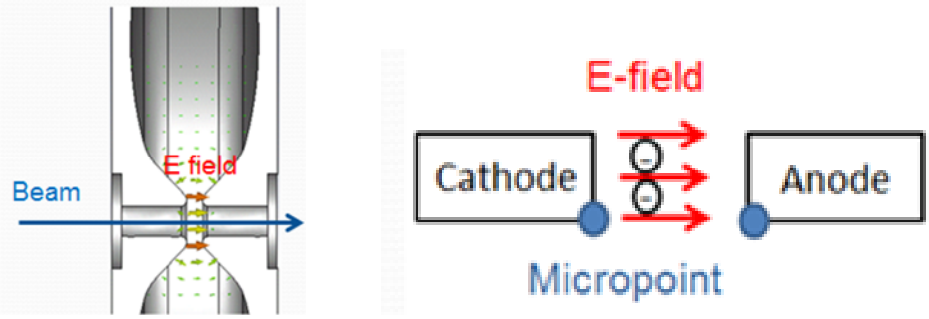

(a) (b)

Figure 59. Electric field at rebuncher cavity gap: (a) field direction, (b) field emission mechanism.

4.4 Proposed Double Gap Cavity Design:

4.4.1 Comparison of Design Parameter

Use TM double gap design to decrease gap voltage and field while supporting similar cavity Q factor

To resolve the X-ray radiation problem, we propose a double gap TM mode cavity design called "DTL type" as shown in Figure 60 (b). DTL stands for a cavity with multi-gap those are made by the connecting tubes on the beam axis called "drift tube" [7] interleaved with open gaps that can support an axial RF field. The drift tube is suspended by a stem that attaches to the

larger cylindrical body. Figure 60 shows a comparison of the existing and proposed designs. Figure 60 (b) shows a single drift tube cavity design. From the discussion in the previous section, we conclude that decreasing the gap voltage and peak electric field can be effective in decreasing the radiation intensity. The DTL type design divides a gap voltage that is half of the single gap design likewise a voltage divider circuit. Moreover, this design can avoid sharp cavity gap geometry and utilize smoother surfaces to improve the RF efficiency. Although slightly more RF losses occurs through drift tube, this power loss can be well compensated by slightly decreasing the gap size of the DTL cavity or extending the cavity length beyond 13 cm.

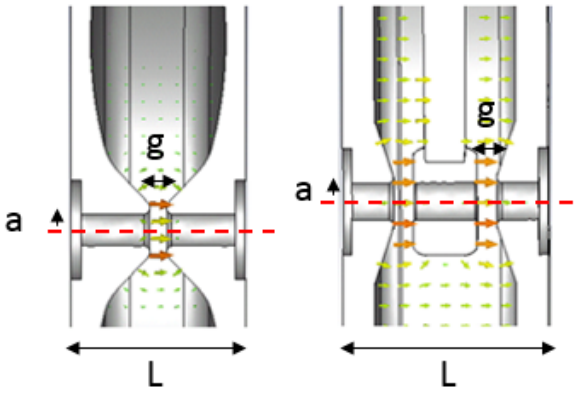

(a) (b)

Figure 60. Electric field in the paraxial direction: (a) single gap elliptical, (b) double gap DTL type cavity.

We analyzed our new design using CST, but for validating our models we used the elliptical cavity (2D) simulation data shown in Table 11 (the manufacturer's Superfish [17] tool results of the existing structure at SNS [41]) as a reference. Since Superfish is a 2D tool, the 3D CST tool

was used [20] first to validate our 3D model of the single gap design, and results turned out to be in good agreement with the 2D case as shown in Table I, which is a good indication of CST capabilities.

The proposed DTL type cavity designs parameters are summarized in Table 11 and compared to the results of the single gap elliptical cavity. Subsequently, the two proposed DTL type (A, B) designs were simulated with CST tool. The DTL type (A) has a similar gap size like the elliptical cavity, while the DTL type (B) has a slightly wider gap to further decrease the peak field.

As noticed in Table 11, the simulated peak electric field (E_{pk}) in DTL type (B) cavity is about 54 % lower than that of the elliptical cavity-- this is a great advantage for reducing X-ray radiation. As a result, the power efficiency of the DTL type cavity is expected to be slightly lower compared to that of the elliptical cavity.

Meanwhile, there is a slight increase in the power loss by surface current in the DTL type cavity due to the addition of the drift tube as shown in Figure 61. This additional power loss is responsible for its Q and R_s degradation. Additionally, the peak magnetic field (H_{pk}) increases by 30 ~ 40 % in the DTL type cavity because of its higher magnetic field intensity around the drift tube stem. As a consequence, more surface current is formed and an adequate cooling channel need to be used into the drift tube stem.

Table 11. Elliptical vs. DTL type - at 28.2 kW peak power.

	Elliptical (2D)	***Elliptical (3D)***	***DTL Type (A)***	***DTL Type (B)***
Frequency f_0 (MHz)	402.5	401.9	400.3	400.1
Cavity length L (cm)	11.48	11.48	13.00	13.00
Gap size g (cm)	1.230	1.230	1.224	1.423
			1.224	1.423
Q (unloaded, Copper)	21542	21413	20773	20903
R/Q				
R_s (Mohm)	29.44	29.35	29.17	27.83
V_0 (kV)	0.638	0.629	0.592	0.581
T	120.00	119.08	116.93	114.55
E_0 (MV/m)	0.445	0.447	0.459	0.452
E_{pk} (MV/m) [Kilpatrick]	2.35	2.32	1.94	1.93
H_{pk} (A/m)	30.8 [1.58]	29.9 [1.54]	16.75 [0.86]	13.26 [0.68]
	6516	6565	9323	8644

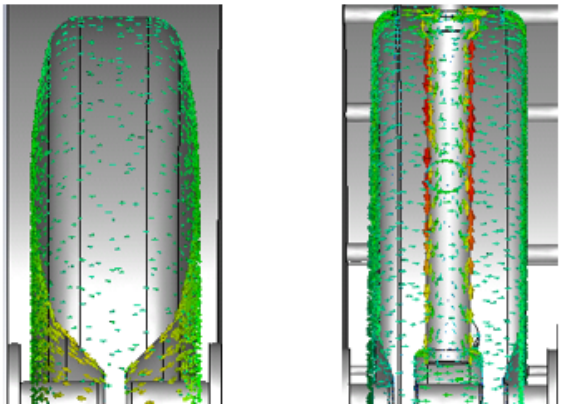

(a) (b)

Figure 61. Surface current distribution: (a) single gap elliptical, (b) double gap DTL type cavity.

4.4.2 Finalized Design Parameter

The detailed mechanical design of the DTL type cavity is shown in Figure 63 with Solidworks [37]. To validate the DTL type cavity design and simulation, a scaled-down model based on the DTL type design was utilized. The scaled model that can operate at 800 MHz are listed in Figure 62. This scaled prototype can be built inexpensively but useful for studying of RF properties accurately. Figure 62 shows some important cavity internal dimensions and perspective view.

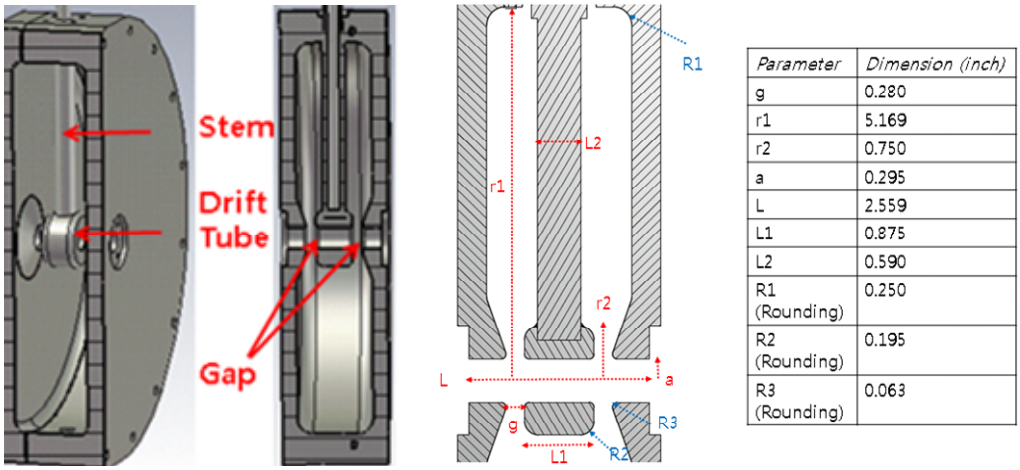

Parameter	*Dimension (inch)*
g	0.280
r1	5.169
r2	0.750
a	0.295
L	2.559
L1	0.875
L2	0.590
R1 (Rounding)	0.250
R2 (Rounding)	0.195
R3 (Rounding)	0.063

Figure 62. Mechanical design of the double gap cavity.

The exploded view representing cavity assembly process is shown in Figure 63. Two cavity pieces are connected together with bolts and nuts with washers. Drift tube assembly and tuner part are to be connected to the major cavity piece.

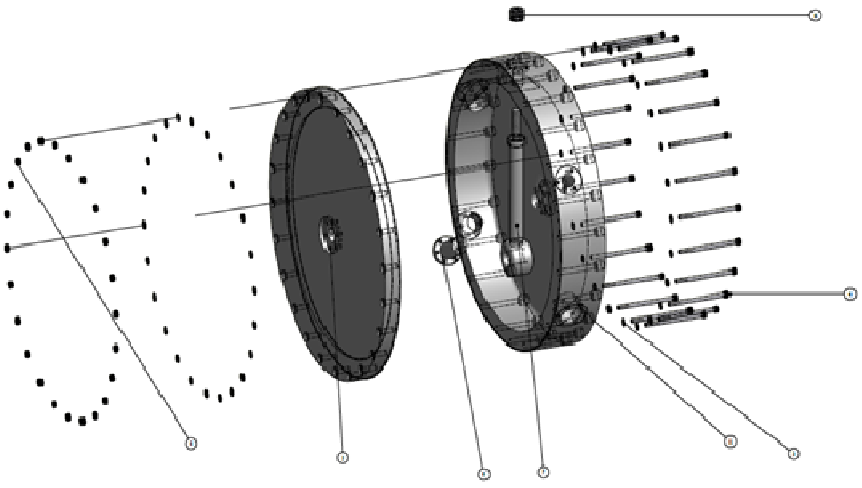

Figure 63. Mechanical design of the double gap cavity: exploded view.

Aluminum material is relatively inexpensive, and has been used in the DTL type cavity prototype design. Meanwhile, two RF couplers are attached for RF measurement.

The Q and R_s are typically different in the scaled cavity relative to the full size one. However, the R/Q is frequency independent and should be the same for both full and scaled cavities. Therefore, R_s can also be found from R/Q and Q measured results of the scaled cavity. Figure 64 shows the fabricated 800 MHz ½ - scaled DTL type cavity components and assembly. AL 6061 T6 material with 42% of copper conductivity is used to reduce manufacturing cost while having good electrical conductivity. A drift tube with a stem is attached to the cavity shell as shown in Figure 64, and assembled to another piece. The transmission method of S_{21} measurement is utilized for the frequency and Q measurements in this paper with two wire-loop antennas for coupling power in and out of the system. The isolation between these two magnetic loop couplers is about 60dB in the TM_{010} mode. The simulated tuning sensitivity of the 400MHz DTL type cavity is 95 kHz/cm with a 32 mm diameter circular slug tuner. For the same size tuner, the tuning sensitivity of the 400 MHz elliptical cavity is 120 kHz/cm, hence the DTL type cavity needs slightly larger tuner diameter of about 36mm to achieve similar sensitivity.

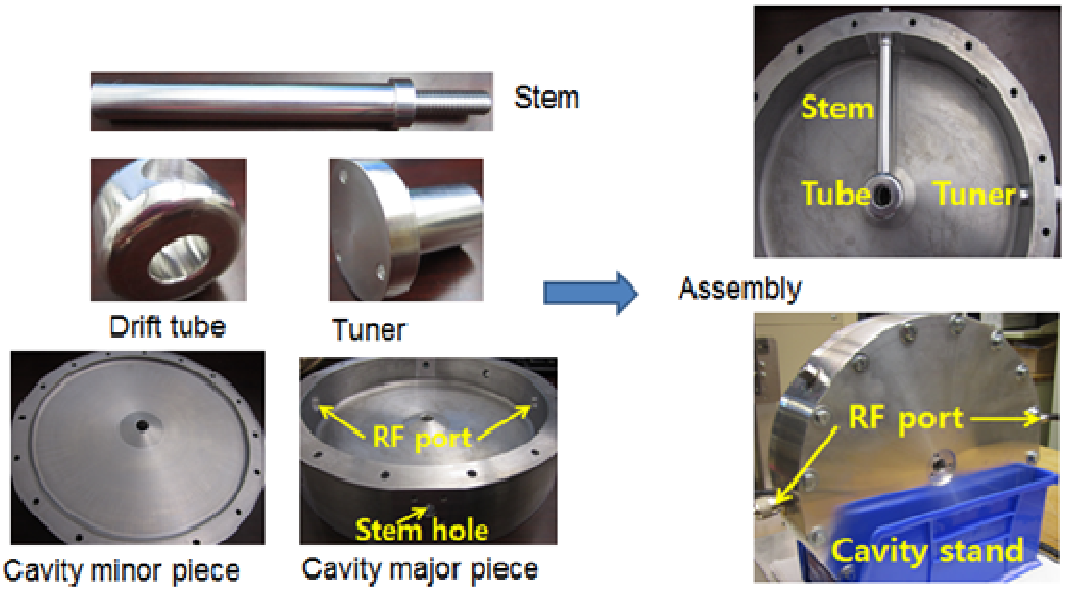

Figure 64. Fabricated double gap rebuncher cavity and assembly.

4.5 Validation of Solutions and Experimental Results:

To validate the DTL type cavity simulation, a scaled-down model based on the DTL type (B) design was utilized. The scaled model operates at 800 MHz. The model dimensions are listed in Figure 62. In this scaled prototype, the designed cavity length *L* is 6.5 cm to meet the system dimensional requirements; but it is a 13% longer than the scaled elliptical cavity parameter *L* of 5.74 cm.

4.5.1 Simulation vs. Measurement

Table 12 and Table 13 show the simulated f_s and measured f_M results of the DTL type cavity operating mode frequency and its Q. Conductivity of aluminum is utilized in our simulation. Only the TM_{010} operating mode and its next adjacent modes are listed.

The measured resonance frequencies of the modes are in excellent agreement with the simulated ones of all modes of interest with a discrepancy of < 0.05 %. Meanwhile, the disagreement rises up to around 6~19 % in the Q measurements due to an extra power loss that appears on the cavity seam plane, stem, surface roughness, and coupler ports. The measured 12% difference in the TM_{010} mode Q is quite acceptable compared to other cavity design experiments [41-42] which usually demonstrate about 20 % disagreement.

Table 12. Simulation vs. measurement - frequency

Mode	***f_s [MHz]***	***f_M [MHz]***	***f_M [Error %]***
TM_{010}	800.49	800.56	0.01
TM_{110}	1427.19	1427.04	0.01
TM_{110}	1439.61	1439.19	0.03

Table 13. Simulation vs. measurement - *Q* (unloaded)

Mode	Q_s *[MHz]*	Q_M *[MHz]*	Q_M *[Error %]*
TM_{010}	9286	8179	12
TM_{110}	9474	7667	19
TM_{110}	10567	9974	06

Figure 65 describes a configuration of the bead pull measurement system setup. A 3mm diameter spherical metal bead on a fishing line is advanced by a motor-driven pully. A computer based motor control system is used to vary the speed and direction of the motor movement, while S_{21} is measured with a vector network analyzer (VNA).

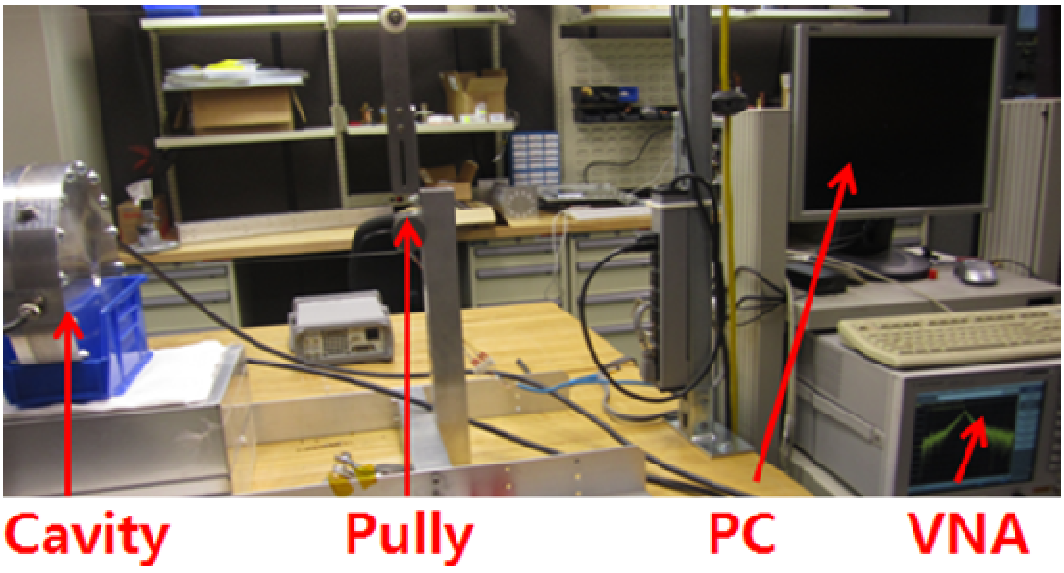

Figure 65. Bead-pull measurement setup.

The result of the bead-pull phase shift measurements is shown in Figure 66.

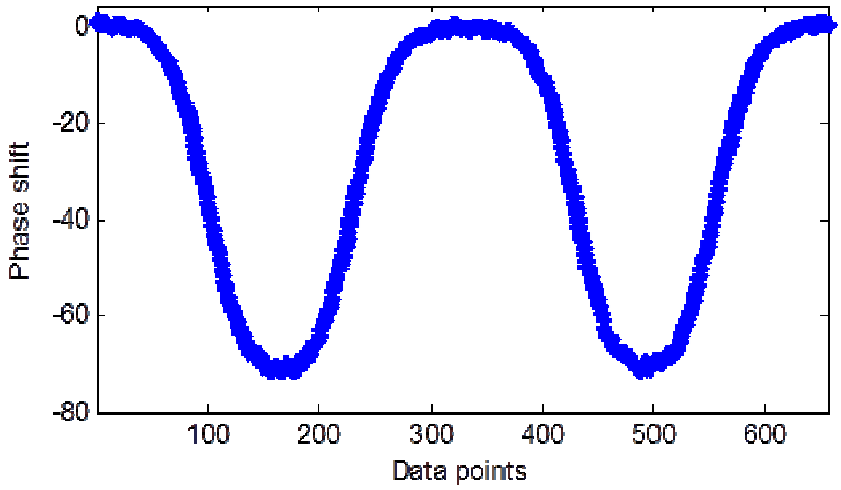

Figure 66. Measured phase shift of S_{21} by bead perturbation.

Two phase shifting cycles are observed because of the double gap. This result is integrated along the axis by using (3)-(4) to calculate *R/Q*.

Table 14 summarizes the calculated *R/Q* and R_s based on the previous measurements. There was about 6.1% differences in *R/Q* results between simulation and measurements; which was slightly higher than the expected results of 4~5% of Ref. [25], however fairly close. Considering a 12% difference in the *Q* measurement from Table III, the R_s result shows approximately 17.4% discrepancy.

Table 14. Simulation vs. measurement - cavity parameters (Parameters assumed at 28.2 kW peak power).

	Simulation	*Measurement*	*Error*
R/Q	27.83	26.12	6.1 %
R_s (MOhm)	0.258	0.213	17.4 %

Measured results reported in the previous section validated the accuracy of our 3D simulation of the DTL type cavities at 800 MHz. Therefore, this experiment can be extended to develop DTL type cavity at 400 MHz.

4.5.2 Parametric Study

Figure 67 shows a comparison of the cavity parameters as a function of the gap size from 0.80 cm to 2.05 cm (for each DTL type cavity gap). Peak field comparison is also shown in Figure 68. Parameters are normalized to the values of the elliptical cavity.

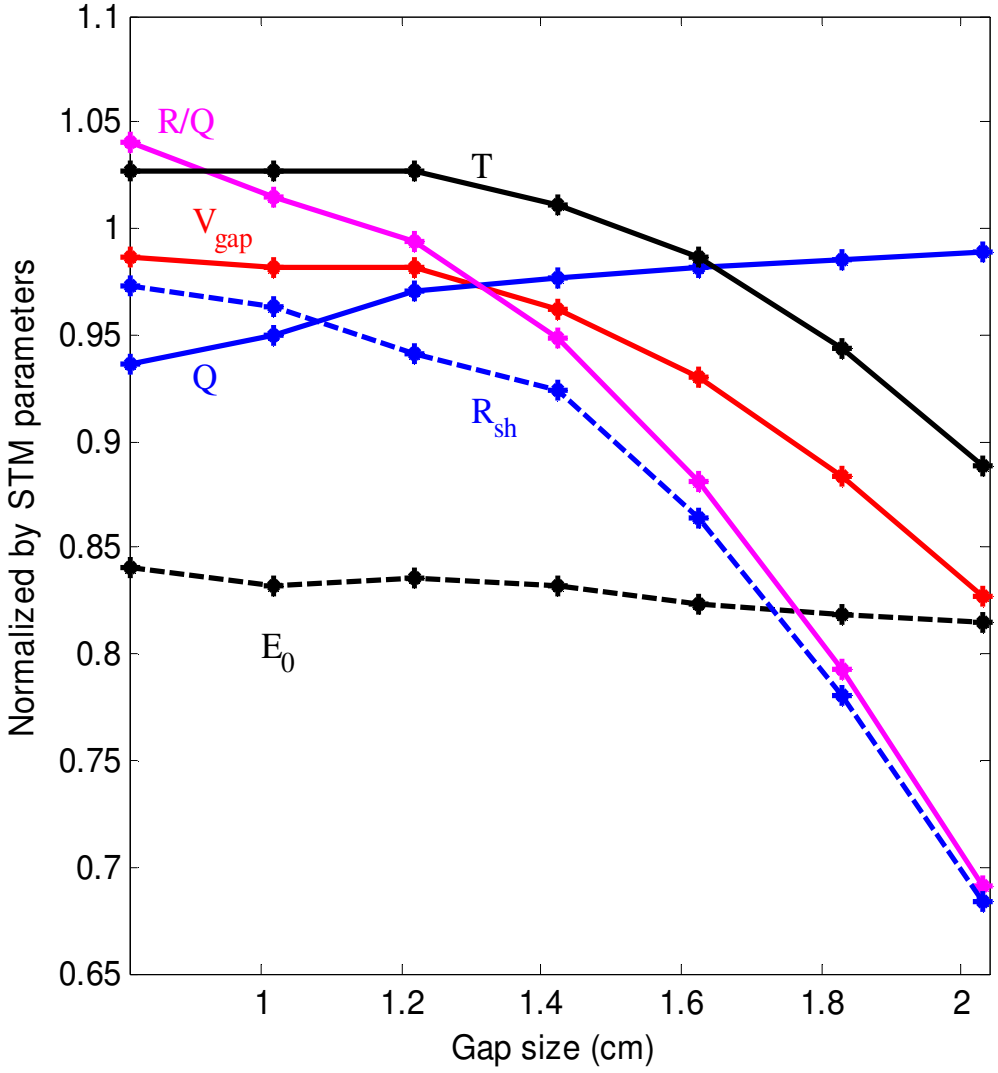

Figure 67. Simulated E_o, R/Q, T, V_{gap}, R_{sh}, and Q vs. gap size.

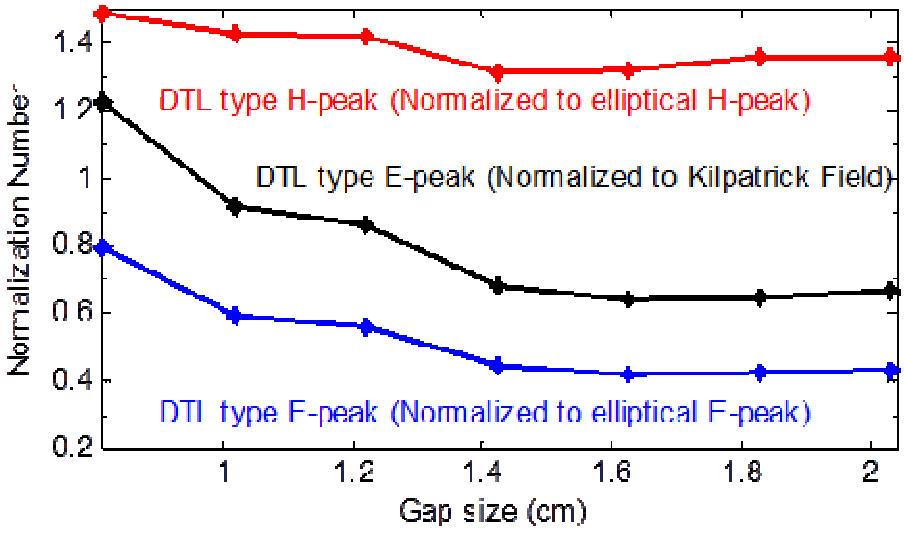

Figure 68. Simulated on-axis *E* field vs. gap dimension.

For greater than 1.2 cm gap, both *R/Q* and R_s decrease rapidly, although *Q* increases. Meanwhile, the peak EM field rapidly increases for < 1.4 cm gap. Therefore, from Figure 67 and Figure 68, an optimum gap size can be selected around 1.2 ~ 1.4 cm. Definitely, the effect of gap size needs to be considered to achieve higher efficiency or lower peak field goals as well.

4.6 Thermal Analysis and Estimation of X-Radiation

4.6.1 Thermal Analysis

The high surface current around drift tube stem can be a concern of DTL type cavity design. The estimated total power dissipation is 1.72 kW in cavity 4 of SNS MEBT system. Here, thermal analysis with CST Multiphysics [20] is presented and discussed. The temperature

gradient in the cooling channel is not considered in this simulation. Therefore, the simulated result of the temperature gradient in cavity wall can be expected slightly less than simulations with full physical consideration. For example, the simulated gradient of elliptical cavity with Copper plated Steel structure is 7.5 K as shown in Figure 69, which is less than 1.7 K from the manufacturer's simulation data of 9.2 K [49].

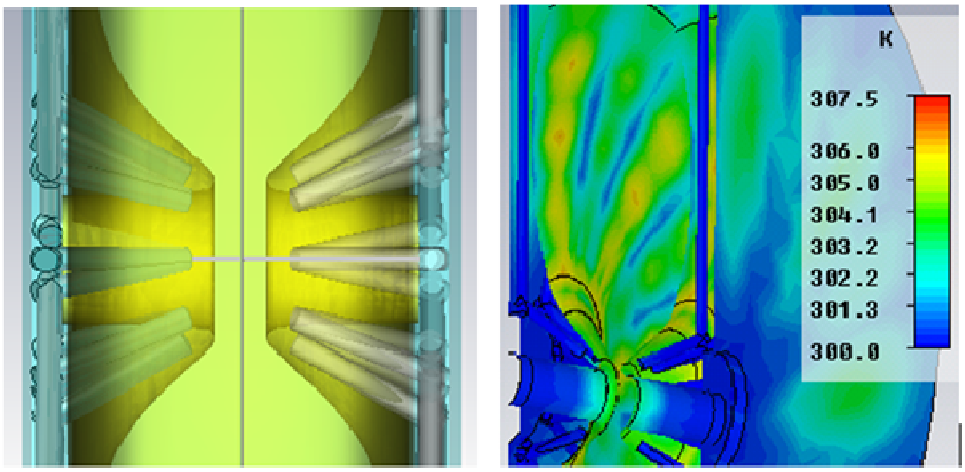

Figure 69. Thermal simulation result of elliptical cavity.

The DTL type cavity inner wall can be made of Copper to provide good electrical and thermal conductivity. Ref. [50] suggests utilization of Stainless Steel at the cavity outer wall to withstand the vacuum pressure. In our simulation, 15.5 mm of internal Copper cavity wall and 12.7 mm of outer Steel wall are used for the 400 MHz DTL type cavity. Meanwhile, the drift tube and stem assembly should be made using Copper, because of the intense heat dissipation around it [51].

Cooling channels are imported at the cavity wall and drift tube assembly as shown in Figure 70. The channel diameter in tube assembly is assumed to be 6.3 mm that leads to a heat transfer coefficient of 6585 W/(m^2·K).

The simulation results are shown in Figure 70 with cooling water and ambient temperatures set to 300 K. The simulated temperature gradient is 4.8 K. Considering similar water temperature gradient as seen in Figure 69 simulation, the maximum gradient with full physical consideration can be expected as 6.5 K.

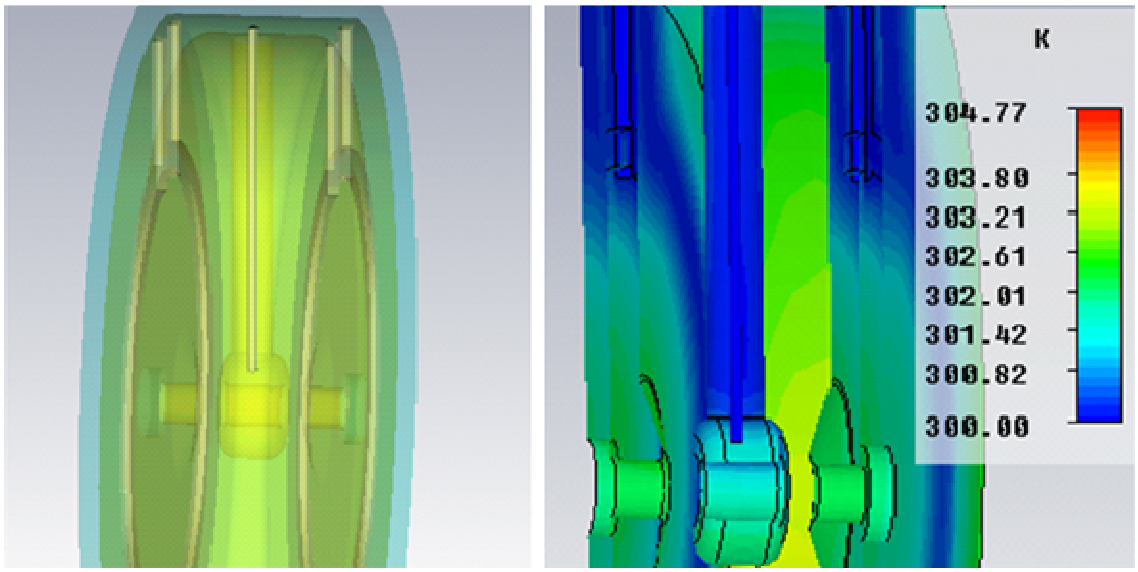

Figure 70. Thermal simulation result of DTL type cavity.

4.6.2 X-radiation Estimation

Double gap design can decrease the gap voltage, field, and X-radiation

Although direct X-ray radiation measurement with high power is not possible with aluminum test cavity, a relative comparison of radiation intensity in the elliptical and the DTL type cavities is possible with Eqs. (1)-(2) assuming the same surface and vacuum conditions. Since the X-ray radiation occurs in a pre-breakdown stage in general [45], equation (1) is expected to be slightly non-linear. But the K and n values in equation (1) are assumed to be constant in all calculations.

Two scenarios can exist as shown in Figure 71.

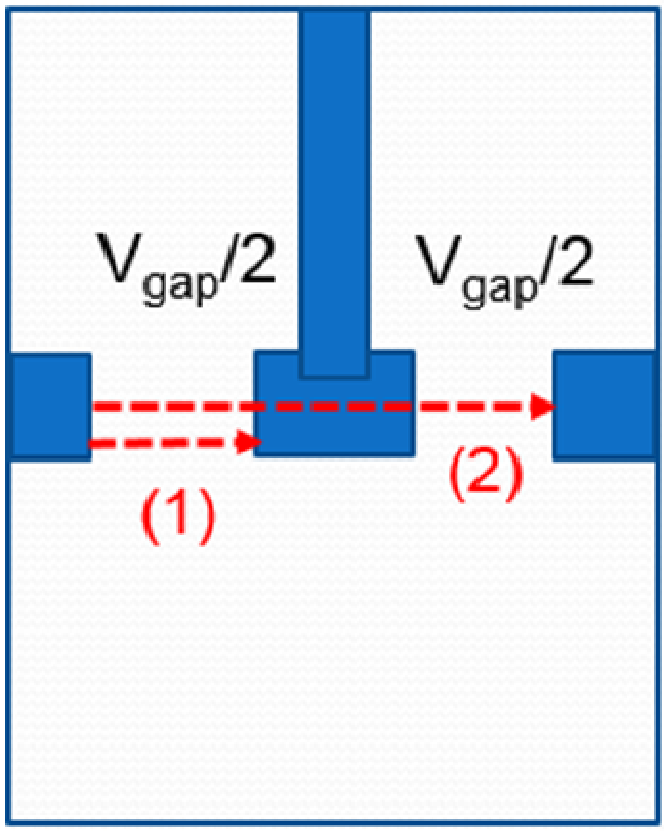

Figure 71. Electron emission and hitting scenario: (1) electrons hitting cavity half gap with Voltage = Vgap/2, (2) electrons hitting cavity end to end with Voltage = Vgap.

The ratio of radiation intensity J_X in DTL type cavity to that of the elliptical cavity is presented in Figure 72 and Figure 73 assuming n = 2 in equation (1). The results shown by the black line assumes the same 28.2 kW peak operating power in all cavities. Meanwhile, the ones shown by the blue line presume all cavities generate the same 120 kV net gap voltage with different power levels. Since the gap voltage is the key parameter of the rebuncher cavity, the blue line result represents a practical J_X for comparison.

From these calculations, the estimated J_X in DTL type cavity can decrease considerably to only 24 % of the elliptical cavity value with a 1.2cm gap size (for both). Even lower J_X can be achieved with a 1.4 ~ 1.6 cm gap size. J_X rather increases with a larger gap > 1.6cm because of the drastic decrement of RF efficiency. Regarding both RF efficiency and J_X, the 1.2 ~ 1.4 cm gap size can be considered as the optimum.

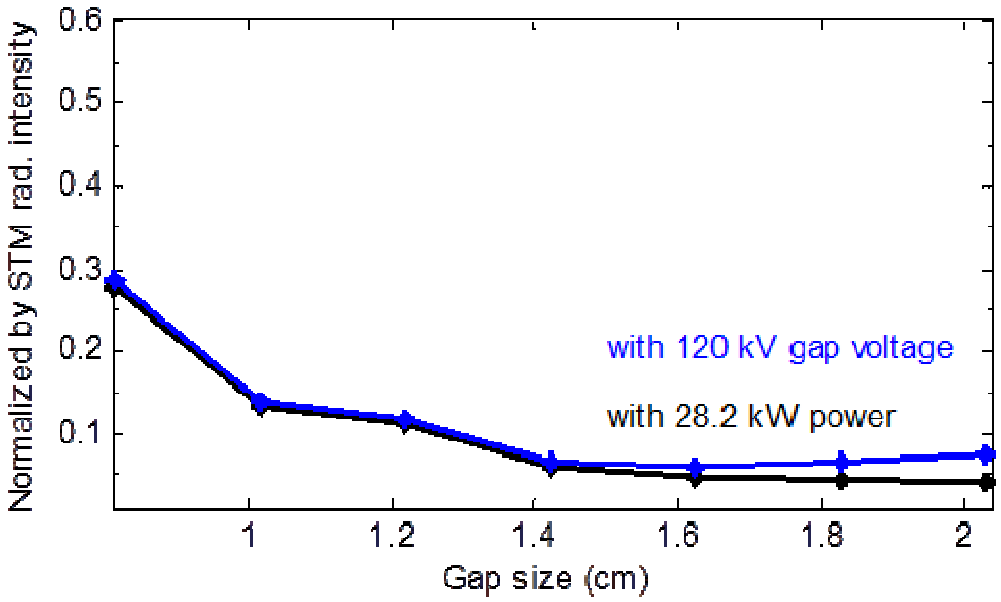

Figure 72. Estimated normalized radiation intensity as function of gap size - assuming n = 2 in Eq. (1), Scenario (1) in Figure 71.

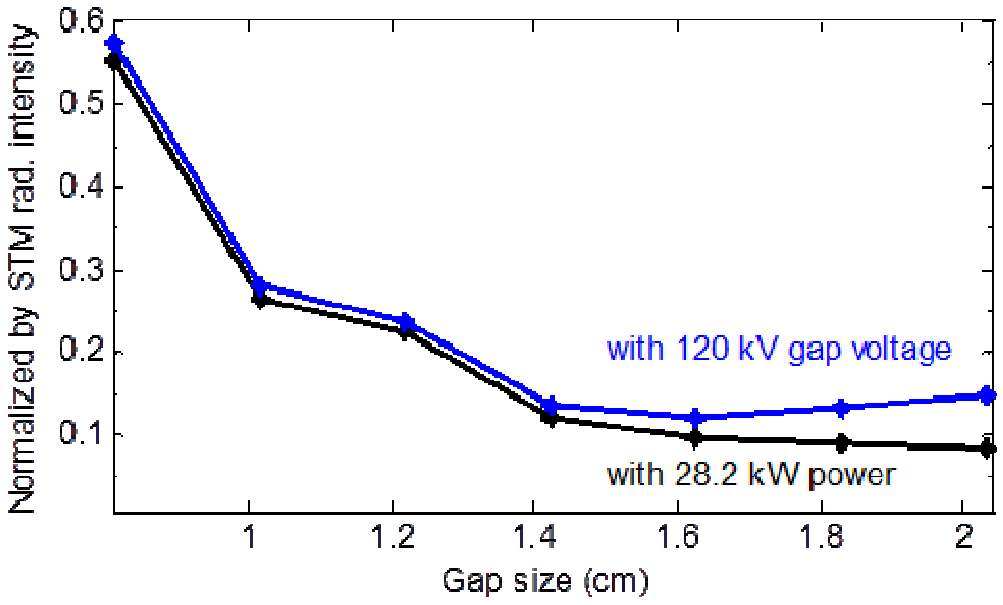

Figure 73. Estimated normalized radiation intensity as function of gap size - assuming n = 2 in Eq. (1), Scenario (2) in Figure 72.

4.7 Conclusions

The proposed double gap rebuncher cavity for SNS MEBT section as an example case has been studied with various 3D simulations and measurements. The proposed design gives similar cavity power efficiency while decreasing the gap voltage and field. A ½ scaled Aluminum demonstration model was built and tested. S-parameter and bead-pull measurement show excellent agreement with simulations. Based on the design parameters, thermal simulation and X-radiation calculations were performed as well. The simulation shows that this design can be

thermally stable with three cooling channels and usage of copper drift tube. The estimated X-radiation is less than a quarter of previous single-gap design.

The proposed double gap design has a great potential to relieve safety issues that SNS has been suffered for several years and potentially for any future accelerator facilities. Controlled access to the accelerator area by X-radiation causes huge waste of time and labor cost. Due to the complexity of the accelerator system, it is difficult to accurately measure the savings in time and labor costs resulted from using this double gap design. However, there is no doubt that its positive impact in time and labor costs is unquestionably significant.

CHAPTER V

CONCLUSION AND FUTURE WORK

5.1 Summary of Dissertation

Table 15 summarizes the technical challenges, our proposed solutions, and efforts to address these challenges.

There are three major technical challenges in addressing the RFQ problem. These challenges made it difficult for scientists to find ways to decrease RFQ design cost and potential fabrication errors. The first challenge is that it is not feasible to be directly measure the RFQ on-axis field which may be investigated using our perturbation study with extensive 3D EM simulation. The simulation accuracy was well verified with the measured results of the unperturbed RFQ first, then it was extended to investigating RFQ on-axis field in this credible perturbation study [27]. The second technical challenge is that the RFQ bandwidth is too narrow; which has been remedied by using alternative cut-back RFQ structures. We also carried out an in-depth analysis of such structures. These simulations were found to be in excellent agreement with the measurements [52]. The third challenge in addressing the RFQ problem is that RFQ energy velocity is too low and this has been resolved by our proposed new coupling cell design that brings more simplicity in coupled RFQ designs. The measurement results using a demonstration model were in good agreement with the simulation results.

In MEBT, the generation of X-ray radiation has been a main technical challenge. Our approach to build a double gap cavity structure addressed this X-ray radiation problem and the proposed solutions could drastically reduce the level of radiation. All EM simulations have been validated with measurements of a prototype Aluminum model [53].

Table 15. Summary of the Proposed Solutions.

Topic	***Technical Challenge***	***Proposed Solution***	***Validation Method***
RFQ	On-axis field cannot be measured	3D EM perturbation Study	Simulation Measurement
	Bandwidth is narrow	Alternative cut-back RFQ	Simulation Measurement
	Energy velocity is low	New coupling cell design	Simulation Measurement
MEBT	X – ray radiation is generated	Double gap cavity design	Simulation Measurement

5.2 Outcome and Impact of the Proposed Solutions

The outcome and impact of our proposed solutions are summarized in Table 16. Compared to the previous solutions, our proposed solutions have several advantages and represent the main research contributions of this dissertation.

Table 16. Outcome and Impact of the Proposed Solutions.

Topic	*Previous Solution*	*Proposed Solution*	*Outcome and Impact*
RFQ	Measured Cavity wall field	3D EM perturbation Study	1. On-axis field can be accurately estimated 2. Tolerance assessment 3. Accuracy validation
	Stabilizer Circuit is used	Alternative cut-back RFQ	1. Decrease RFQ design cost 2. Design guideline by length 3. Mode analysis and study
	Coupling cell design	New coupling cell design	1. Reduce coupling cell cost 2. New idea verification 3. Spurious mode suppression
MEBT	Single gap design	Double gap cavity design	1. Decrease gap voltage 2. Develop design guidelines 3. New idea verification 4. Decrease X-ray radiation 5. Develop thermal design

5.2.1 RFQ – Perturbation Study

- The details of the RFQ on-axis field can be estimated by the proposed 3D EM perturbation study with great accuracy.
- The RFQ fabrication tolerance can be determined using a perturbation study, which can prevent RFQ fabrication errors. RFQ fabrication mistakes could waste up to 2 million dollars of research funding.
- Simulation of the full sized RFQ models has been validated showing high level of accuracy. This observation simplifies the RFQ fabrication process without building an

Aluminum demonstration model. As a result, the overall project time and labor expenses can be reduced by more than 10%.

5.2.2 RFQ – Alternative RFQ cut-back designs

- The proposed alternative cut-back RFQ can decrease the high cost of mode stabilizer designs in RFQ fabrication. Both design time and tuning costs can be reduced as well.
- Our work established a design guideline for the RFQ by structure length. An optimum RFQ cut-back design can be selected from this design guideline, which is simplified in Table 17.
- The analysis work performed in this dissertation answers why alternative RFQ cut-back structures generate unique mode spectrum in detail. Moreover, the spectrum relation between non-degenerating DD dipole modes are clarified through our analysis.

Table 17. RFQ Design Options by RFQ Length (O – Good mode separation, X – Poor mode separation, i.e. requires mode stabilizer).

	4C	***DD***	***FD***
RFQ Rebuncher	X	O	O
RFQ (L<1λ)	X	O	O
RFQ (L=2λ)	O	X	O
RFQ (L=3λ)	X	O	X
RFQ (L=4λ)	O	X	O
RFQ (L=5λ)	X	O	X

5.2.3 RFQ – Coupling cell designs

- The proposed coupling cell design reduces the required tuning effort of the coupling cell in half. Therefore, the coupling RFQ design is considered more frequently in high energy RFQ applications over 5 MeV.
- The new coupling RFQ design idea has been verified with the measurements derived from a real RFQ demonstration model.
- The coupling gap spurious mode is suppressed in the new coupling cell design. Therefore, more flexibility is given when choosing coupling gap size.

5.2.4 MEBT – Double gap designs

- The proposed double gap design decreases the gap voltage by 50 %, therefore less than 25 % of X-ray radiation is expected.
- A design guideline for the proposed double gap design has been developed. Cavity parameters are estimated with respect to the gap size.
- A ½ scaled prototype model has been measured, and the results are in excellent agreement with simulation results.
- A thermal design has also been pursued, and it has been proven that the double gap design does not cause any thermal issues.

5.3 Implementations and pursue of the proposed solutions

Table 18 presents the detailed implementation plan for the proposed solutions. The 3D EM perturbation study has already been performed in the SNS RFQ analysis and in the spare part design. Implementation of a double gap design has been positively considered since it can be a direct solution to the current X-radiation issues. Politically, development of the high power alternative cut-back RFQ and coupled RFQ design may require further approval until it reaches the final stage of implementation. Given the high cost of RFQ fabrication, implementation of the new RFQ structures including finalizing all design verifications will take more time.

Table 18. Implementation Plan for the Proposed Solutions.

Topic	***Proposed Solution***	***Implementation Plan / Status***	***Decision***
RFQ	3D EM perturbation Study	Immediately	Designer
	Alternative cut-back RFQ	In the future	ORNL Laboratory / DOE
	New coupling cell design	In the future	ORNL Laboratory / DOE
MEBT	Double gap cavity design	Under consideration	ORNL Laboratory

5.4 Future work

The research presented in this dissertation provides basis for future research in several areas. These areas include: successfully implementing and operating the proposed RFQ with high power, performing a direct measurement of X-ray radiation from double gap rebuncher cavity, and making some design modifications to realize the proposed cavities in high power operation.

5.5 Publications

5.5.1 Transactions

[1] Ki R. Shin, Yoon W. Kang, and Aly E. Fathy, "Feasibility of folded and double dipole radio frequency quadrupole (RFQ) cavities for particle accelerators," IEEE Transactions on Nuclear Science, Vol. 61, Issue 2, Apr. 2014.

[2] Ki R. Shin, Yoon W. Kang, and Aly E. Fathy, "Design guideline of a double-gap microwave rebuncher cavity for a 400 MHz, 2.5 MeV energy light ion accelerator with lower gap voltage and field," IEEE Transactions on Nuclear Science, Vol. 61, Issue 2, Apr. 2014.

[3] Ki R. Shin, Yoon W. Kang, Sang-Ho Kim, and Aly E. Fathy, "Investigation of electromagnetic field perturbation with respect to mechanical imperfections in radio frequency quadrupole (RFQ) structure," IEEE Transactions on Nuclear Science, Vol. 59, Issue 5, Oct. 2012.

5.5.2 Conferences

[1] Ki R. Shin, Yoon W. Kang, Aly E. Fathy, and Mark S. Champion, "Design and measurement of double gap buncher cavity proposed for reduction of X-ray radiation," Proceedings of 2013 Particle Accelerator Conference, Pasadena, CA.

[2] Ki R. Shin, Yoon W. Kang, Aly E. Fathy, and Mark S. Champion, “Radio frequency quadrupole cavity structure for particle accelerators – simulation and measurements,” Proceedings of 2013 International Microwave Symposium, Seattle, WA.

[3] Ki R. Shin, Yoon W. Kang, and Aly E. Fathy, “Field study of radio frequency quadrupole cavity end-region,” Proceedings of 2013 National Radio Science Meeting, Boulder, CO.

[4] Ki R. Shin, Yoon W. Kang, and Aly E. Fathy, “Broadband antenna matching network design and application for RF plasma ion source,” Proceedings of 2011 Particle Accelerator Conference, New York, NY.

REFERENCES

[1] T. Wangler, J. Billen, and R. Keller, "The SNS," *U. S. Particle Accelerator School,* 2004 2004.
[2] P. M. Lapostolle and A. L. Septier, "LINEAR ACCELERATORS," 1970.
[3] S.-H. Kim, A. Aleksandrov, M. Crofford, J. Galambos, P. Gibson, T. Hardek*, et al.*, "Stabilized operation of the Spallation Neutron Source radio-frequency quadrupole," *Physical Review Special Topics-Accelerators and Beams,* vol. 13, p. 070101, 2010.
[4] I. Kapchinsky and V. Tepliakov, "Linear ion accelerator with spatially homogenous focusing," *Prib. Tekh. Éksp,* vol. 2, p. 119, 1970.
[5] LBNL, "The RFQ design review," 1999.
[6] J. Staples, D. Oshatz, and T. Saleh, "Design of the SNS MEBT," *LINAC '2000, Monterey, MOD18,* 2000.
[7] T. P. Wangler, *RF Linear accelerators*: John Wiley & Sons, 2008.
[8] A. Ratti, J. Staples, D. Oshatz, J. Potter, and G. Li, "MEBT rebuncher FDR," *SNS technical note FE-ME-035,* 2000.
[9] J. Staples, "Fundamentals of Proton Linear Accelerators with Simulations Lab," *U. S. Particle Accelerator School,* 2011.
[10] E. Fagotti, L. Antoniazzi, A. Palmieri, F. Grespan, and M. Desmons, "High power RF conditioning of the TRASCO RFQ," *THPB040, these proceedings,* 2012.
[11] A. Ueno and Y. Yamazaki, "New field stabilization method of a four-vane type RFQ," *Nuclear Instruments and Methods in Physics Research Section A: Accelerators, Spectrometers, Detectors and Associated Equipment,* vol. 300, pp. 15-24, 1991.
[12] L. M. Young and L. Rybarcyk, "Tuning the LEDA RFQ 6.7 Mev accelerator," in *this conf*, 1998.
[13] M. J. Browman and L. M. Young, "Coupled radio-frequency quadrupoles as compensated structures," in *Proc. of the 1990 Linear Accelerator Conference,(Albuquerque, 10-14 Sept. 1990) LA-12004-C*, 1990.
[14] L. M. Young, "Segmented resonantly coupled radio-frequency quadrupole (RFQ)," in *Particle Accelerator Conference, 1993., Proceedings of the 1993*, 1993, pp. 3136-3138.
[15] L. Young, "An 8-meter-long coupled cavity RFQ Linac," in *Presented at the 17th International LINAC Conference, Tsukuba, Japan, 21-26 Aug. 1994*, 1994, pp. 21-26.
[16] L. Young, "25 years of technical advances in RFQ accelerators," in *Particle Accelerator Conference, 2003. PAC 2003. Proceedings of the*, 2003, pp. 60-64.
[17] K. Halbach and R. Holsinger, "SUPERFISH-a computer program for evaluation of RF cavities with cylindrical symmetry," 1976.
[18] R. Klatt, F. Krawczyk, W. Novender, C. Palm, T. Weiland, B. Steffen*, et al.*, "MAFIA-A three-dimensional electromagnetic CAD system for magnets, RF structures, and transient wake-field calculations," in *Proceedings of the 1986 Linear Accelerator Conferences*, 1986.
[19] D. Li, J. W. Staples, and S. P. Virostek, "Detailed modeling of the SNS RFQ structure with CST microwave studio," in *Proceedings of LINAC*, 2006, pp. 580-582.
[20] C. M. Studio, "Computer Simulation Technology," *GmbH, Darmstadt, Germany,* 2009.
[21] H. ANSYS, "Ansoft Corp., Pittsburgh, PA," ed.
[22] A. Comsol, "COMSOL multiphysics user's guide," *Version: September,* 2005.

[23] G. Romanov and A. Lunin, "Complete RF Design of the HINS RFQ with CST MWS and HFSS," *LINAC08, Victoria, BC, Canada,* 2008.
[24] S. Jolly, M. Easton, J. Pozimski, and A. Letchford, "Integrated design method and beam dynamics simulations for the FETS radio frequency quadrupole," *IPAC2010, Kyoto, May,* 2010.
[25] L. C. Maier Jr and J. Slater, "Field strength measurements in resonant cavities," *Journal of Applied Physics,* vol. 23, pp. 68-77, 1952.
[26] P. Balleyguier and F. Simoens, "Simulations vs. measurements on IPHI RFQ cold model," in *8th European Particle Accelerator Conference, Paris*, 2002, p. 40.
[27] K. R. Shin, Y. W. Kang, S.-H. Kim, and A. E. Fathy, "Investigation of Electromagnetic Field Perturbation With Respect to Mechanical Imperfections in Radio-Frequency Quadrupole (RFQ) Structure," *Nuclear Science, IEEE Transactions on,* vol. 59, pp. 2428-2434, 2012.
[28] M. U. s. Guide, "The mathworks," *Inc., Natick, MA,* vol. 5, 1998.
[29] F. Grespan, A. Pisent, and A. Palmieri, "Dipole stabilizers for a four-vane high current RFQ: Theoretical analysis and experimental results on a real-scale model," *Nuclear Instruments and Methods in Physics Research Section A: Accelerators, Spectrometers, Detectors and Associated Equipment,* vol. 582, pp. 303-317, 2007.
[30] L. Young, "Tuning and Stabilization of RFQ's," in *Proceedings of the 1990 Linear Accelerator Conference*, 1990, pp. 10-14.
[31] R. Hutcheon, L. Hansborough, K. Hohban, and S. O. Schriber, "RFQ linac structure developments at CRNL," *Nuclear Science, IEEE Transactions on,* vol. 30, pp. 3521-3523, 1983.
[32] R. Hutcheon, J. Brown, L. Hansborough, S. Schriber, and R. Turner, "100% duty factor RFQ linac systems at CRNL," *Nuclear Science, IEEE Transactions on,* vol. 30, pp. 3557-3559, 1983.
[33] M. Chen, G. Tsandoulas, and F. Willwerth, "Modal characteristics of quadruple-ridged circular and square waveguides (short papers)," *Microwave Theory and Techniques, IEEE Transactions on,* vol. 22, pp. 801-804, 1974.
[34] A. France, M. Desmons, O. Piquet, and C. Rossi, "RF design and tuning of LINAC4 RFQ," 2012.
[35] D. Li, "The front-end system study of project X," *LBNL Presentation,* 2010.
[36] R. E. Collin, *Foundations for microwave engineering*: John Wiley & Sons, 2007.
[37] I. SolidWorks, "Solidworks corporation," *Concord, MA,* 2002.
[38] L. U. Manual, "National Instruments," *Austin, TX,* 1998.
[39] J. C. Slater, "Microwave electronics," 1950.
[40] A. Aleksandrov, "SNS MEBT: Beam dynamics, diagnostics, and performance," *Private Presentation*.
[41] L. Doolittle, "Rebuncher Cavity Design Update," *FEEE-014, SNS Technical Note,* 2000.
[42] J. Staples, "MEBT buncher cavity design," *SNS technical note FE-PH-024,* 1999.
[43] K. Fujisawa, "General treatment of klystron resonant cavities," *Microwave Theory and Techniques, IRE Transactions on,* vol. 6, pp. 344-358, 1958.
[44] E. L. Ginzton, *Microwave measurements*: McGraw-Hill, 1957.

[45] J. Wang and G. Loew, "Field emission and rf breakdown in high-gradient room-temperature linac structures," *Proc. Joint School RF Engineering for Accelerators,* 1997.
[46] J. Haimson, "Some aspects of electron beam optics and X-ray production with the linear accelerator," *Nuclear Science, IRE Transactions on,* vol. 9, pp. 32-49, 1962.
[47] A. Oppelt, *Imaging systems for medical diagnostics*: Publicis MCD, 2005.
[48] R. Fowler and L. Nordheim, "Field emission from metallic surfaces," in *Proc. R. Soc. London, Ser. A*, 1928, pp. 173-181.
[49] J. Potter, "Conceptual design report - MEBT rebuncher cavity," *SNS technical note FE-EE-019,* 2000.
[50] G. Romanov, S. Barbanotti, E. Borissov, J. Coghill, I. Gonin, S. Kazakov*, et al.*, "CW Room-Temperature bunching cavity for the project X MEBT," in *Proceedings PAC*, 2011.
[51] K. R. Shin, Y. W. Kang, and A. E. Fathy, "Double-gap rebuncher cavity design of SNS MEBT," in *Proceedings of International Particle Accelerator Conference and Exhibition.-New Orleans, USA–2012.–P*, 2012, pp. 3898-3900.
[52] K. R. Shin, Y. W. Kang, and A. E. Fathy, "Feasibility of Folded and Double Dipole Radio Frequency Quadrupole (RFQ) Cavities for Particle Accelerators," 2014.
[53] K. R. Shin, Y. W. Kang, and A. E. Fathy, "Design Guidelines of a Double-Gap Microwave Rebuncher Cavity for a 400 MHz, 2.5 MeV Energy Light Ion Accelerator with Lower Gap Voltage and Field," *Nuclear Science, IEEE Transactions on,* vol. 61, pp. 817-823, 2014.

APPENDIX

A1. Measurements of R/Q using perturbation Theory

Typically, R/Q is used as the cavity figure of merit that has no dependence on the power or the material but only on the geometry. Since both R_s and Q are material related, direct measurement of the two is not very precise in general. However, R/Q is a function of the cavity geometry only. R/Q can be measured from the frequency or phase variation while the cavity is under controlled perturbation. Thus, based on perturbation theory [22], a change in the stored energy is comparable to the associated frequency shift if the energy variation is small. Typically, in this perturbation method, we use a bead movement through the cavity on-axis and, the resonance frequency is measured as a function of the bead position [23].

Equation (1) represents an analytic expression of both frequency and phase when a perturbing object with a spherical geometry is used [23]. The magnetic fields at the bead location, H_b, can be approximated as zero for the TM_{010} mode if the bead radius r is very small. From the measured phase ϕ, the frequency difference Δf with respect to the frequency f_0 can be calculated using

$$\frac{\Delta f}{f_0} \cong \frac{\tan\phi}{2Q_L} = -\frac{\pi \cdot r^3}{U}\left[\varepsilon_0 E_b^2 - \frac{\mu_0}{2} H_b^2\right] \qquad (1)$$

where U is the stored energy in cavity, Q_L is the loaded Q , ε_0 and μ_0 are the permittivity and permeability in the air respectively, and E_b is the electric field at the bead location.

The frequency shift $\Delta f = f_0 - f(z)$ is measured where f_0 is a resonance frequency of unperturbed cavity and $f(z)$ is the resonance frequency of the cavity when a bead is inside the cavity at position z. Researchers usually prefer to measure a phase shift instead of the frequency difference [24].

R/Q result can then be obtained from the integration of this $\Delta f / f_o$ along the cavity axis using the well-known relation (2) [24].

$$\frac{R}{Q} = \frac{2}{3\pi \cdot f_0 \cdot \Delta V \cdot \varepsilon_0} \left[\left(\int \sqrt{\frac{\Delta f(z)}{f_0}} \cos kz \cdot dz \right)^2 + \left(\int \sqrt{\frac{\Delta f(z)}{f_0}} \sin kz \cdot dz \right)^2 \right] \qquad (2)$$

where k is the wavenumber, and z is the longitudinal coordinate. The ΔV in the denominator term stands for the volume of the perturbing object.

VITA

Ki R. Shin earned his Bachelor of Science degree from Handong Global University, Pohang, South Korea, in 2004. From 2005 to 2008, he worked as a RF Engineer at the LG Electronics, Seoul, South Korea. In August 2008, he joined the University of Tennessee at Knoxville where he started his Ph. D. program in Electrical Engineering. From 2008 to 2014, he worked as part of the Spallation Neutron Source (SNS) project team at Oak Ridge National Laboratory (ORNL), Oak Ridge, TN. In 2014, he also worked with the Computational Science & Engineering Division (CSE) at ORNL. His research interests include passive RF devices, printed RF circuit, metamaterial-inspired antennas, high power RF, and accelerator technology.